Detection of
exclusive reactions
in the
Hermes Recoil Fiber Tracker

vorgelegt von

Tibor Keri

aus Subotica, Jugoslawien

Dekan: Prof. Dr. Bernd Baumann

1. Berichterstatter: Prof. Dr. M. Düren
2. Berichterstatter: Prof. Dr. C.-D. Kohl

Zusammenfassung

Das Standardmodell der Teilchenphysik beschreibt die grundlegenden Bestandteile und Kräfte in unserer Welt. Allerdings gehen viele Aspekte der subatomaren Welt noch über dem Bereich der theoretischen Vorhersagen hinaus. Dazu gehört, daß die Zusammensetzung des Nukleonspins, welches Drehimpuls- und Bahndrehimpulsbeiträge von Quarks und Gluonen enthält, noch nicht vollständig verstanden wird. Der tatsächliche Quarkdrehimpulsbeitrag zum vollständigen Nukleonspins beträgt nur etwa 30%. Ein neuentwickelter Formalismus ermöglicht die interne Struktur des Nukleons durch so genannte GPDs (Generalized Parton Distributions) auf eine umfangreichere Art als die vorher verwendeten PDFs (Parton Density Functions) zu beschreiben. Diese GPDs werden durch die Summenregel von Ji mit den Beiträgen des Gesamtdrehimpulses von Quarks und Gluonen verknüpft und können durch die Untersuchung von harten exklusiven Reaktionen bestimmt werden. DVCS (deeply virtual Compton scattering) ist die einfachste exklusive Reaktion, um unter Verwendung von Leptonenstrahlen mit verschiedenen Helizitäten und Ladungen einige dieser Verteilungen zu messen.

HERMES (HERA measurements of spin) ist eines der Experimente zur Untersuchung des Nukleonenspins. Es befindet sich innerhalb HERA (Hadronen-Elektronen Ring Anlage), welches ein $e^{\pm}$-p-Beschleuniger am DESY (Deutsches Elektronen-Synchrotron) ist. Bei dem HERMES Experiment wird nur der polarisierte Elektron-/Positron-Strahl verwendet, welcher an wahlweise polarisierten oder unpolarisierten Gasen gestreut wird. Das Vorwärtsspektrometer vom HERMES Experiment besteht aus Spurdetektoren sowie Detektoren zur Teilchenidentifikation. In der ersten Phase der Datennahme wurden nur die Teilchen in Vorwärtsrichtung detektiert. Die Kinematik von exklusiven Reaktionen wurden unter der Verwendung fehlender invarianter Restmasse vervollständigt.

Um die Exklusivität zu verbessern und um die Auflösung kinematischer Variablen zu erhöhen, wurde das HERMES Vorwärtsspektrometer um den RD (Recoil Detector) erweitert, wobei danach die Messungen mit unpolarisierten Gasen erfolgten. Dieser Detektor besteht aus dem Silicon Strip Detector, dem SFT (Scintillating Fiber Tracker), dem Photon Detector und wird von einem supraleitenden Magneten mit einer Feldstärke von 1T umgeben. Er stellt mehrere Raumpunkte für Spurrekonstruktion und damit für die Impulsrekonstruktion zur Verfügung. Die Energieverluste der Teilchen beim Passieren der verschiedenen Detektoren werden verwendet, um die Teilchen identifizieren zu können. Der Hauptteil dieser Arbeit war die Implementierung des SFT- und des RD-Auslesesystems.

Vor der Installation des RD wurde eine Reihe von Messungen mit verschiedenen Versuchsaufbauten durchgeführt, um das Konzept des Detektors zu prüfen, die interne Ausrichtung zu messen und die Installation vorzubereiten. Diese Messungen für den SFT werden beschrieben und die wesentlich-

en Resultate werden gezeigt. Ausserdem wurde eine erste Analyse der aktuellsten Datenproduktion 06d/06d0 durchgeführt, um die Leistung des installierten RD in Verbindung mit dem HERMES Vorwärtsspektrometer zu zeigen.

Abstract

The standard model of particle physics describes successfully the fundamental constituents and forces in our world; nevertheless, many details of the subatomic world are still beyond the scope of theoretical predictions. The internal structure of the nucleon has been investigated in detail and it was found that the nucleon spin budget, i.e. the composition of the nucleon spin by the spin and orbital angular momentum of quarks and gluons is not yet understood. It has been measured that the intrinsic quark spin contribution is only about 30% of the total spin of the nucleon. A recently developed formalism allows to describe the internal structure of the nucleon by so-called GPDs (Generalized Parton Distributions) in a more complete way than the previously used PDFs (Parton Density Functions). The GPDs are linked by the Ji sum rule to the angular momentum contributions of quarks and gluons. These GPDs can be accessed by the investigation of hard exclusive reactions. DVCS (deeply virtual Compton scattering) is the cleanest exclusive reaction to determine some of these distributions, using lepton beams with different helicity states and charges.

HERMES (HERA measurements of spin) is one of the experiments which were carried out to complete the information about the nucleon spin budget. It is located at HERA which is an $e^{\pm}$-p-collider at DESY but uses only the polarized electron- and positron-beam, which is scattered off a gaseous internal target. The HERMES forward spectrometer consists of a set of detectors that are used for tracking, while another set of detectors provides information on particle identification and triggering. In the first phase of HERMES, only forward going particles were detected. Exclusive reactions have been measured using a missing invariant mass technique.

In order to improve exclusivity and to enhance the resolution of kinematic variables the HERMES collaboration decided to remove the equipment for the polarized target and to install the RD (Recoil Detector) with an unpolarized target at this position. This detector consists of the Silicon Strip Detector, the SFT (Scintillating Fiber Tracker), the Photon Detector and is surrounded by a 1T superconducting magnet. It provides several space points for tracking and thus momentum reconstruction. The energy deposition in the various detectors is used to achieve particle identification. The main part of the thesis work was the implementation of the SFT and the RD readout system.

Before the installation of the RD a series of test runs were carried out to proof the concept of the detector, to measure the internal alignment and to prepare the installation. These test runs for the SFT are described and major results are shown. Furthermore a preliminary analysis of the latest data 06d/06d0 was carried out to show the performance of the installed Recoil Detector in combination with the HERMES forward spectrometer.

Contents

Chapter 1

Introduction

The microscopic world can be very successfully described by the atomic model developed by Bohr [Boh13] and confined by Sommerfeld [Som15]. In this model atoms are constituted by protons, neutrons and electrons. The subatomic world described by the standard model of particle physics is not yet completely clarified. The common agreement until now is the point like property of the electrons while the protons and neutrons seems to be compound objects. These components are quarks with gluons as carrier of the strong forces. Further investigations condensate into the well known standard model [Gri87] containing QCD (Quantum Chromo Dynamics) where quarks and leptons are the constituents of matter while the electromagnetic, strong and weak forces are interacting by the carrier photons, gluons and bosons. Even the description of matter and the predictions are very well tested this model is not though yet complete. The aspect of gravity is still remaining to be taken into account and calculations on long distance scale are challenging and not done yet analytically. Mainly the complete nucleon spin budget is still unclear until now as well.

Starting with elastic scattering the transverse spatial distribution of the partons can be described in the frame of quantum electro dynamics by FFs (Form Factors) very precisely. By investigations of deep inelastic scattering in the frame of quantum chromo dynamics the longitudinal momentum distributions are accessible and can be described by PDFs (Parton Distribution Functions). The uncertainty relation limits the simultaneously measurable resolutions of corresponding properties like location and momentum. As FF describing transverse spatial distributions and PDF describing longitudinal momentum distributions both properties are disentangled. They can be combined simultaneously to distributions named GPDs (Generalized Parton Distributions) [Mue+94, Ji97a] which was developed in the recent years. Beside combining the both models together the Ji [Ji97b] sum rule opens with GPDs several new paths to access further informations about the nature of the nucleon. Several GPDs can be accessed by investigations of hard

exclusive reactions. Therefore GPDs are more and more used for studies.

Many experiments have been carried out to identify the contributors to the nucleon spin and to investigate their constraints. A naive quark model where three quarks as partons of the nucleon carry the whole spin of the nucleon was a first try to explain the nucleon spin budget. This simple model has to be refined as measurements by the EMC (European Muon Collaboration) [Ash+88, Ash+89] show that the intrinsic contribution by quarks are much lower than expected. In order to solve this so called spin crisis several high energy experiments were started to search answers to these contributions. One of these experiments is the HERMES (HERA measurements of spin) experiment [Her+93, Due95] which was running inside HERA (Hadron Elektron Ring Anlage) at DESY (Deutsche Elektronen Synchrotron). The HERMES experiment was designed to contribute information about the nucleon spin budget. Due to improvements in understanding of deep inelastic scattering and new models like GPDs the physics program has been widely extended.

The HERMES experiment was running with electron or positron beam. The target was either polarized gas of ^1H, ^2H, ^3He or unpolarized gas of ^4He, N, Ne, Kr, Xe. The HERMES detector was built as a forward spectrometer for quasi fixed target which consists of identical upper and lower half. A set of detectors is used to reconstruct the particle track and to determine the particle momentum. Another set of detectors is used for particle identification. As the space in front of the HERMES detector was occupied by the equipment of the polarized gas target the recoiling particles were not detectable. The complete kinematics of the exclusive reactions was computed with the missing invariant mass technique.

To improve exclusivity and the resolution of kinematic variables the HERMES collaboration decided to upgrade the HERMES detector with the Recoil Detector. The aim of this new Recoil Detector is directly detect recoiling particles and measure their properties. The Recoil Detector consists of a Silicon Strip Detector, a Scintillating Fiber Tracker and a Photon Detector. It is surrounded by a superconducting magnet with a 1T center field strength. The core of the this work was the implementation of the readout for the Scintillating Fiber Tracker and to bind the readout for the Recoil Detector to the HERMES data acquisition.

The outline of this work starting with the motivation why measurements of hard exclusive reactions are attractive. Afterwards the HERMES forward spectrometer with the used facilities is described. Hereafter the Recoil Detector with the major components is recorded as well. Rearwards the results of several test runs for the preparation of the Recoil Detector and some preliminary results of the experiment are presented. The results of the 06d/06d0 production are compared to previous results.

Chapter 2

Nucleon spin budget

The standard model of particle physics is perhaps the best proven model. Nevertheless the nucleon spin budget is not yet completely clarified. A possible path to access informations about the constituents and their contributions is the recently developed GPDs (Generalized Parton Distributions) which can be ascertained by investigations of exclusive reactions. In front of the description a short introduction of the nomenclature to describe properties of scattering reactions and at the end recent results at HERMES are shown. The particles of the electron-/positron-beam are named lepton in this work.

2.1 Deep Inelastic Scattering

The general process visualized in figure 2.1 for a lepton scattering reaction can be expressed by

$$(2.1) \qquad\qquad k + N \rightarrow k' + \sum_{j=1}^{n} X_j.$$

with N as the nucleon in the initial state, k (k') as the lepton in the inital (final) state and where n denotes the number of the scattered and produced particles. In the limit of inelastic scattering, for an elastic scattering process the nukleon N remains intact, thus follows $n = 1$ and $X_1 = N$.

Further categorizations are inclusive, semi-inclusive and exclusive measurements. In case of an inclusive measurement only the scattered lepton is detected, while in semi-inclusive measurements some but not all other particles are detected. If all particles in the final state are detected the measurement is called exclusive.

The HERMES experiment [Her+93, Due95] uses as will be shown later a $27.6 GeV$ polarized lepton beam. In this case other interactions like weak forces at higher energies can be neglected.
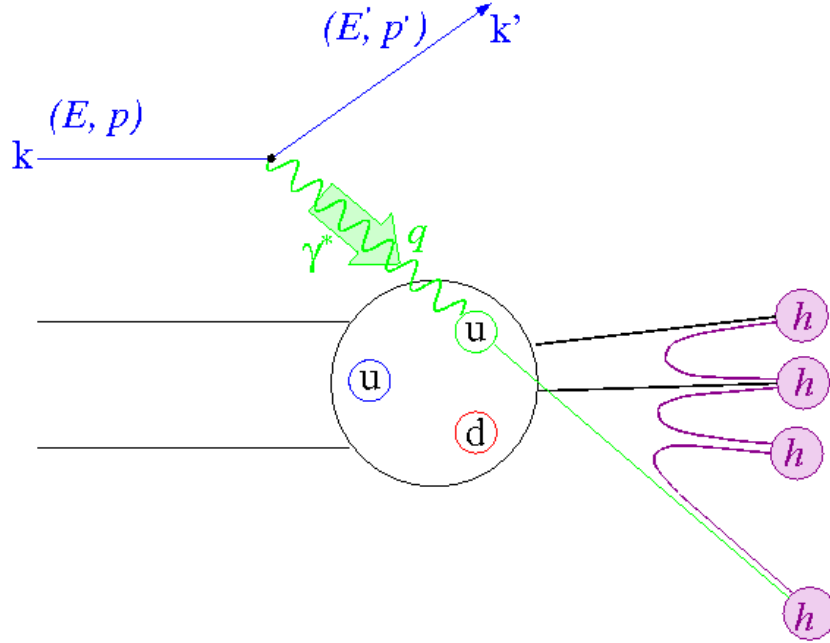
Figure 2.1:   *Illustration of a deep inelastic scattering reaction where the incoming lepton (k) scatters off and interacts with the nucleon by a virtual photon.*

The four momentum transfered by the virtual photon is the difference

$$(2.2) \qquad\qquad\qquad q = k - k'$$

of the four momentum of the incoming k and scattered k' lepton. The square of the four momentum transfer q due to the uncertainty relation can be interpreted as a spatial resolution $Q^2 \sim \lambda^{-2}$ of the probing and can be expressed as

$$(2.3) \qquad\qquad\qquad Q^2 = -q^2.$$

The value q is a space like property and therefore q^2 is negative. In order to have a positive resolution the negative square of q is used as the spatial resolution Q^2.

The energy ν transfered by the virtual photon can be expressed as

$$(2.4) \qquad\qquad\qquad \nu = \frac{p \cdot q}{M}$$

where M denotes the nucleon mass and where p is the four momentum of the nucleon before the interaction.

The squared sum of the four momentums of the initial nucleon and the incoming lepton holds the inital state invariant mass

$$(2.5) \qquad\qquad\qquad s = (p + k)^2$$

of the reaction.

The squared sum of the four momentum of the nucleon and the interacting virtual photon results to the invariant mass

$$(2.6) \qquad\qquad\qquad W^2 = (p + q)^2$$

of the nucleon-photon-system.

The Bjoerken work [Bjo69] shows that the description of interactions can be made without properties with physical dimensions. Therefore the following properties are dimensionless and are interpreted accordingly.

The fractional energy y of the virtual photon can be defined as

$$(2.7) \qquad\qquad\qquad y = \frac{p \cdot q}{p \cdot k}.$$

The four momentum fraction x of the nucleon-photon-system to the center-of-mass system can be written as

$$(2.8) \qquad\qquad\qquad x = \frac{-q^2}{2p \cdot q} = \frac{Q^2}{2p \cdot q}.$$

As W^2 can be expressed as

$$(2.9) \qquad W^2 = (p + q)^2 = p^2 + 2p \cdot q + p^2 = p^2 + 2p \cdot q \, (1 - x)$$

x can be interpreted as a measure of the inelasticity of the process as in an elastic process the equation $x = 1$ holds. Due to the kinematics in inelastic processes the ranges are limited to $0 < x < 1$ and to $0 < y < 1$.

The properties Q^2, s, W^2, y, x are invariant against Lorentz transformations.

In the kinematic range of the HERMES experiment running with $27.6 GeV$ lepton beam the rest mass of the imprinted lepton with $\sim 0.5 MeV$ on the first order can be neglected. Under this assumption these properties can be expressed in the laboratory frame as:

$$(2.10) \qquad\qquad Q^2 = -q^2 \approx 4EE' \sin^2 \left(\frac{\theta}{2} \right)$$

$$(2.11) \qquad \nu = \frac{p \cdot q}{M} \approx E - E'$$

$$(2.12) \qquad s = (p + k)^2 \approx 2ME + M^2$$

$$(2.13) \qquad W^2 = (p + q)^2 \approx M^2 + 2M\nu - Q^2$$

$$(2.14) \qquad y = \frac{p \cdot q}{p \cdot k} \approx \frac{\nu}{E}$$

$$(2.15) \qquad x = \frac{Q^2}{2p \cdot q} = \frac{Q^2}{2M\nu} \approx \frac{Q^2}{2M(E - E')}$$

In these equations E and E' denotes the energy of the incoming and scattered lepton, θ is the polar angle between the vectors of the unscattered and the scattered lepton. All these properties can be determined by the knowledge of the initial state and by detecting only the scattered lepton.

2.2 Generalized Parton Distributions

GPDs (Generalized Parton Distributions) [Mue+94, Ji97a] have been developed few years ago to combine transverse charge distribution information named FFs (Form factors) with longitudinal momentum distribution information named PDFs (Parton Density Functions) for description of exclusive processes. After the correlation between these GPDs and the total angular momentum was investigated by Ji [Ji97b] this description got more and more used. A very detailed description of GPDs and the current development can be found in [Die03].

GPDs consist of a set of distributions for quarks and gluons for each flavor and helicity state. Most often discussed are the four twist-2 quark-chirality conserving distributions: the polarization-independent distributions are denoted by $H(\bar{x}, \xi, t)$ and $E(\bar{x}, \xi, t)$, while the polarization-dependent distributions are named $\tilde{H}(\bar{x}, \xi, t)$ and $\tilde{E}(\bar{x}, \xi, t)$. The distributions E and $\tilde{E}$ do not conserve the nucleon helicity but the distributions H and $\tilde{H}$ do. The distributions of all flavors for each quark and gluon are superposed to describe the total response. The used parameters $\bar{x}$, ξ and t are shown in figure 2.2.
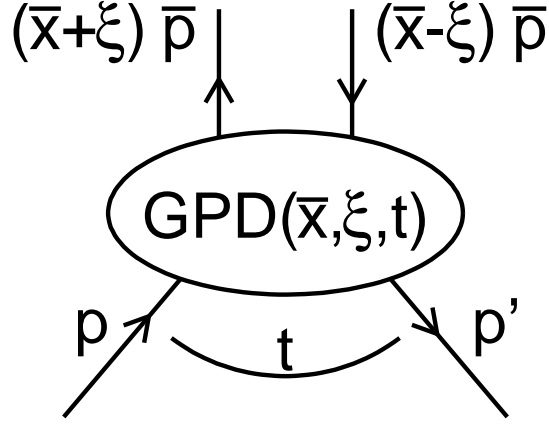
The four momentum $\bar{p}$

Figure 2.2: *Description of GPDs by momentum fraction $\bar{x}$, skewness ξ and momentum transfer t as described in the text. p, p' and $\bar{p}$ are the four momentum of the target for the initial state, finial state and the averaged case.*

$$(2.16) \qquad \bar{p} = \frac{1}{2}\left(p + p'\right)$$

is the average of the four momentum p of the nucleon in the initial state and the four momentum p' of the nucleon in the final state. The parameter $\bar{x}$ is the average longitudinal momentum fraction of the quark, while the skewness parameter ξ represents the fractional longitudinal-momentum transfer to that quark. Positive values of $\bar{x} + \xi$ and $\bar{x} - \xi$ are interpreted as quarks, while negative values are treat as anti-quarks.

The Mandelstam variable t

$$(2.17) \qquad t = \left(p - p'\right)^2$$

is the squared momentum transfer to the nucleon and is therefore invariant against Lorentz transformations.

Knowing unpolarized GPDs $H\left(\bar{x}, \xi, t\right)$ and $E\left(\bar{x}, \xi, t\right)$ the Ji sum rule [Ji97b]

$$(2.18) \qquad J_{q,g} = \lim_{t \to 0} \frac{1}{2} \int_{-1}^{+1} d\bar{x}\ \bar{x}\left(H_{q,g}\left(\bar{x}, \xi, t\right) + E_{q,g}\left(\bar{x}, \xi, t\right)\right)$$

can be used to determine the total angular momentum contribution by quarks and gluons which is one of the key feature of this model. By knowing the intrinsic spin contributions of quarks and gluons the contribution of the orbital angular momentum can be accessed as well.

As further advantage the GPDs formalism still provides access to FF and PDF. The FF are accessible by the first momentum of $\bar{x}$ while the PDF are the limit for vanished momentum transfer $t \to 0$ to the nucleon.

Exclusive reactions originated by a virtual photon γ^* to a nucleon p visualized in figure 2.3 can be formulated by
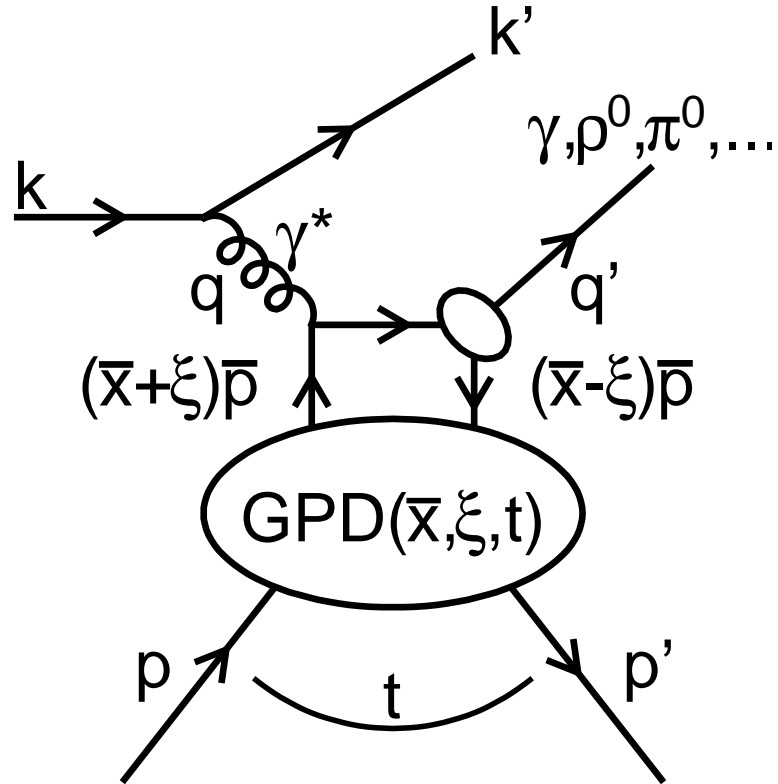

Figure 2.3: *Illustration of exclusive reactions by scattering of lepton (k) on a nucleon (p).*

$$(2.19) \qquad\qquad\qquad \gamma^* + p \to X + p'$$

where the nucleon p, p' is still intact but a different particle X is generated. These exclusive reactions are an important tool to access the properties of GPDs and therefore to the nucleon constituents.

Another feature of exclusive reactions is the possibility to probe certain reactions by final state selection. Final states with a ρ^0, the scattered projectile and the intact nucleon allow studies of quarks and gluons on the same order and on linear order as described in [Goe+01, Die+04b], with recent results in [Ros+07] and in HERMES paper which is in preparation.

But the cleanest way to access GPDs is deeply virtual Compton scattering which will be introduced in the following section.

2.3   Deeply Virtual Compton Scattering

Theoretically simplest process to access GPDs is DVCS (deeply virtual Compton scattering). The DVCS process visualized in figure 2.4 can be expressed by the reaction

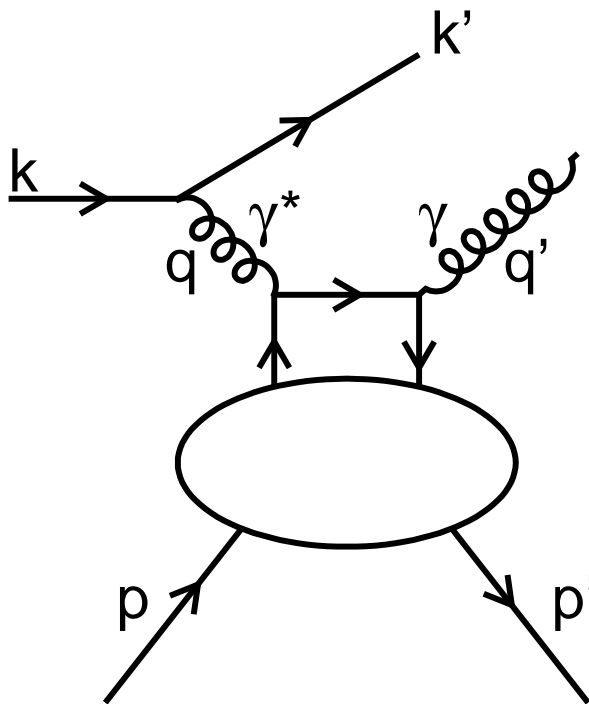Figure 2.4: *DVCS (deeply virtual Compton scattering. The virtual photon originated from the scattered projectile probes the nucleon which stays intact in the final state and produces a real photon.*

(2.20) $k + p \rightarrow k' + \gamma^* + p \rightarrow k' + \gamma + p'$

with k (k'), p (p'), γ^*, γ which are the initial (final) lepton, the inital (final)

nucleon, the originating virtual photon and the produced real photon. The generated real photon carry information about the involved quark as it is not generated by Bremsstrahlung. The Mandelstam variable t

$$(2.21) \qquad t = \left(p - p'\right)^2 = (q - q')^2$$

of the squared momentum transfer to the nucleon can be calculated alternatively by the momentum of the two incident photons. In this case the momentum transfer can be determined without the detection of the recoiled nucleon.

The final state of the DVCS process can not be distinguished from the BH (Bethe-Heitler) process as it has the same initial and final state as shown in figure 2.5. The BH process is an elastic scattering process and can be precisely calculated in the frame of QED (Quantum Electro Dynamics).
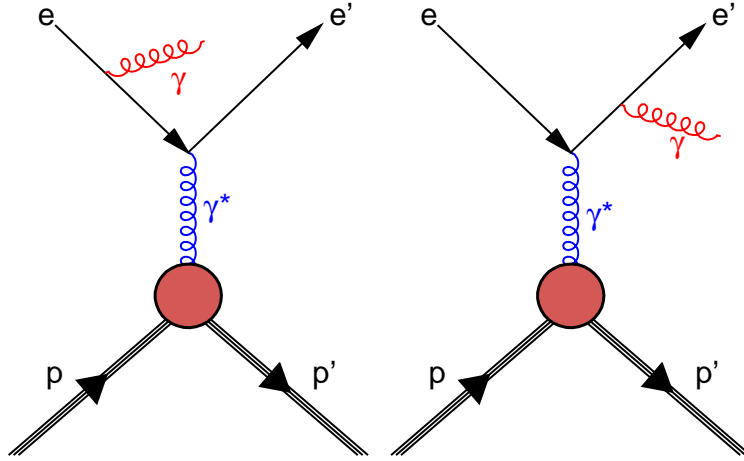

Figure 2.5: *The Bethe-Heitler process can not be distinguished in the initial and final states from the deeply virtual Compton scattering.*

The combined cross section [Bel+02]

$$(2.22) \qquad \frac{d\sigma}{dxdyd|t|d\phi} = \frac{\alpha_{em}^3 xy}{8\pi Q^2 \sqrt{1 + 4x^2 M^2/Q^2}} \left| \frac{\tau}{e^3} \right|^2$$

results to an interference of the amplitudes by

$$(2.23) \qquad |\tau|^2 = |\tau_{BH} + \tau_{DVCS}|^2 = |\tau_{BH}|^2 + |\tau_{DVCS}|^2 + \Im$$

with the interference term

(2.24)
$$\Im = \tau_{BH}^{*}\tau_{DVCS} + \tau_{DVCS}^{*}\tau_{BH}.$$

The electromagnetic fine structure constant α_{em} and the elementary charge e is used here.

An additional parameter for separation between DVCS and BH is the angle $\theta_{\gamma^{*}\gamma}$ between the trajectories of the virtual photon and the produced real photon. A further parameter for describing azimuthal asymmetries is the azimuthal angle ϕ between the scattering plane defined by the incident and scattered lepton and the production plane defined by the momentum of the virtual and real photon shown in figure 2.6.
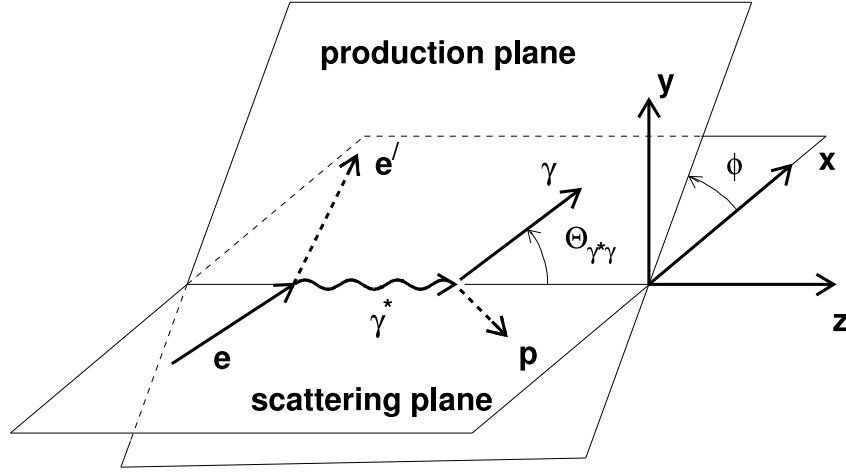

Figure 2.6: *Diagram of the kinematics for DVCS reactions. The scattering plane is defined by the trajectories of the projectile while the production plane is defined by the virtual and real photons. The angle ϕ is formed by these two planes. The angle $\theta_{\gamma^{*}\gamma}$ are formed by trajectories of the virtual and real photon.*

2.3.1 Azimuthal asymmetry

The two pure terms and the one interference term of the combined amplitude of BH-process and DVCS-process can be evolved in leading order to a Fourier sum [Bel+02] in which ϕ denotes the angle between the scattering plane and the production plane as shown in figure 2.6:

(2.25)
$$|\tau_{BH}|^{2} = \frac{e^{6}}{xy^{2}\left(1 + 4x^{2}M^{2}/Q^{2}\right)P_{1}\left(\phi\right)P_{2}\left(\phi\right)}\left(c_{0}^{BH} + \sum_{n=1}^{2}\left(c_{n}^{BH}\cos\left(n\phi\right)\right)\right)$$

(2.26)

$$|\tau_{DVCS}|^2 = \frac{e^6}{y^2 Q^2} \left(c_0^{DVCS} + \sum_{n=1}^{2} \left(c_n^{DVCS} \cos\left(n\phi\right)\right) + \lambda s_1^{DVCS} \sin\left(n\phi\right) \right)$$

(2.27)

$$\Im = \frac{-C\ e^6}{xy^3 t P_1\left(\phi\right) P_2\left(\phi\right)} \left(c_0^I + \sum_{n=1}^{2} \left(c_n^I \cos\left(n\phi\right)\right) + \lambda \sum_{n=1}^{2} \left(s_n^I \sin\left(n\phi\right)\right) \right)$$

with C as the charge and λ as the helicity of the beam lepton, $P_1\left(\phi\right)$ and $P_2\left(\phi\right)$ as the BH propagators [Bel+02, Jaf96].

By combining measurements with different states like charge and polarization of the striking beam lepton certain coefficients can be determined by azimuthal asymmetries.

As shown in figure 2.7 in the HERMES kinematics the amplitude of the BH process is almost over the whole $\theta_{\gamma^*\gamma}$ range much larger than the amplitude of the DVCS process [Kor+02]. As the contribution by the pure BH term can be precisely calculated in QED and the contribution by the pure DVCS term is of sub leading order the interference term provides an unique access to the DVCS amplitude in linear order which is significantly increased by the larger BH amplitudes compared to the pure DVCS term.

The nomenclature for the coefficients of azimuthal asymmetries are A_{BT} where B and T are the polarization of the beam and the target. These states can be L, T, U which are the cases for longitudinal, transversal or unpolarized polarization. Despite of this notation the coefficient for the beam charge asymmetry is denoted as A_C.

As the DVCS process provides access to all GPDs of quarks the total angular momentum contribution of the quarks to the nucleon spin budget can be determined with the Ji sum rule [Ji97b]. However the measurements for all the manifold states and parameters are still challenging.

2.4 Results at HERMES

At the HERMES experiment in first years of running the recoiling particle was not detectable. The complete kinematics of the exclusive reactions are computed by the missing invariant mass technique. The newly installed Recoil Detector into the HERMES experiment detects the recoiling particles directly. This enhances exclusivity and the resolution of kinematic variables.

All measured results until now are using data samples before the installation of the Recoil Detector. An extended introduction and presentation of the recent results can be found in [Air+01, Ell03, Ell07, Kra05, Ye07, Air+06, Air+08]. An simple overview about results at HERMES will be
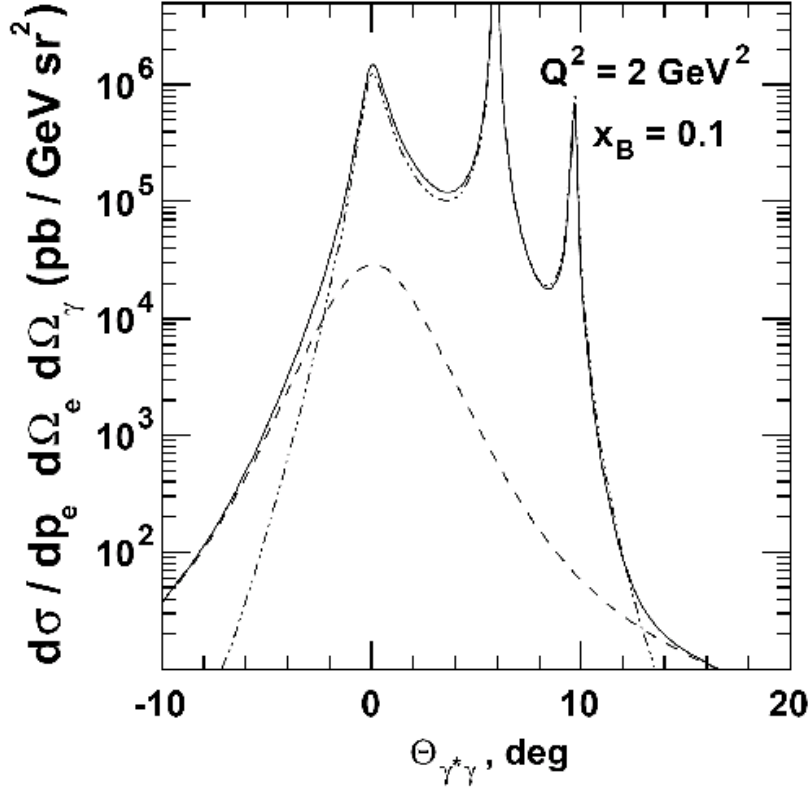
Figure 2.7:   *The solid line is the sum of the cross section sum of BH-process (dashed-dotted line) and DVCS (dashed line) versus the angle $\theta_{\gamma^*\gamma}$ each in the kinematic region of HERMES. $\theta_{\gamma^*\gamma}$ is the angle between virtual and real photon [Kor+02]. Positive values of $\theta_{\gamma^*\gamma}$ correspond to $\phi = 0$, while negative ones are for $\phi = \pi$. The range used to select exclusive events are $5mrad(\approx 0.28^o) < |\theta_{\gamma^*\gamma}| < 45mrad(\approx 2.6^o)$*

given below. The following measurements are done with unpolarized hydrogen as a target and with an electron and a positron beam.

2.4.1   Beam Spin Asymmetry

In order to determine the coefficient for the BSA (beam spin asymmetry) the measurements of longitudinal polarized lepton beam on unpolarized hydrogen are combined and the asymmetry [Bel+02, Air+01] is given by

$$(2.28) \qquad A_{LU} = \frac{d\sigma^+ - d\sigma^-}{d\sigma^+ + d\sigma^-} = \frac{1}{<|P_B|>} \frac{N^+ - N^-}{N^+ + N^-} \propto C \frac{x}{y} \frac{s_1^{\Im}}{c_0^{BH}} \sin(\phi)$$

where C denotes the charge of the projectile while $d\sigma^+$ and $d\sigma^-$ are the cross sections for the case of parallel and anti-parallel longitudinal beam helicity. The event counts N^+ and N^- for the corresponding states are normalized to the luminosity and the amplitude is adjusted by the mean beam polarization $< |P_B| >$. The result for the BSA amplitude is shown in figure 2.8.
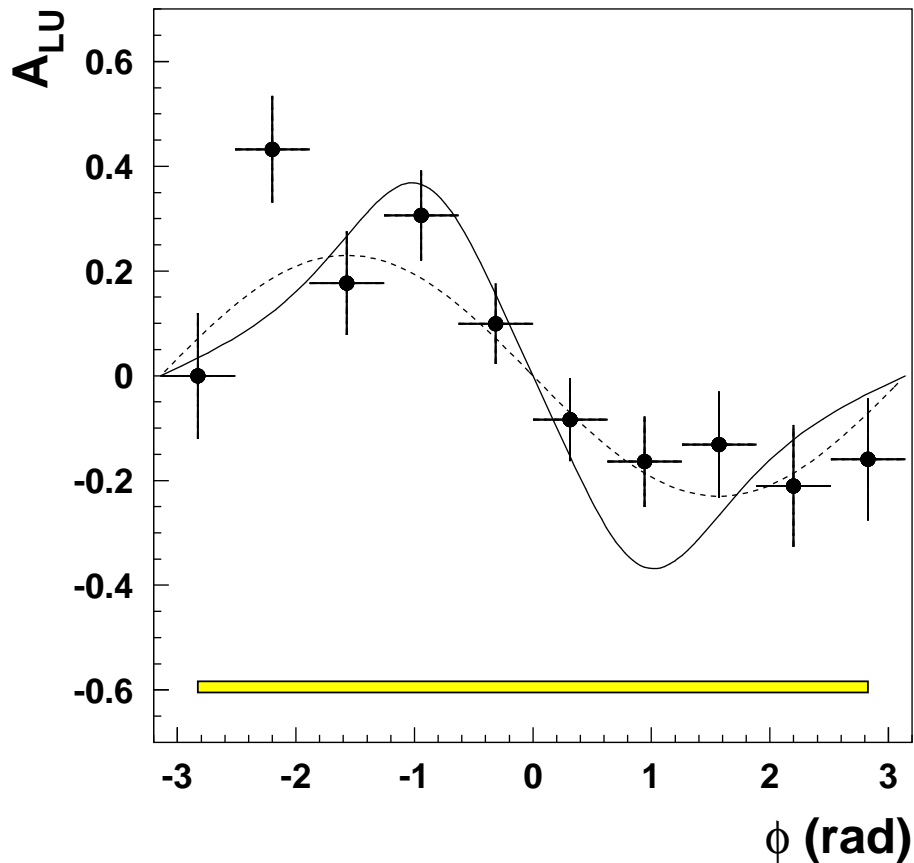

Figure 2.8:   *Beam spin asymmetry for electro-production of photons as function of the azimuthal angle ϕ [Air+01]. The dashed curve represents a $\sin(\phi)$ dependence with an amplitude of 0.23, while the solid curve represents the result of a model calculation taken from [Kiv+01]. The horizontal error bars represent the bin width, and the error band below represents the systematic uncertainty.*

2.4.2 Beam Charge Asymmetry

The BCA (beam charge asymmetry) is only measurable at HERA due to the availability of electron and positron beam. By combining measurements

with positrons and electrons as a projectile the leading coefficient for the beam charge asymmetry [Bel+02], [Air+06] can be expressed by

$$(2.29) \qquad A_C = \frac{d\sigma^+ - d\sigma^-}{d\sigma^+ + d\sigma^-} = \frac{N^+ - N^-}{N^+ + N^-} \propto -\frac{x}{y}\frac{c_1^{\mathfrak{I}}}{c_0^{BH}}\cos(\phi)$$

where the sign denotes the corresponding beam charge, $d\sigma^+$ and $d\sigma^-$ are the cross sections, N^+ and N^- are the normalized to the luminosity event counts. In this case the dominant contribution is the $\cos(\phi)$ part of the BCA amplitude which is shown in figure 2.9.
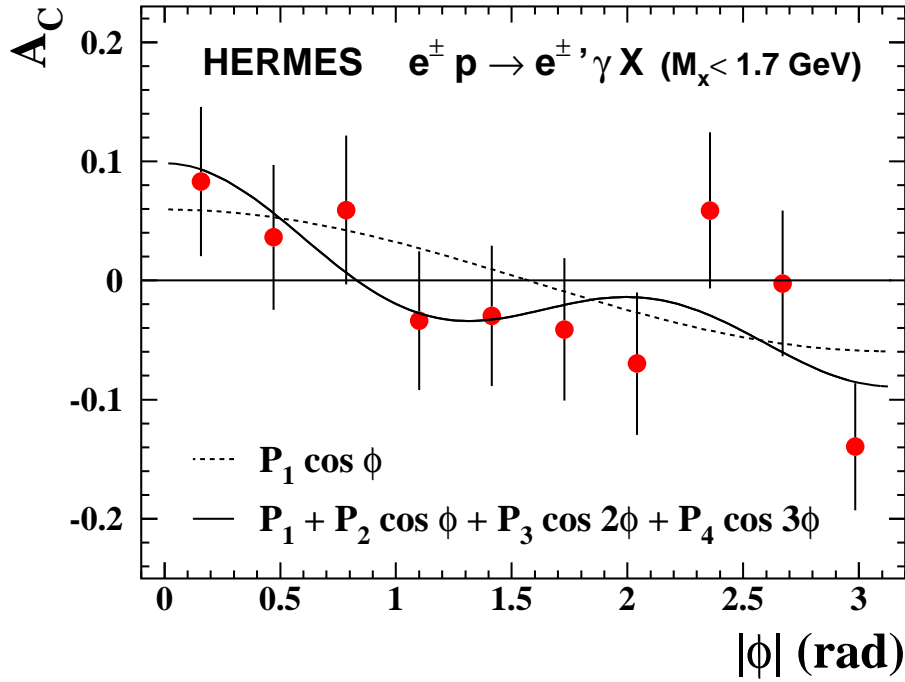

Figure 2.9: *Beam charge asymmetry A_C as function of the azimuthal angle $|\phi|$. The four parameter fit $(-0.011 \pm 0.019) + (0.060 \pm 0.027) * \cos(\phi) + (0.016 \pm 0.026) * \cos(2\phi) + (0.034 \pm 0.027) * \cos(3\phi)$ shown as solid line represents the total contribution of higher harmonics while the dashed line contains only the pure $\cos(\phi)$ amplitude for exclusive sample before background correction. Only statistical uncertainties are shown here[Air+06].*

2.4.3 Transverse Target Spin Asymmetry

Electroproduction of real photons shown in figure 2.10 on transverse polarized hydrogen gas target allow to access total angular momentum of quarks in a model-dependent way [Air+08].
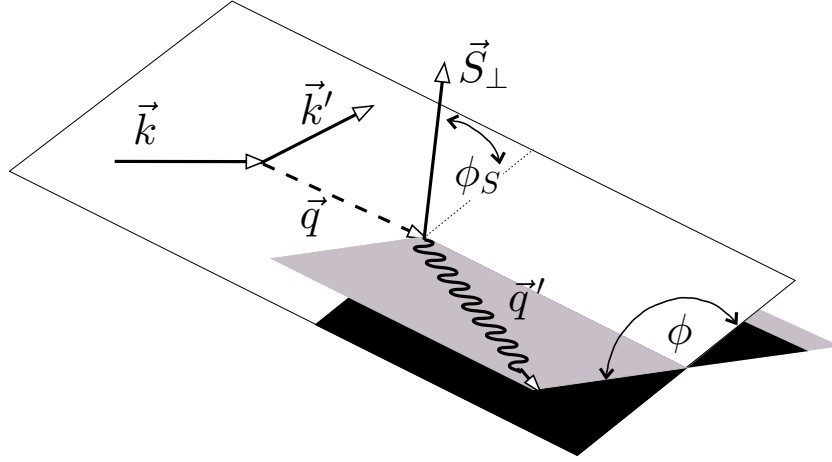
Figure 2.10: *Momenta and azimuthal angles for exclusive electroproduction of photons in the target rest frame following the Trento conventions [Bac+04]. The quantity $\overrightarrow{q} = \overrightarrow{k} - \overrightarrow{k}'$ is the three-momentum of the virtual photon as difference of the initial ($\overrightarrow{k}$) and the final ($\overrightarrow{k}'$) beam lepton three-momenta, while $\overrightarrow{q'} = \overrightarrow{q}'$ denotes the three-momentum of the real photon. The angle between the scattering plane of the lepton to the production plane of the photons is named ϕ, while the angle between the scattering plane of the lepton and the transverse target polarization $\overrightarrow{S}_\perp$ is called ϕ_S.*

Measurements with both target polarities and both beam charges are used to extract azimuthal asymmetries. Beside the BCA amplitude the TTSA (transverse target spin asymmetry) amplitude is needed, which can be expressed in terms of cross sections as

(2.30)
$$A_{UT}(\phi, \phi_S) = \frac{1}{S_\perp} \frac{[d\sigma^+(\phi, \phi_S) - d\sigma^+(\phi, \phi_S + \pi)] - [d\sigma^-(\phi, \phi_S) - d\sigma^-(\phi, \phi_S + \pi)]}{[d\sigma^+(\phi, \phi_S) + d\sigma^+(\phi, \phi_S + \pi)] + [d\sigma^-(\phi, \phi_S) + d\sigma^-(\phi, \phi_S + \pi)]}$$

where the $d\sigma^+$ and $d\sigma^-$ are for the corresponding beam charge and is adjusted by the transverse target polarization $S_\perp$. By comparing calculations of several GPD-models with the experimentally extracted azimuthal asymmetry amplitudes of BCA and TTSA, a model-dependent constraint on the total angular momenta contribution of u- and d-quarks can be accessed [Ell+05]. Model-dependent constraints on the u-quark total angular momentum J_u vs d-quark total angular momentum J_d, obtained by comparing DVCS experimental results and theoretical calculations are shown in figure 2.11.
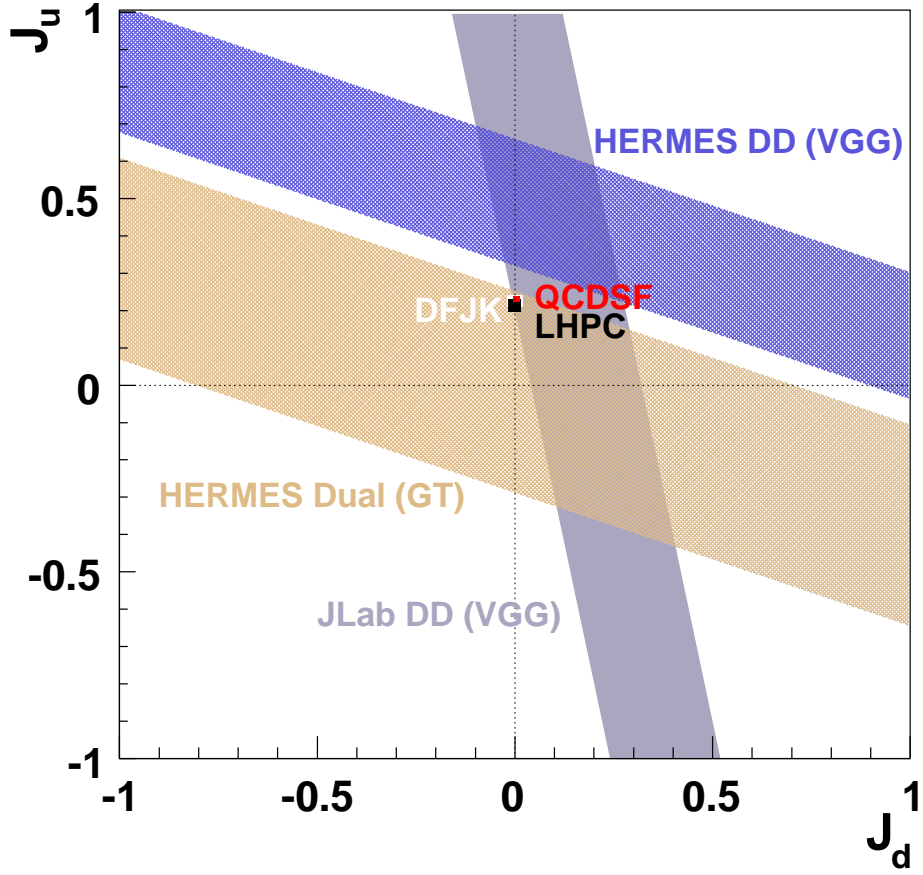
Figure 2.11: *Model-dependent constraints on u-quark total angular momentum J_u vs d-quark total angular momentum J_d, obtained by comparing DVCS experimental results and theoretical calculations. The constraints based on the HERMES data for the TTSA interference amplitudes $A_{UT}^{\sin(\phi-\phi_S)\cos(\phi)}$ and $A_{UT}^{\sin(\phi-\phi_S)}$ use the double-distribution (HERMES DD) [Van+99, Goe+01] or dual-parameterisation (HERMES Dual) [Guz+06] GPD models. The additional band (JLab DD) is derived from the comparison of the double-distribution GPD model with neutron cross section data [Maz+07]. Also shown as small (overlapping) rectangles are results from lattice gauge theory by the QCDSF [Bro+07] and LHPC [Hae+07] collaborations, as well as a result for only the valence quark contribution (DFJK) based on zero-skewness GPDs extracted from nucleon form factor data [Die+04a, Kro07]. The sizes of the small rectangles represent the statistical uncertainties of the lattice gauge results, and the parameter range for which a good DFJK fit to the nucleon form factor data was achieved. Theoretical uncertainties are unavailable. More details can be found in [Air+08].*

Chapter 3

The HERMES Experiment

The HERMES (HERA measurements of spin) experiment [Her+93], [Due95] was started to study the nucleon spin budget with DIS (Deep Inelastic Scattering). An lepton beam with the energy of $27.6 GeV$ was used to scatter off a quasi fixed target provided by polarized gas target. The HERMES experiment was originally designed to measure only the nucleon spin budget but in the meantime the physics program was widely expanded due to improvements in understanding of DIS and to recently developed models. The HERMES forward spectrometer provides detection of products generated by inclusive and semi-inclusive processes directly.

3.1 HERA at DESY

HERA is an e-p-collider and the major facilities used by the HERMES experiment will be presented.

DESY

DESY (Deutsche Elektronen-Synchrotron) of the Helmholtz-Gemeinschaft is a research facility located in Hamburg / Germany. It is shown in figure 3.1. It was founded in 1959 with the main purpose to do scientific fundamental research which covers three major topics:

- development, construction and operation of particle accelerators;

- investigations of matter and force on the scale of particles;

- providing synchrotron radiation for many other disciplines.

Since this time a lot of pioneering experiments and technologies were carried out.

Most of the accelerators are shown in figure 3.2. The first synchrotron ring DESY was built between 1960 and 1964. DORIS (Doppel-Ring-Speicher)

Figure 3.1: *The laboratory at DESY in Hamburg / Germany. The picture shows the location and dimension of HERA and PETRA by the two dashed circles. See also sketch 3.2 for more details.*

is a facility for studies with synchrotron radiation. The PETRA (Positron-Electron Tandem Ring Accelerator) which was built between 1976 and 1978 achieved the pioneering work to discover gluons in 1979 [Wii+79]. Later in 1990 HERA (Hadronen Electronen Ring Anlage) was available to provide two accelerators combined with storage rings with a proton and a lepton beam for unique studies on particle physics. In last years pioneering work was done for TESLA (Tera Scale Accelerator) to proof the concept of next generation of linear lepton colliders as the storage rings for leptons for higher energy getting very challenging and very expensive.

Recently the XFEL (X-ray Free Electron Laser) project was started to provide unique facility to measure in situ chemical reactions, to investigate atomic details of molecules or to make spatial pictures of nano scale physics. After the retirement of HERA in 2007 which will be not used for the next years the upgrade of PETRA was started to improve the properties to be the worldwide most brilliant synchrotron radiation source with additional 14 beam lines with up to 30 experimental stations installed until 2009.
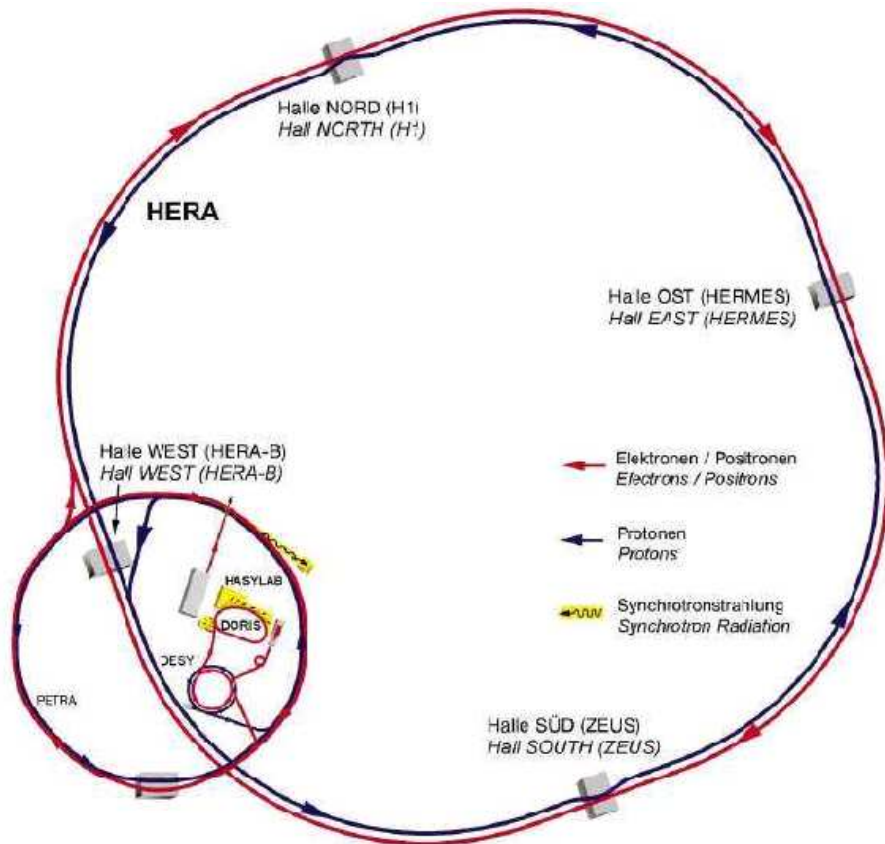
Figure 3.2: *A set of pre accelerators are used to feed HERA with protons and leptons. The arrows indicates the accelerated particles flow which are marked as blue for protons and red for leptons. Four experiments were located at HERA. As indicated H1 in the north and ZEUS in the south were collider's. HERA-B in the west used only the proton beam while HERMES in the east used only the lepton beam.*

HERA

Hera consists of two concentric rings with a circumference of around $6300m$. Each ring had the facility to accelerate particles and store them for several hours.

The one ring provided in the early years an unpolarized proton beam with an energy of $880GeV$. After an upgrade in 1998 the energy was increased to $920GeV$. In the last few months of HERA run time the energy of the proton beam was changed to $460GeV$ and $575GeV$ for additional studies with these lower energies. A typical value for the beam current is around $110mA$ at the beginning of the a fill with a life time of several hundred

hours.

The other ring delivers polarized electron or positron beam with an energy of $27.6 GeV$ starting with up to $50mA$ beam current which drops exponentially with a life time around 13 hours.

These unique features of HERA enables colliding and fixed target experiments. Four detectors were installed in HERA. In the north and south the colliding beam experiments H1 (north) and Zeus (south) are installed. These experiments running from 1992 until the end of HERA in 2007 investigated unpolarized nucleon structure functions with collisions of protons and electrons or positrons aiming discovery of lepto-quarks. The experiment HERA-B located in the west used from 2000 to 2003 only the accelerated protons on a fixed target to examine charm and bottom meson production. The HERMES experiment in the east was running only with accelerated electrons or positrons on polarized or unpolarized gaseous target, designed to contribute in solving the nucleon spin puzzle initiated by EMC experiment [Ash+88], [Ash+89].
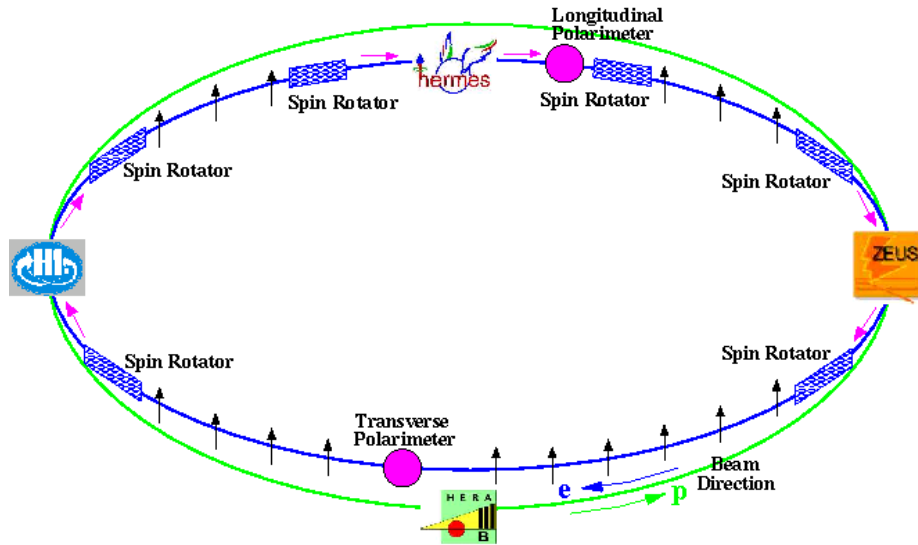

Figure 3.3:   *HERA consist on two concentric storage rings. The green circle shows the proton ring while the blue circle show the lepton beam which is self polarized due to the Sokolov-Ternov effect [Ter+61], [Sok+63], [Sok+64].*

Electron/Positron-Beam

HERA consists of two beams as shown in figure 3.3. The one beam of protons rotates counter clockwise while the other beam of leptons rotates clockwise.

The proton beam as well as the $e^{\pm}$ beam are not continuously filled beams. The whole HERA is segmented into 220 numbered buckets to hold the particles if desired. As the time slice for each bucket is $96ns$ the rotation frequency of a particle is around $(220 * 96ns)^{-1} \approx 47kHz$. Each bucket which is filled with accelerated particles is called bunch. The setup of buckets and bunches has a characteristic shape starting at Bunch 1 and is segmented into 3+1 parts. There are three so called trains of bunches and a bunch free zone. Almost all buckets of these trains are filled with particles and are colliding bunches. Exceptional some few buckets called pilot bunches are only filled with one type of particles in order to monitor and tune the corresponding beam as they do not collide with the other beam. In the bunch free zone none of the buckets are filled. This give the possibility to imprint reference signals inside the detectors for monitoring and tuning like for gain monitoring systems without interference of background generated by accelerated particles.
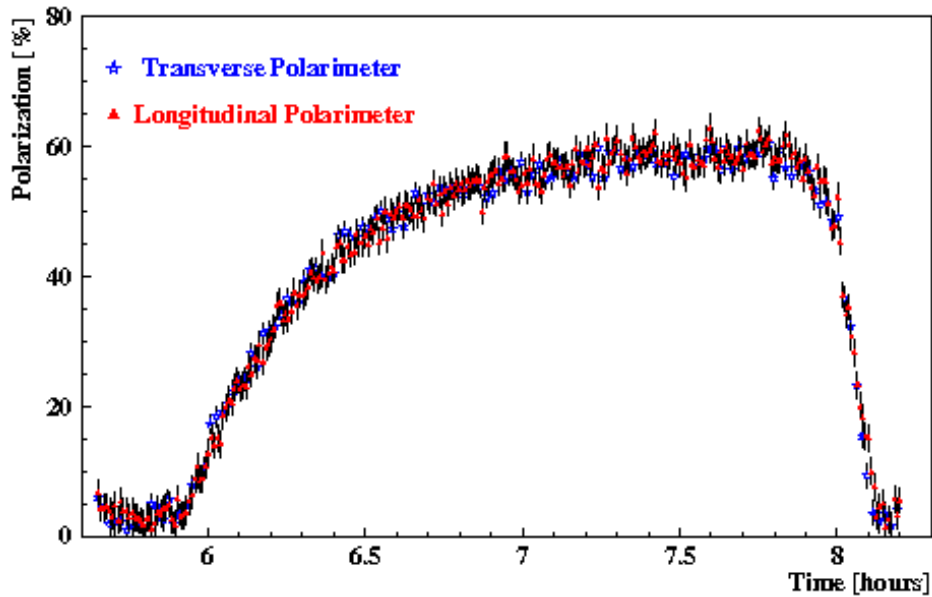

Figure 3.4:   *Self polarization of the lepton beam due to an asymmetry in synchrotron radiation described by Sokolov-Ternov effect and intentional depolarization at the end [Bar+93].*

The proton beam is unpolarized. Due to acceleration in the arcs of high-energy storage rings the helicity of leptons can flip by emission of synchrotron radiation described by the Sokolov-Ternov effect [Ter+61], [Sok+63], [Sok+64]. Due to a small asymmetry in the spin-flip amplitudes the transverse state is preferred which lead to a self polarization of the lepton beam. With the help of spin rotator magnets the helicity can be changed to longitudinal

orientation and vice versa[Buo+86].

Before the upgrade of HERA in 2001 only the HERMES experiment used the longitudinal polarized beam. The accumulated beam spin orientation was in the most time in the transverse state in order to improve the beam polarization. The time independent polarization of the leptons can be described by

$$(3.1) \qquad P_B = \frac{N_+ - N_-}{N_+ + N_-}$$

where N_- and N_+ denote the numbers of the two spin states while the time dependent polarization shown in figure 3.4 increases exponential

$$(3.2) \qquad P_B\left(t\right) = P_B\left(1 - e^{-\frac{t}{\tau}}\right).$$

The theoretical limit of 92 % polarization can not be reached due to these spin rotation and imperfect alignments of the beam line magnets. Instead a typical polarization of around 60 % after 45 minutes is reached.

During the shutdown in 2001 several other spin rotator magnets were installed to provide a longitudinally polarized lepton beam for the collider experiments as well so that the time spending in transverse instead of longitudinal orientation decreased. Therefore the rise time grew slightly and the final average polarization dropped a few percentage.

In order to quantify the polarizations, two polarimeters as shown in figure 3.3 were installed in HERA using Compton backscattering processes. While the location for the transversal polarimeter [Bar+93] is behind the HERA-B experiment in the west, the location of the longitudinal polarimeter [Bec+02] is downstream after the HERMES experiment in the east. By this setup the disturbance to the experiments by monitoring and measuring of the polarization with the polarimeter is minimized and give possibility to recover the beam condition after these impacts. A detailed introduction into the polarimeters can be found in [Ruh99], [Men01].

3.2 Target system

At HERA four experiments have to coexist. This is limiting the degree of freedom for the setup of the target of the HERMES experiment as the life time of the lepton beam for solid materials, as a target, drops too fast. Therefore HERMES is using a gas as a quasi fixed target [Ste+03], [Bau+03b], [Sch+98]. A novel technique of a target storage cell [Due+92] with an active length of $40cm$ has been developed to be used for the experiment. As the beam current roughly follows the shape of an exponential decay

(3.3)
$$I_{lepton}(t) \approx I_{lepton}(0) \exp^{-t/\tau}$$

where τ is the beam life time. If τ_B denotes the beam life time without gas and τ_G the beam life time with gas the density of the gas is selected to match the beam life time contribution of 45 hours under normal conditions. In this case the following equation holds

(3.4)
$$\frac{1}{\tau_G} = \frac{1}{\tau_B} + \frac{1}{45h}.$$

This is the regular running condition. At the end of a fill the density is increased to run one further hour. This high density run increases the rate of data taking by more than one order. Due to the limited life time contribution the target areal density is limited to the order up to 10^{17} protons per cm^2 in contrast to around 10^{24} protons per cm^2 for solid materials.

This technique gives the possibility to change the type of gas at any time. The experiment can be run with polarized or unpolarized gas target. The lighter gases like ^1H, ^2H or ^3He were polarized while the heavier gases like ^4He, N, Ne, Kr, Xe were unpolarized.

An illustration of the target system implemented at HERMES is shown in figure 3.5. In the ABS (Atomic Beam Source) [Nas+03] of the target system a dissociator is used to disjoin molecular Hydrogen or Deuteron gas by radio frequencies to generate an atomic beam gas. The polarization is selected in a set of sextupole magnet system due the Stern-Gerlach-effect before it enters the storage cell in order to interact with the lepton beam. The remaining gas is analyzed to determine the properties of the gas for further analysis In the TGA (Target Gas Analyzer) [Bau+03a] the amount of recombined molecular gas is measured while in the BRP (Breit-Rabi-Polarimeter) [Bau+02] the polarization is measured. A usual transversely target polarization of 78% for hydrogen was usable [Air+05b] and routinely a longitudinal polarization of 97% for hydrogen and 92% for deuterium was available [Nas+03].

As the space in the target area was limited by the apparatus to provide polarized and unpolarized gas targets the recoiling particles were not detected. The full kinematic are computed by the missing invariant mass technique and the kinematic resolutions are therefore limited by the resolution of the forward spectrometer.

3.3 Forward spectrometer

As mentioned before the HERMES forward spectrometer [Ack+98] (figure 3.6) was originally designed to measure the nucleon spin budget. For studies
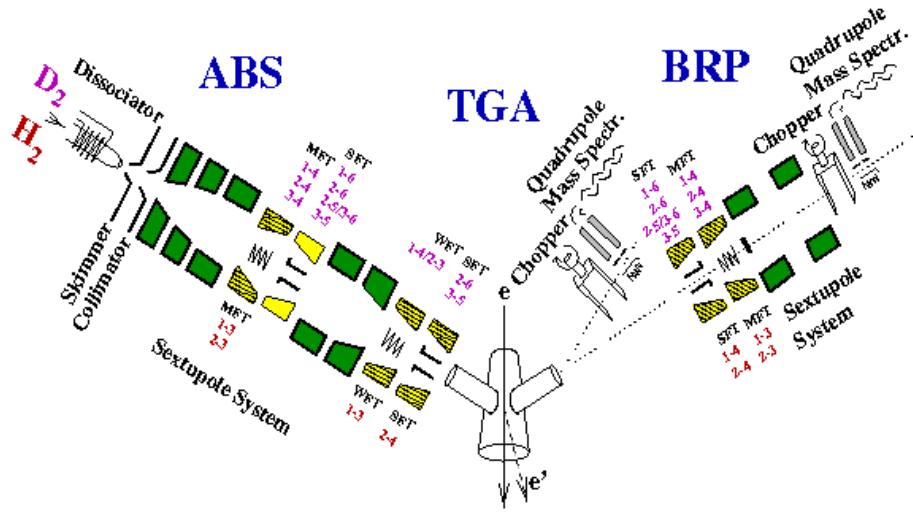
Figure 3.5: *Equipment of the polarized gas target [Bau+03b]. The target gas is dissociated and polarized in the ABS (Atomic Beam Source) [Nas+03] before entering the storage cell. The TGA (Target Gas Analyzer) [Bau+03a] and BRP (Breit-Rabi-Polarimeter) [Bau+02] are used to analyze the remaining gas. A set of sextupols magnets with strong, medium and weak field transitions are used.*

on absolute cross sections or different years of data taking the knowledge about the luminosity is of great importance which is measured with a luminosity monitor. For the reconstruction of interactions with the accompanied particles a system of detectors is established for track reconstruction and for particle identification. For both system a short introduction will be given.

The HERMES forward spectrometer consists of two parts, where the upper and the lower part are symmetric. The configuration of the HERMES detector was modified several times for improvements of particle identification and for extensions of the physics program. After 1997 the Ĉherenkov Counter was replaced by the RICH (Ring Imaging Čherenkov), the damaged VC was removed and DVC was installed. In 2000 the LW (Lambda Wheels) were installed to extend the HERMES acceptance and in 2005 the RD (Recoil Detector) was installed to detect the properties of recoiling particles.

3.3.1 Luminosity monitor

In order to compare and understand the results of physical analysis the knowledge of the absolute luminosity in DIS studies is very important. Target states and beam states have to be combined in order to calculate cross section asymmetries with relative luminosities. Therefore a luminosity mon-
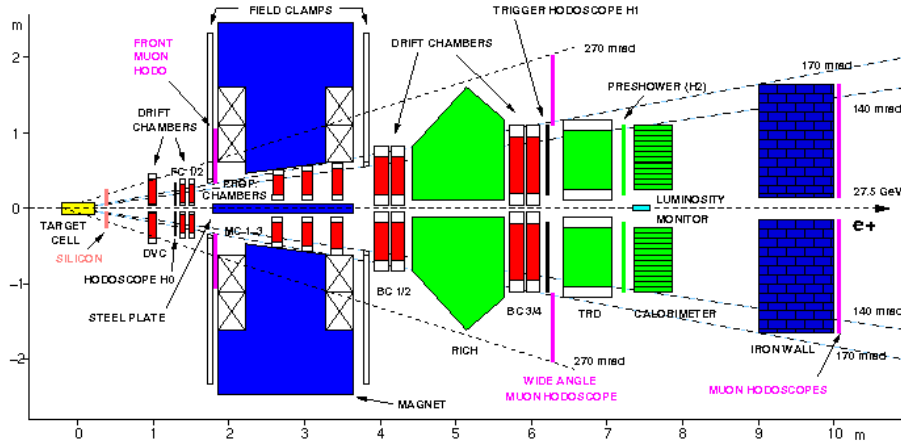
Figure 3.6:   *An illustration of the HERMES forward spectrometer.   The lepton beam enters from the left and interacts with the gas target in the target cell (yellow).   The tracking system consisting of DVC, FC, MC and BC which are colored in red.   The RICH, TRD, hodoscope preshower detector and calorimeter for the particle identification are in green.   The lepton beam is shielded by a septum steel plate.   The Luminosity monitor for absolute normalization is shown in light blue.   The acceptance of the spectrometer is indicated by dashed lines.*

itor was installed [Ben+01], [Ben98].
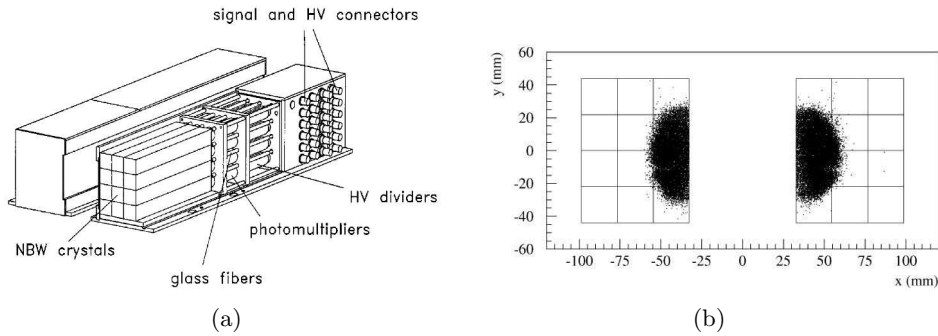
Figure 3.7:   *Luminosity monitor [Ben+01]. (a) The setup of the luminosity monitor for the absolute normalization. (b) Front view of the distributions of reconstructed trajectory of elastic scattered particles.*

In case of a positron beam Bhabha scattering $e^+ e^- \rightarrow e^+ e^-$ and pair annihilation $e^+ e^- \rightarrow \gamma\gamma$ are used to measure the luminosity while for the case of electron beam Møller scattering $e^- e^- \rightarrow e^- e^-$ is investigated.

In both cases the event rate R of these very well known QED processes is corrected for normalization, acceptance and efficiency to determine the absolute luminosity L [Ben+01] by

(3.5)
$$L = \frac{R}{\int_{\Delta\Omega} \Omega \epsilon \, (d\sigma/d\Omega)}$$

where R is the event rate of these processes, ϵ denotes the efficiency and integrated over the acceptance space angle $\Delta\Omega$.
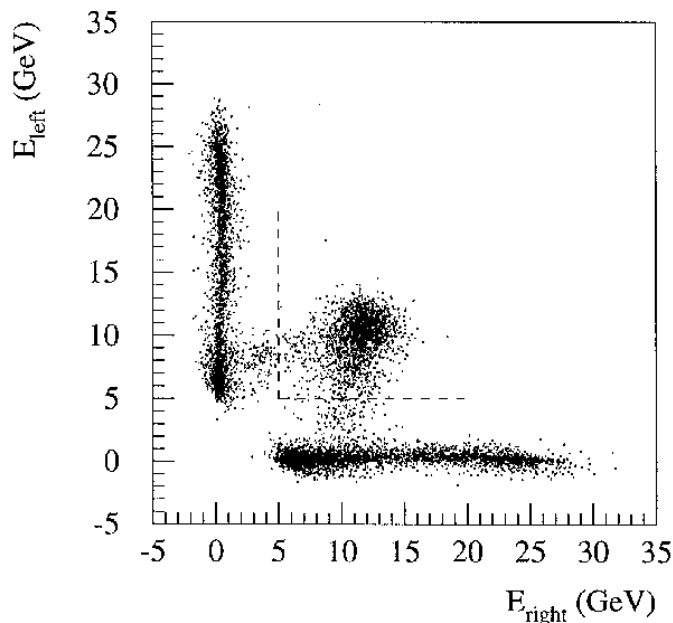

Figure 3.8: *Scatterplot of energy depositions in the right side versus left side. The dashed line separates Bhabha events from background [Ack+98].*

The setup of the luminosity monitor located between the electromagnetic calorimeter is shown in figure 3.7. It consists of a pair of electromagnetic calorimeters left and right of the beam pipe which are moved close to the beam after the data taking was declared to reduce possible radiation damage.

Both are made of a 3x4 matrix of $NaBi(WO_4)_2$ (NBW) Čherenkov crystals each with a size of $22 \times 22 mm^2$ and a length of $200 mm$. The readout is made by photomultiplier tubes of type Hamamatsu R4125Q.

A typical response on elastic scattering is shown in figure 3.8.

3.3.2 Magnet system

The spectrometer magnet consist of two magnets. The main magnet is of the horizontal type with a maximum deflecting power of $\oint Bdl = 1.5 Tm$ for

the momentum reconstruction while the second magnet is a correction coil with an deflecting power of $0.08 Tm$.

The magnet field was modeled and calculated with MAFIA and TOSCA simulation programs and agreed within a few percent with measurements with 3D-Hall probes with an automated 3D-mapping machine. The overall reproducibility of the results are below a permille. This fine 3D-map of the magnet field is implemented into the track reconstruction algorithm as a lookup table.

The main magnet has field clamps in front and behind in order to minimize the fringe field at the position of the drift chambers which are part of the tracking system. For safety and for reduction of power consumption it was running at $1.3 Tm$. With this setup the remaining fringe fields at these positions are below 0.1T. A secondary effect is to protect sub-detectors behind the magnet from synchrotron radiation produced in HERA. The space in the magnet center leaves an acceptance of $\pm (40 - 140)\,mrad$ in vertical direction and $\pm 170 mrad$ in the horizontal direction.

Even if the lepton beam is shielded with an 11cm thick steel plate the main magnet has some effects on the lepton beam. The effect to the proton beam is neglectable due proton beam energy. Therefore a second magnet was installed inside the shielding of the lepton beam pipe. The main two functions of these correction coils are to reduce the disturbance generated by the main magnet and to compensate the transverse component of the lepton beam.

3.3.3   Tracking system

The main task of the tracking system is to reconstruct the tracks and therefore particle momentum as illustrated in figure 3.9. Additionally the corresponding hits in the detectors for particle identification can be correlated. Furthermore the kinematics due to the deflection by the magnet can be determined.

The geometrical resolution of a fully operational tracking system is limited by Bremsstrahlung while passing the wall of the target cell for electrons, of the stainless steel vacuum window and of the first tracking detectors. The tracking system is shown in the figure 3.6 in red color. It consists originally in downstream direction of VC (Vertex Chambers), DVC (Drift Vertex Chambers), FC (Front Chambers), MC (Magnet Chambers) [And+01] and BC (Back Chambers) [Ber+95], [Ber+98]. In 1998 the damaged VC was removed and in 2000 the LW (Lambda Wheels) were installed to increase the acceptance of the HERMES forward spectrometer.

VC

The VC 3.6 is a micro strip gas chamber for high precision reconstruction downstream right after the target cell area and is therefore very close to the beam pipe. The stripe width of $7\mu m$ and a distance of $193\mu m$ yields in a very narrow resolution of around $65\mu m$. Due to an accident during beam dump the VC was seriously damaged and therefore removed in 1998 in order to minimize further disturbance.
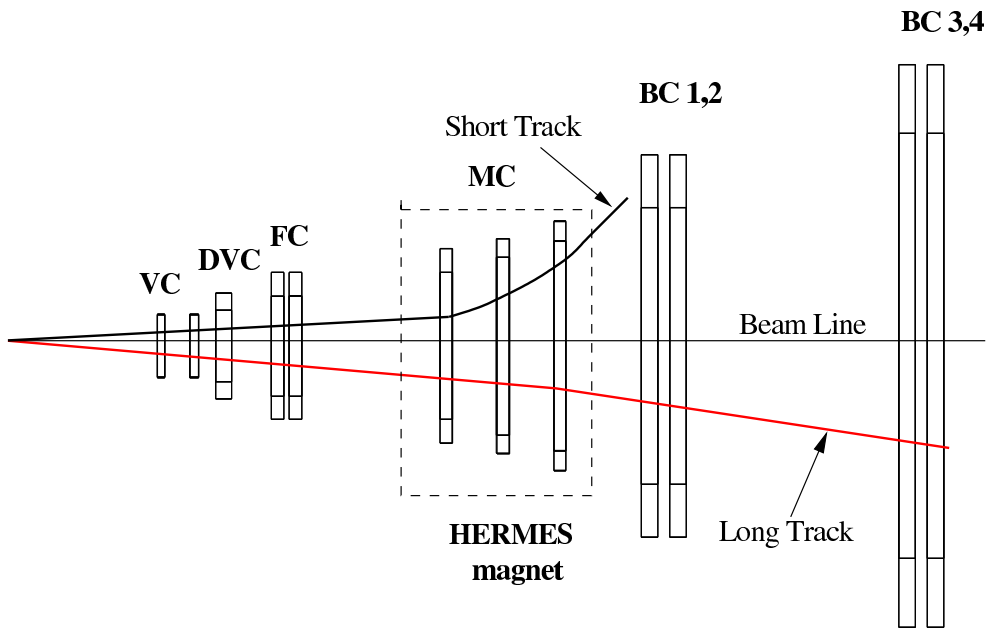

Figure 3.9: *Schematic illustration of the tracking system. Long tracks reaching all tracking detectors, while short tracks are deflected by the HERMES magnet out of the acceptance of the BC.*

Drift chambers and proportional chambers

In order to simplify the handling all the other detectors for tracking consist of drift chambers built as a sandwich of three planes with vertical or $\pm 30^0$ tilted wires. The DVC (Drift Vertex Chambers) and FC (Front Chambers) [Bra+01] in front of the magnet is used to reconstruct the front part of the tracks, while the BC (Back Chambers) [Ber+95], [Ber+98] behind the magnet are used to measure the back part of the tracks. By combining these information the momentum of the charged particles can be measured due to deflection in magnet field.

The chambers has for simplicity the same setup and running with the same gas mixture of $Ar\,(90\%)\,CO_2\,(5\%)\,CF_4\,(5\%)$ which provides very high

drift velocity and is non-flammable for security.

Even this tracking are very accurate to determine the momentum the MC (Magnet Chambers) [And+01] is of great help to resolve ambiguities of track finding and to measure low momentum particles which does not reach the back part of the spectrometer which are called short tracks. The MC which has to operate in strong magnet field has slightly different setup. It is built as MWPC (Multi Wire Proportional Chamber) with a optimized gas mixture of $Ar\,(65\%)\,CO_2\,(30\%)\,CF_4\,(5\%)$.

For the readout of the detectors ASP (Amplifier-Shaper-Discriminators are used to digitize by Fastbus Multihit TDC with a time accuracy of 0.5ns. With the usual wire diameter of around $25\mu m$ and at a distance of few mm results in a spatial resolution of around $300\mu m$ per plane. The resolution of the momentum reconstruction was between 0.7% to 1.25% before 1998 and was since then between 1.5% to 2.5% due to dismount of the precise but damaged VC and as furthermore it was decided to put an additional material (aerogel) for the new RICH into the track path. These modifications were made to enhance the physics program of the HERMES detector.

LW

Last upgrade of the tracking system was the LW (Lambda Wheels) detector based on silicon wafer and located behind the target cell in order to extend the acceptance of the forward spectrometer and to detect λ-hyperons in wide kinematic domain. Detailed informations about the setup can be found in [Hee03] and recent results are documented in [Dem07], [Rei07].

Track reconstruction

Due to the simple setup of the tracking system the track reconstruction can be done very efficiently by a tree search for the track finding and by a fast momentum determination with a look-up table for the track kinematics [Ack+98].

The tree search algorithm as illustrated in figure 3.10 works very fast and simple. The possible window for the track pattern are bisectioned in each step. As the tracking detector has a size of around three meters and a resolution of around $250\mu m$ after around 14 iterations the binary tree search determinate independently for the front part and the back part of the HERMES spectrometer into partial tracks. These front partial tracks are combined within specific spatial tolerance to find back partial tracks which have a starting vertex near the interaction region and reaching the other detector of the particle identification system.

After the track finding the momentum reconstruction is done by combining tracking information in front and behind the magnet as charged particles are deflected while passing through magnetic fields. Under normal condi-

tions the reconstruction in an inhomogeneous magnet field requires usually a high amount of calculations.

The HERMES track reconstruction uses a simple look-up table to reconstruct the momentum which contains all relevant informations of space points before and after the magnet with a relative momentum resolution contribution of less than $\delta p/p \sim 0.5\%$. The table has around 0.5M entries. This momentum reconstruction algorithm is therefore very efficient and require only low performant computer hardware.

Alignment

The resolution of the tracking system depends essential on a proper alignment of the sub detectors. In order to align the tracking system dedicated runs were taken without a magnet field to gain straight tracks to measure the relative position of the detectors. Due to the simple layout of the chambers a simple tree backtracking algorithm can be applied to determine the relative offsets.

Additionally a laser tracking system [Shi+98] is used to monitor online relative movements of the detector. Due to the ramping of the magnet unpredictable movements of the detectors can been detected and corrected in situ.

The K_s meson decay can be used to check the absolute calibration of the spectrometer and the performance of the tracking system. The result shown in figure 3.11 gives a very good agreement with the PDG (Particle Data Group) [PDG08] on one part of permille accuracy.

3.3.4 Particle identification

The major interaction of particles passing through material is ionization, Bremsstrahlung, pair production or Čherenkov radiation. The amount of energy deposition or deflection of charged particles depend on the mass, charge and momentum of the passing particle and therefore particle identification is possible.

The system for particle identification, one of the key features of the HERMES detector, consist of four detectors. Due to this complementary combination the HERMES detector has a very good particle separation. These detectors are RICH (Ring Imaging Čherenkov) [Asc+00], [Ako+02], TRD (Transition Radiation Detector) [Eme96],[Thi96], hodoscope preshower detector and an electromagnetic calorimeter [Ava+98].

RICH

The RICH [Ako+02] illustrated in figure 3.12 replaced the threshold Ring Imaging Čherenkov counter in 1998 and allows to provide very efficient separation of pions, kaons and protons by Čherenkov radiation in a wide mo-
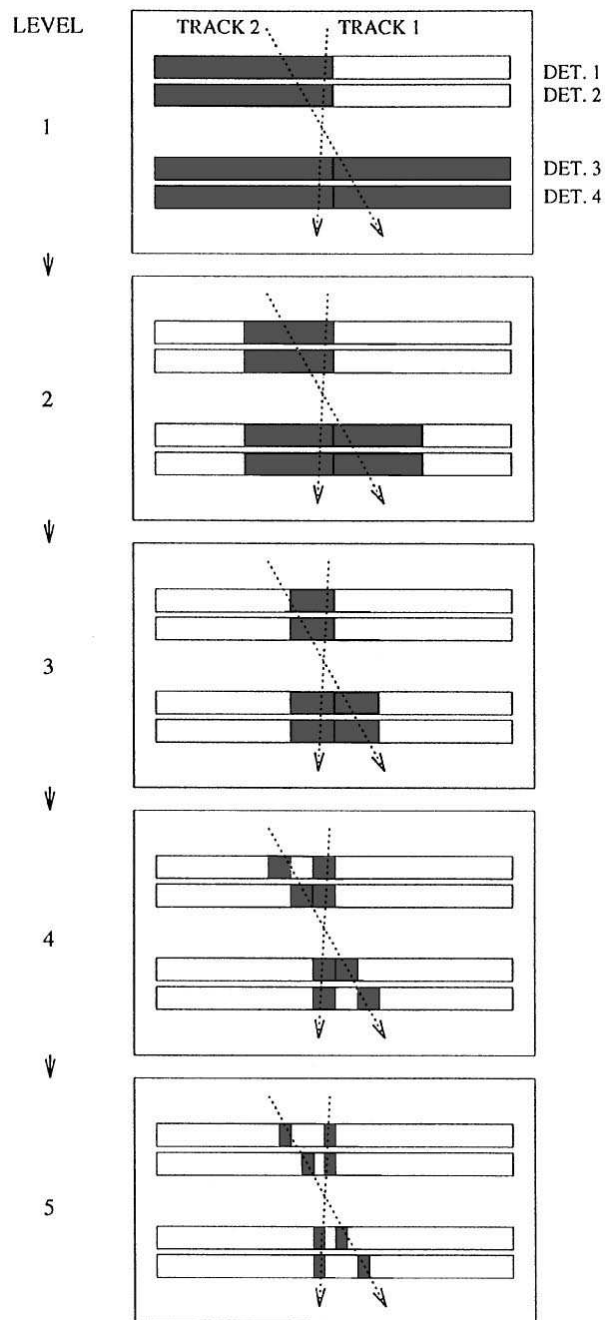
Figure 3.10:   *Illustration of the HERMES track finding algorithm [Ack+98] by bisectioning tree search in each iteration step. The resolution is step wise doubled to determine the trajectories of the tracks.*
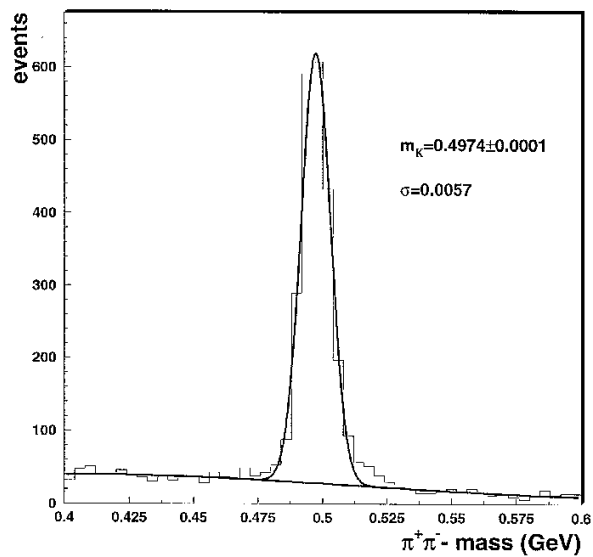
Figure 3.11:   *The invariant mass of $\pi^+\pi^-$ pairs [Ack+98]. The reconstructed K_S mass (497.4MeV) agrees very well with the PDG value (497.7MeV).*
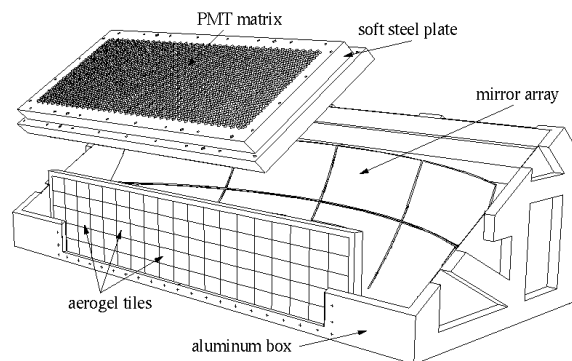

Figure 3.12:   *The setup of the upper half of the RICH (Ring Imaging ČHerenkov) detector [Ako+02] which is one of the key part of the particle identification. The bottom half has similar construction.*

mentum range. The characteristic angle θ_C of the light cone is correlated with the speed of the particle thus with the momentum by

$$\theta_C = \frac{1}{n\beta} \tag{3.6}$$

where n denotes the refractive index of the material while $\beta = v/c$ with v
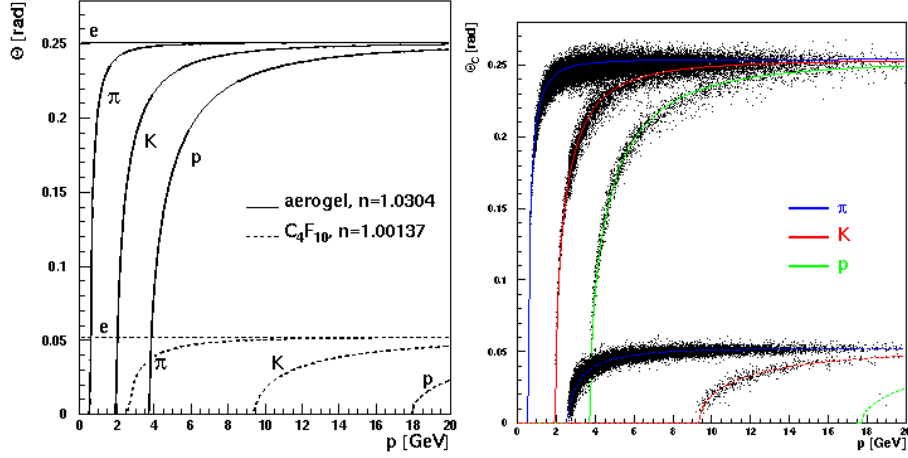
Figure 3.13:   *The angle of the Čherenkov cone versus the momentum for the major particle types are shown. On the left side the Monte Carlo simulation is shown as well as on the right side real data are included [Haa07].*

as speed of particle and c as speed of light.

As shown in figure 3.13 the RICH can contribute to separate leptons and hadrons for momentums below $4GeV$ very well. As the lepton energy spectrum for analysis of exclusive events has it's main contribution above $5GeV$ the RICH is not taken into account for this work. A very detailed description of the RICH detector can be found in [Asc+00] and [Ako+02].

TRD

Charged particles passing different dielectric mediums produce radiation on the transition in order to match the different Coulomb field in the material. The mean energy E of the radiation in case of ultra-relativistic condition can be expressed as

$$(3.7) \qquad\qquad E = \frac{2}{3}\alpha_{em}\omega_P\gamma$$

where $\alpha_{em} = 1/137$ is the electromagnetic fine structure constant, γ is the Lorentz factor and ω_P is the plasma frequency.

The transition radiation is emitted in a cone around the particle trajectory with an opening angle of $\theta = 1/\gamma$. As the Lorentz factor γ for leptons are much higher due to the larger mass than for hadrons this allows a lepton hadron separation by energy deposition.

As the probability for a transition radiation is very small a large amount of transitions of material is required. This can be done by a sandwich design as illustrated in figure 3.14.
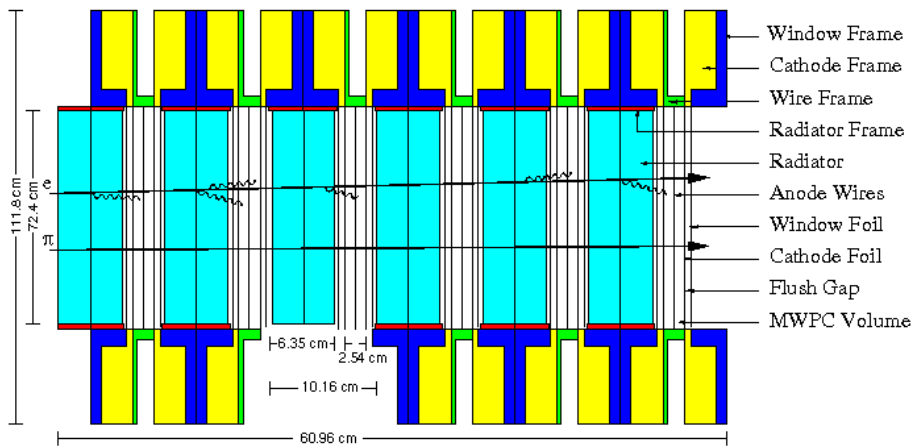
Figure 3.14:   *The upper half of the TRD [Ack+98] setup is illustrated with a lepton and pion trajectory. The opening angle of the lepton path is due to better visibility not to scale.*

The TRD setup consists of six independent modules with an active area of $72.4 \times 325 cm^2$. Each modules has a sequence of radiator and PWC (Proportional Wire Chamber) in order to provide informations about energy deposition and location. The radiator with a thickness of $6.35cm$ is built by fibers with $17\mu m$ to $20\mu m$ diameter and a density of $0.059g/cm^3$. This corresponds to an average of 267 dielectric layers. The PWC has a conventional design with 256 vertical wires of $75\mu m$ gold-coated Be-Cu-compound material separated by $1.27cm$. For an easy in situ replacement the wires are crimped and are positioned with an accuracy of $25\mu m$. The chambers has a thickness of $2.54cm$ and was filled with $Xe\,(90\%)\,CH_4\,(10\%)$ detector gas for highly efficient X-ray absorption.

The analog signals are amplified and transmitted as differential signal with twisted-pair flat cables to the Fastbus ADC for readout. The response for a single TRD module and for a truncated mean of six TRD modules are shown in figure 3.15.

Electromagnetic calorimeter

The electromagnetic calorimeter shown in figure 3.16 has two functions to provide a first-level trigger for scattered beam leptons and to provide particle identification for the off-line analysis.

It consists of radiation resistant lead-glass called F101. Each of the upper and lower walls was built with 42 times 10 blocks with a active area of $9x9cm^2$ each. The length of such a block is $50cm$ which is about 18 radiation lengths. In order to minimize optical cross talks between the blocks they
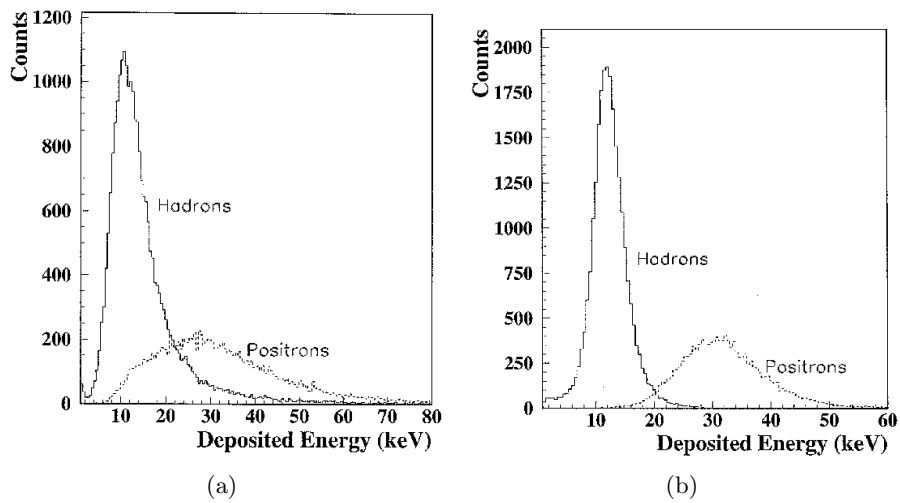
Figure 3.15: *Response of TRD [Ack+98] for leptons and hadrons as count versus energy deposition, integrated over all momentums. (a) Response for a single TRD module. (b) Response for truncated mean of six TRD modules.*
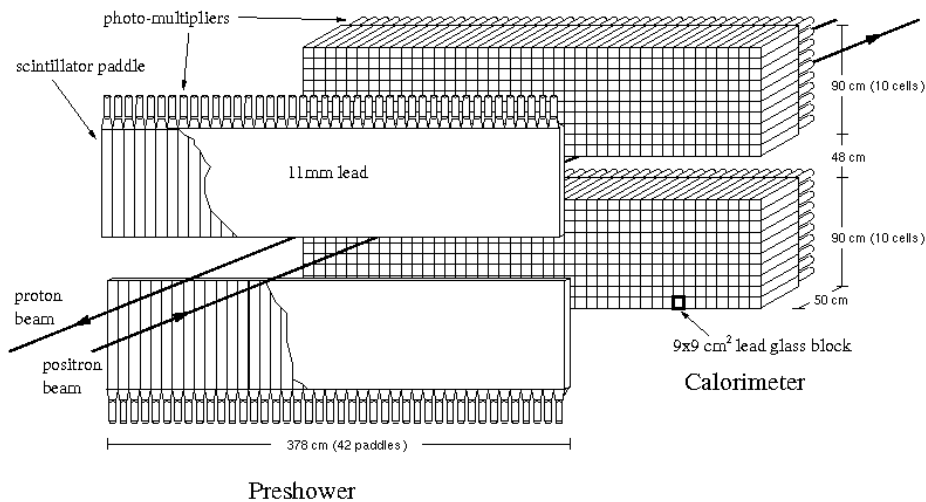

Figure 3.16: *Illustration of the electromagnetic calorimeter together with the hodoscope preshower detector H2 in front [Ack+98].*

are covered on the side with $51\mu m$ thick aluminium mylar foil and with $0.127mm$ thick tedlar foil. Each block has a PMT (Photomultiplier tube) of type Philips XP3461 on the downstream side. In order to prevent radiation damage both walls are moved in a distance of $50cm$ to the beam during injection.

The performance of the calibration of the electromagnetic calorimeter is shown in figure 3.17. The energy E is measured by the electromagnetic calorimeter while the momentum p is reconstructed by the tracking system of the forward spectrometer. The ratio $r = E/p \approx 1.00 \pm 0.01$ demonstrate the $\approx 1\%$ uniformity of the response. The long term stability is of the same order and includes the effect of radiation damage over the years as well.

In order to check the overall calibration the reconstruction of the π^0 decay is used. The reconstructed π^0 mass from 2γ events are shown in figure 3.17 and is in good agreement with the PDG (Particle Data Group) value. A more detailed description of the electromagnetic calorimeter can be found in [Ava+98].

(a)   (b)
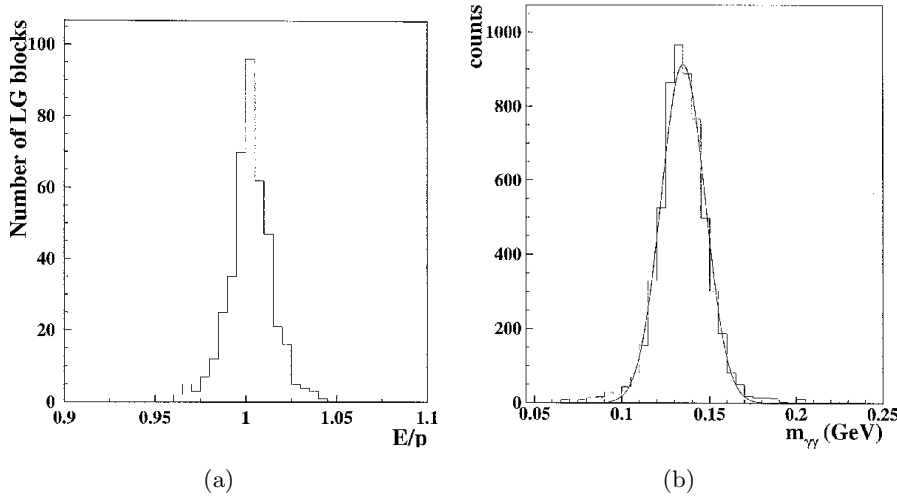
Figure 3.17: *Performance of the electromagnetic calorimeter [Ack+98]. E are the measured energy while p is the reconstructed momentum. (a) Distribution of E/p with center value 1.00 and with width 0.01. (b) Distribution of π^0 mass reconstructed from 2γ cluster event. The fit with a gaussian distribution yields to the center $(134 \pm 0.2)\,MeV$ and to the sigma $(12.5 \pm 0.2)\,MeV$ and is in good agreement with the PDG value.*

The hodoscope for trigger and PID

The hodoscope detectors H0, H1, H2 consist of fast plastic scintillators. They are mainly employed as trigger detectors. On the other hand they contribute to particle identification by measuring energy deposition as well. The setup of the lower and upper hodoscopes are identical.

The location of the H0 is in front of the HERMES magnet and has a active area of $60x20cm^2$ and a thickness of $3.2mm$ as illustrated in figure 3.18. Each H0 is readout by two PMT of type Thorn EMI 9954SB.

The hodoscope H1 is before and the hodoscope H2 is behind the TRD as shown in figure 3.6. Each hodoscope has the same setup as shown in figure 3.16 and consist of 84 vertical scintillator modules which are $1cm$ thick and has an active area of $9.3x91cm^2$ of a fast scintillator material with large attenuation length of $300cm$ to $400cm$. The modules have an overlap region of around $2cm$ to $3cm$ to maximize efficiency. The hodoscope H2 has additional a passive radiator consisting on $11mm$ (2 radiation lengths) of Pb with $1.3mm$ stainless steel in front.

Each of the scintillating modules are readout with a PMT of type Thorn EMI 9954SB and provide together with H0 fast signals for first level trigger.

With this setup a striking lepton produces a broad distribution of deposited energy with a mean of $20MeV$ to $40MeV$ which has a weak dependency on the energy of the passing lepton. In comparison to around $2MeV$ by a pion this gives the opportunity to separate hadrons from leptons clearly as shown in figure 3.18.

(a)   (b)
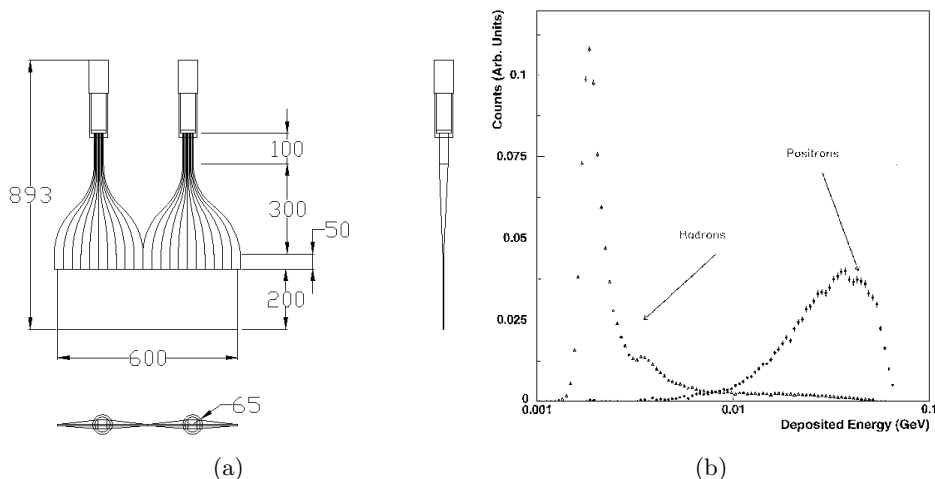
Figure 3.18:   (a) Technical drawing of the hodoscope H0 which is mainly used for the first level trigger. (b) Response of hodoscope preshower detector H2 which utilize particle identification by energy deposition.

PID performance

The performance of the particle identification system in shown in figure 3.19 where the PID value represents the accumulated informations of the contributing detectors about the particle. A very detailed description of the PID value which is a likelihood estimation can be found in [Kai+97], [Wen99], [Wen01].
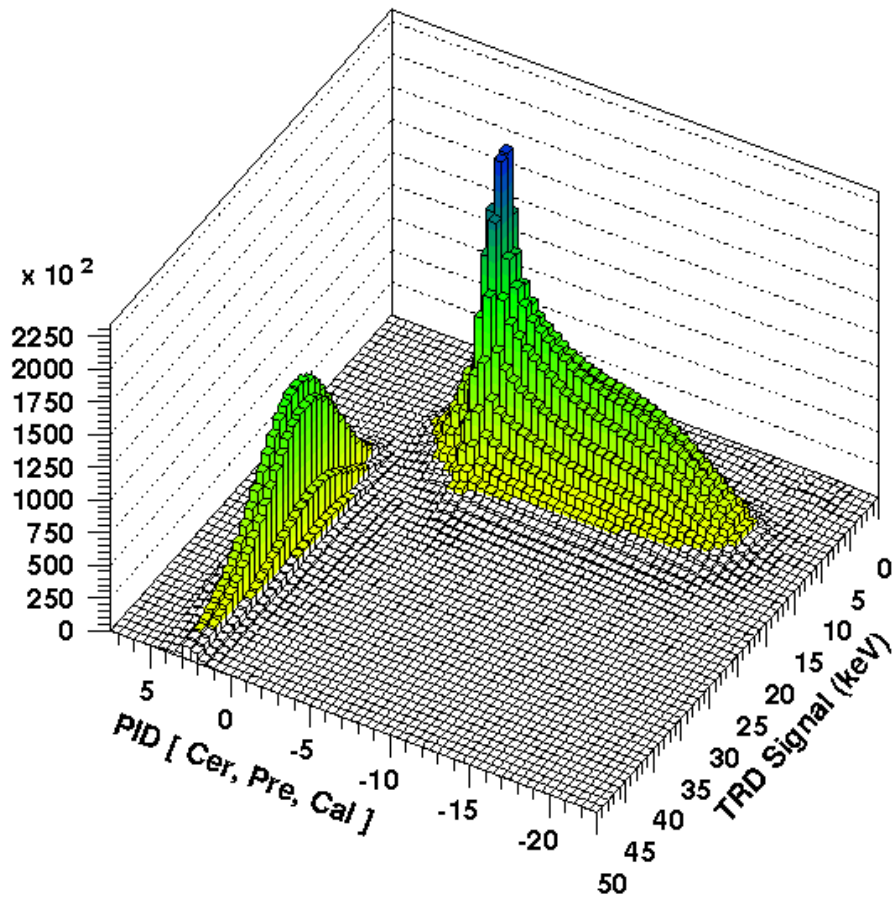
Figure 3.19: *The performance of the PID system [Ack+98] shows a clear separation between leptons and hadrons. The leptons are located left while the hadrons are on the right side.*

Chapter 4

The Recoil Detector

To improve the exclusivity and the resolution of the kinematic variables the HERMES collaboration decided to upgrade the HERMES Detector with the RD (Recoil Detector)[Kai+02], [Sei04] to detect the recoiling particles directly. To install the RD the equipment for the polarized gas target had to be removed as illustrated in figure 4.1. During the maintenance shutdown in winter 2005 the Recoil Detector was installed in front region of the HERMES detector and data taking was running until the HERA shutdown in June 2007. The readout implementation of the SFT (Scintillating Fiber Tracker) which is one of the key part of the RD and the readout integration of the RD into the HERMES data acquisition are the main part of this work.

(a)   (b)
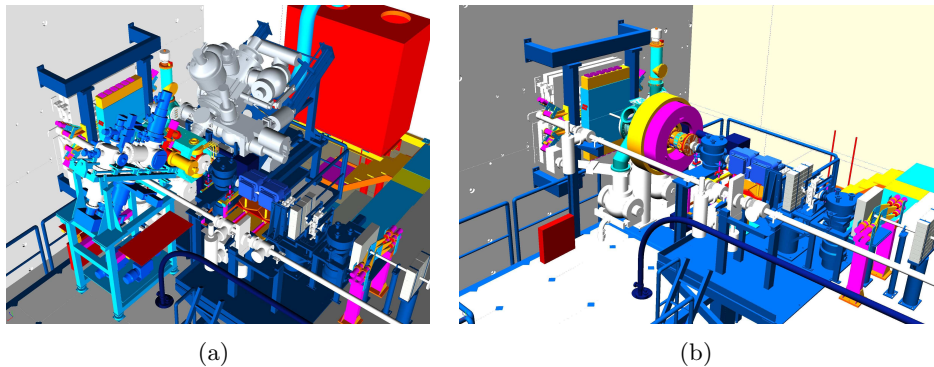
Figure 4.1:   *The HERMES Detector front region before (a) and after (b) the installation of the Recoil Detector as 3D illustration gives a good impression about the space limitation.*

4.1   Design requirements and realization

The resolution of the DVCS kinematics and the suppression of background is limited in the HERMES forward spectrometer by the electromagnetic calorimeter and the impossibility of the detecting the recoiling particle. The aim of the Recoil Detector is therefore to enhance the event selection to improve the kinematic resolution for physical analysis and to be able to make the events more exclusive. This is done by detecting and reconstructing the properties of the recoiling particles directly. Furthermore the event selection is improved by suppression of background.

Extensive Monte Carlo studies on reactions of the type

$$eN \rightarrow e'\gamma X \tag{4.1}$$

with e as incoming lepton, e' as scattered lepton, γ as the produced real photon, N as target nucleon and X as rest of products were carried out in order to determine selections for exclusive reactions. The remaining invariant mass M_x^2 of the squared four-momentum properties of the known particles can be expressed as

$$M_x^2 = p_e^2 + p_N^2 - p_{e'}^2 - p_\gamma^2 \tag{4.2}$$

where p_e and $p_{e'}$ are the four momentum of the incoming and scattered lepton, p_N denotes the four momentum of the off scattered nucleon target and p_γ is the four momentum of the produced real photon.
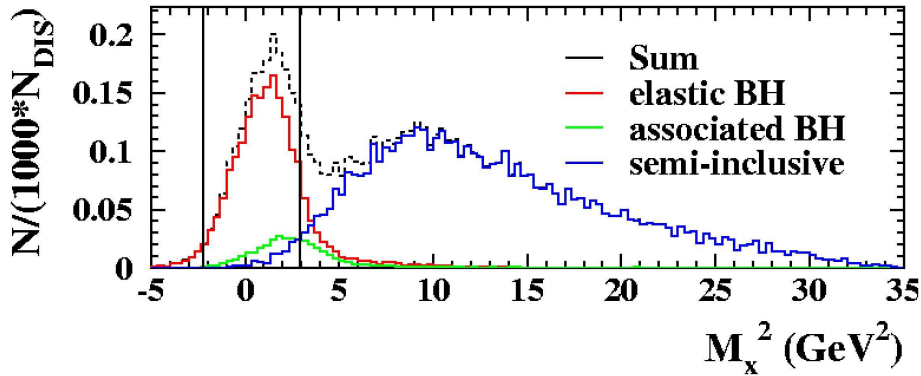
Figure 4.2:   *Missing invariant mass distribution for different reactions. The vertical lines constraints the event selection to* $-2.25 \leq (M_x/GeV)^2 \leq +2.89$.

The contribution of different types of reactions are shown in figure 4.2. For the exclusive event selection the used range of the missing invariant mass is

$$(4.3) \qquad\qquad -2.25 \leq (M_x/GeV)^2 \leq +2.89.$$

The contribution by associated Bethe-Heitler process also called Δ-resonance is in this case around 11%, while the contamination by semi-inclusive processes are around 5%.

These Monte Carlo studies [Kra05] indicate the requirement to detect recoiling protons in the momentum range between $50MeV$ up to $1400MeV$ which are illustrated in figure 4.3. The dependence particle momentum p versus the polar angle θ for several alternative reactions are shown. Additional properties of the Recoil Detector are summarized in table 4.1.

Parameter	Unit	Ideal Performance	Expected Performance
p-acceptance	MeV/c	50-1400	106-450 (SSD) 250-1400 (SFT) 600-1400 (PD)
θ-acceptance	rad	0.1-1.35	0.4-1.35 (SSD) 0.7-1.35 (SFT) 0.78-1.90 (PD)
ϕ-acceptance	rad	2π	4.8 (SSD) > 4.8 (SFT) > 4.8 (PD)
p-resolution	1	$< 10\%$ 5%	3-9% for $p < 500MeV/c$ 13% for $p > 500Mev/c$
t-resolution	GeV^2	< 0.07	0.01-0.07 for $t < 0.03$ $0.07 - 0.2$ for $0.3 < t < 10$
ϕ-resolution	rad	< 0.05	0.031 (SSD) 0.008 (SFT) 0.1 (PD)
π/p PID range	MeV/c	50-800	135-650
π^+ rejection factor	1	> 10	> 10 for $p < 650MeV/c$
Δ suppression	1	$> 90\%$	92%

Table 4.1:   *Summary of the properties of the Recoil Detector and for the sub detectors if available [Kai+02], [Hoe06].*

By combining a Silicon Strip Detector, a Scintillating Fiber Tracker and a Photon Detector inside of a 1T magnetic field the momentum of the detected particles can be reconstructed and allowing particle identification. A schematic overview of the Recoil detector is shown in figure 4.4.
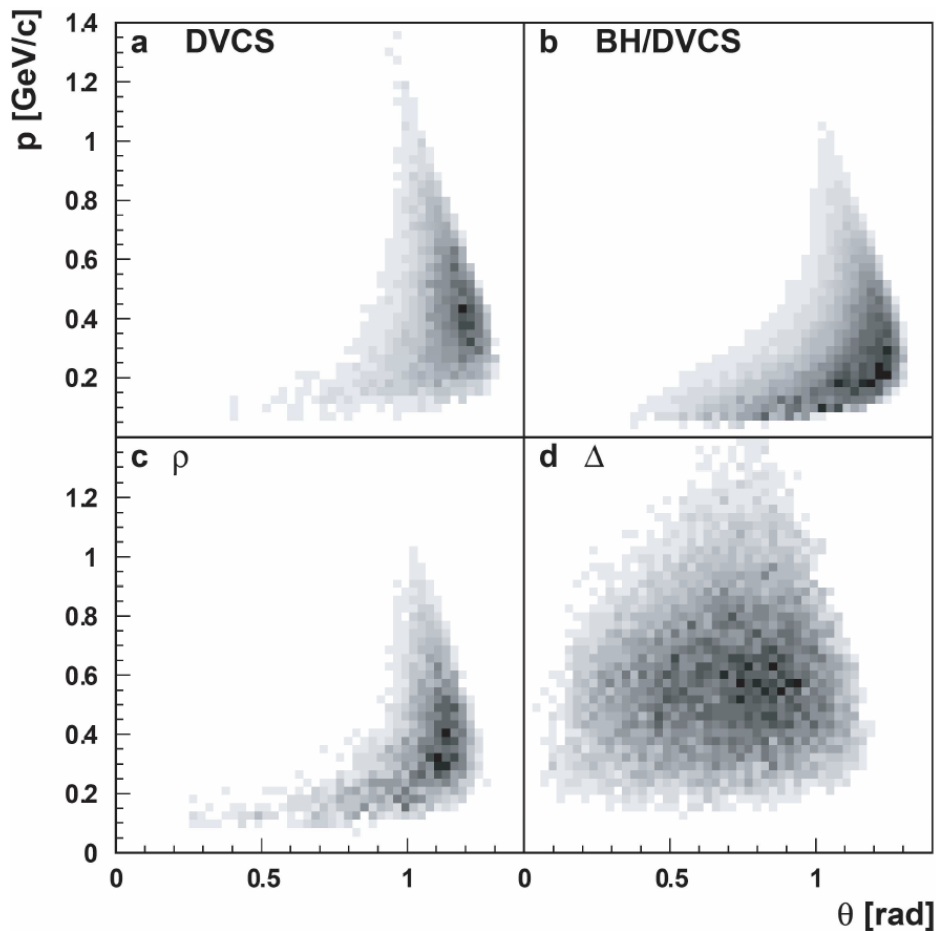
Figure 4.3:   *Distributions of particle momentums p versus polar angle θ studied with Monte Carlo simulations for (a) DVCS process, (b) DVCS / BH interference term, (c) ρ-meson production and (d) Δ resonances or associated BH-process [Vil08].*

The drawback for these improvements of the HERMES forward spectrometer is the removal of the polarized gas target due to limited space in the front region of the HERMES detector. The remaining data taking by the HERMES experiment until the shutdown of HERA in 2007 was done therefore with unpolarized gas of hydrogen and deuterium. The installation of the Recoil Detector into the HERMES detector is shown in figure 4.5. To take the new spatial dimensions of the RD and the different target gas system into account a new target cell was built.

The Recoil detector is a collaborative effort with contributions by

- Infrastructure by
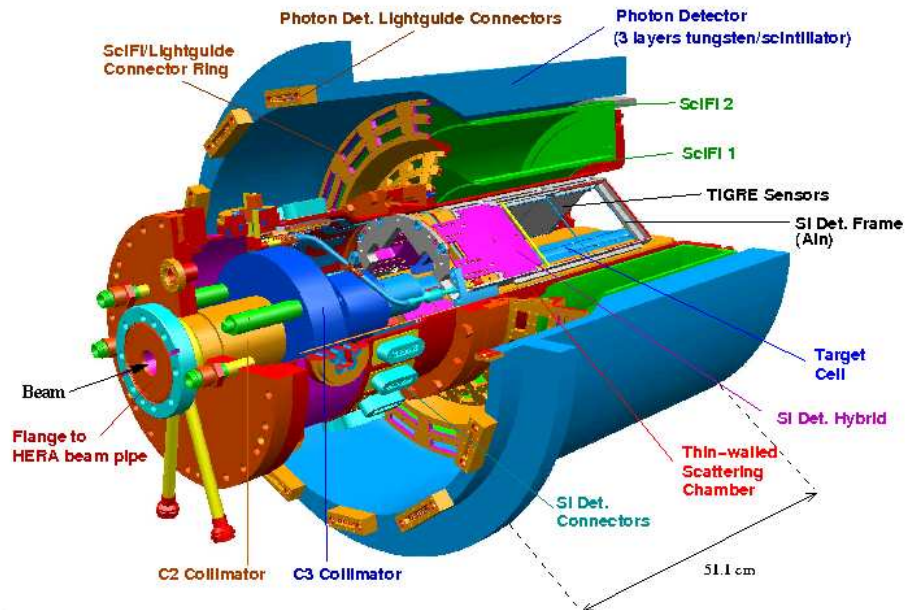
Figure 4.4: *Overview of the Recoil Detector.*
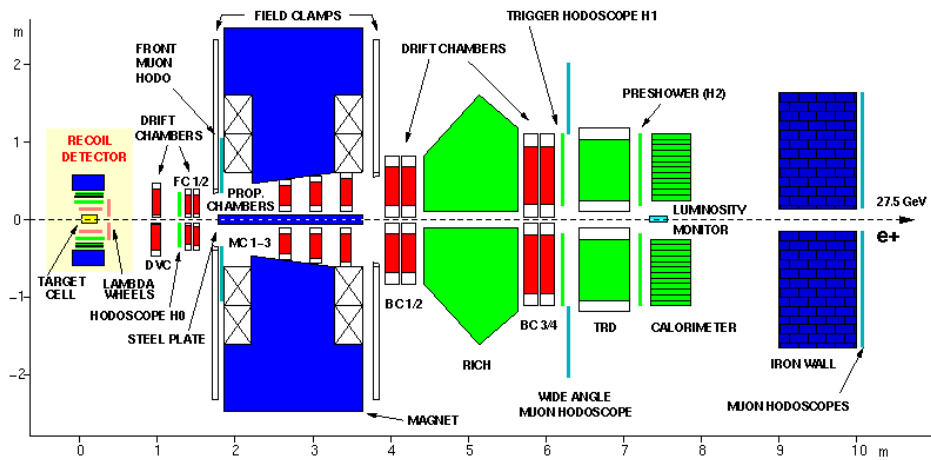
Figure 4.5: *HERMES forward spectrometer upgraded with the Recoil Detector.*

DESY Hamburg / Germany

- TC (Target Cell) by
  INFN Ferrara / Italy

- SSD (Silicon Strip Detector) by

DESY Zeuthen / Germany
University of Erlangen / Germany
University of Glasgow / Scotland

- SFT (Scintillating Fiber Tracker) by
University of Giessen / Germany

- PD (Photon Detector) by
LNF Frascati / Italy
University of Gent / Belgium

- SCM (SuperConducting Magnet) by
PNPI St. Petersburg / Russia

4.2   Target cell

The target cell have to be adjusted to face the new dimensions of the RD
but the major shape remains. The new target cell was produced like the
previous ones by the target group [Air+05b] is shown in figure 4.6.

As described before the effective length of the target cell was before
$40cm$. This value is now $30cm$ which matches roughly the size of the active
part of the SSD (Silicon Strip Detector) which stay in the HERA beam pipe
vacuum. The thickness of the target cell made by thin aluminum foil was
originally $50\mu m$. An accidental damage of the thin foil due to thermal and
mechanical stress caused indirect serious damage in the SSD. A new target
cell was built with $75\mu m$ thickness and installed during the last maintenance
shutdown of HERA in June 2006.

Several collimators in front of the Recoil Detector protects the target cell
and the Silicon Strip Detector from synchrotron radiation. The scattering
chamber covering the active area of the Recoil Detector and enclosing the
vacuum region are $1.2mm$ thick and is the other reason for the lower limit
of the momentum of detected protons.

The previous cooling for the polarized gas target was running with liquid
helium in order to improve the target polarization and for a precisely and
stabled polarized gas. Running the experiment with unpolarized gas the
need for this expensive and difficult cooling with liquid helium is obsolete.
This simplifies the construction and servicing of the target cell. While run-
ning the gas target around room temperature the cooling can be done with
water and the thermal stress can be significantly reduced. Beside this the
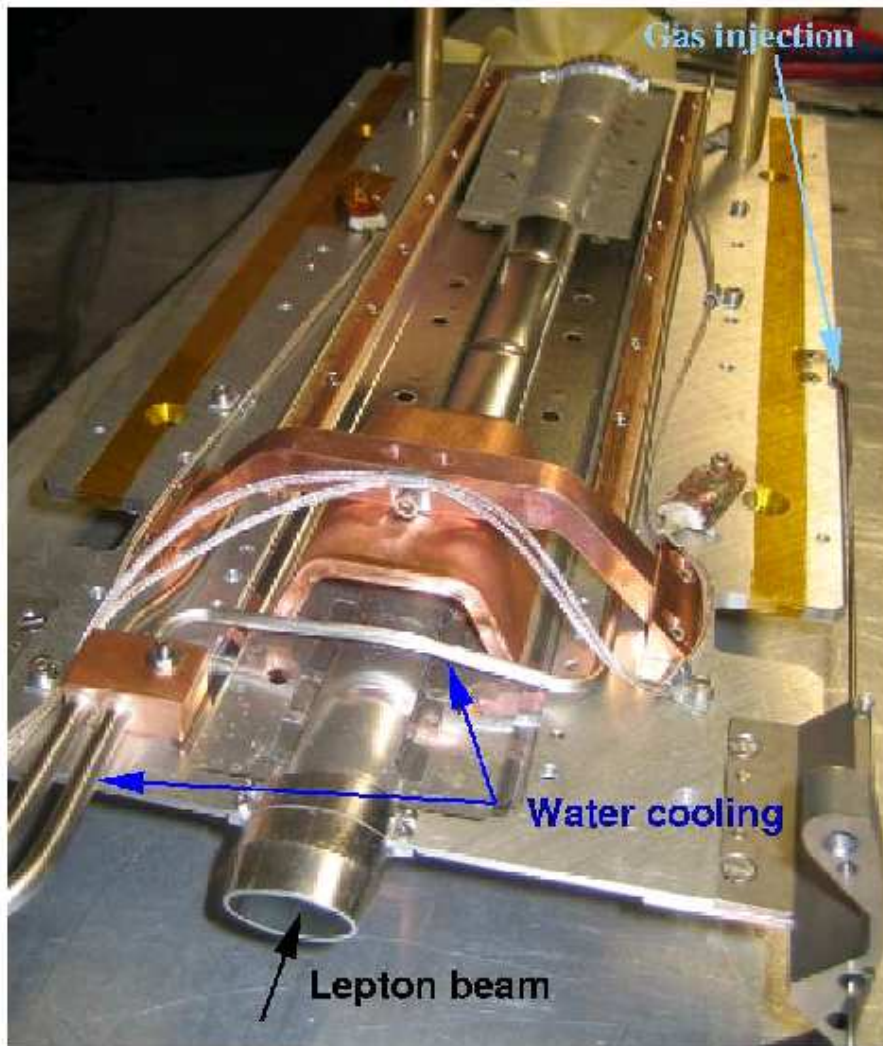control of the temperature is better as well.

Figure 4.6:   *The new adjusted target cell which fits the requirements of the Recoil Detector.*

4.3   Silicon Strip Detector

Due to the design requirements studied with Monte Carlo simulations the material budget in front of a detector has to be minimized In order to detect very low momentum particles. For this the SSD (Silicon Strip Detector) [Pic08], [Vil08] is mounted inside the HERA beam vacuum with a pressure of around $10^{-9}mbar$ and is one of the key parts of the RD. This way of implementation yields to measure protons with momentums as low as $50MeV/c$.

As shown in figure 4.7 the response of silicon for passing protons de-
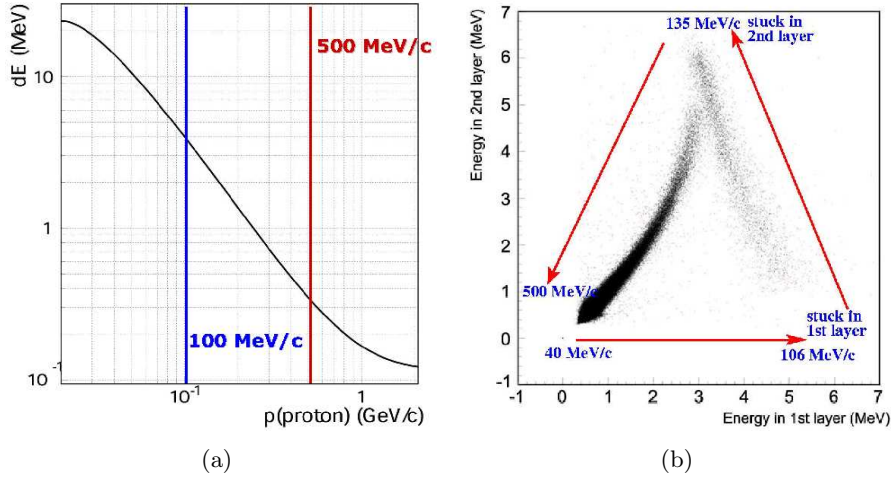
Figure 4.7: *Response of a $300\mu m$ silicon layer on proton penetration. (a) Bethe Bloch formula [PDG08], [Vil08] gives the energy deposition response versus incident proton momentum. The two vertical lines illustrate the designed active range of the silicon modules for the SSD. (b) The arrows indicate increasing proton momentum [Haa07]. Protons with momentum range $40MeV/c$ to $106MeV/c$ mostly stuck in the first layer. Protons with momentum range $106MeV/c$ to $135MeV/c$ mostly stuck in the second layer. Protons with momentum above $135MeV/c$ passes both layers.*

scribed by the Bethe-Bloch formula is very simple. The momentum of the recoiling proton can be reconstructed by energy deposition due to ionization. Combining two layers of silicon improves the momentum resolution. The typical triangle shape of response can be separated in three parts. The first part is due to stopped particle with very low momentum from $40MeV/c$ to $106MeV/c$ in the first layer without a response in the second layer. In the second part the particle with momentum range of $106MeV/c$ to $135MeV/c$ passes the first layer but stuck in the second layer. In the third part particles in the momentum range from $135MeV/c$ passes both silicon layers.

The setup of the SSD consists of eight SSD modules as illustrated in figure 4.8 which are built in a diamond shape with an inner and an outer layer. Each SSD modules has two double sided silicon wafers called TIGRE sensors with parallel or perpendicular orientation of the 128 strips on each side. Each of the silicon wafer with thickness of around $300\mu m$ has an active area of $10 \times 10mm^2$. Each strip has a pitch width of $758\mu m$ and a distance of $56\mu m$ to the neighboring strips.

This provides two space points per track for track reconstruction with a resolution of around $222\mu m$ and particle identification for the momentum range from $106MeV/c$ up to $500MeV/c$. As the wafers are a few cm away

from the beam the polar angular acceptance are between $0.1rad$ and $1.35rad$. Due to the ceramic frame which holds the silicon sensors the azimuthal angular acceptance is around $\sim 70\%$.

<div align="center">(a)   (b)</div>
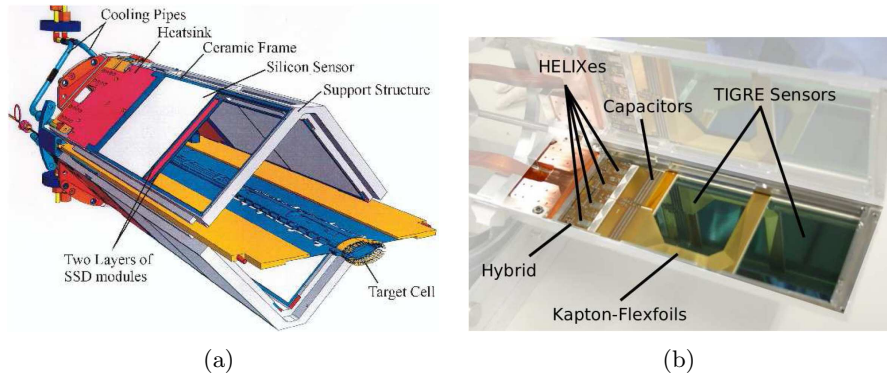
Figure 4.8:   *Setup of the Silicon Strip Detector. (a) The drawing illustrates the diamond shape surrounding the target cell in the HERA beam vacuum of the scattering chamber. (b) Photo shows one of the eight silicon modules.*

In order to extend the dynamic range [Hri+05] each strip has a charge division circuit with two outputs to the ADC (Analog to Digital Converter) as shown in figure 4.9. The high gain channels are used if the signals are not in the saturation range. In case of saturation in the high gain channel the low gain channel are used to measure the energy deposition. The dynamic range of the energy deposition are up to $7MeV$. The ADC consists of HELIX128 chips which was used for the LW (Lambda-Wheel) detector [Hee03].

4.4   Scintillating Fiber Tracker

One of the major components of the Recoil Detector is the SFT (Scintillating Fiber Tracker) [Hoe06]. The aim of this detector is to provide several space points to reconstruct the momentums of charged particles due to the deflection while passing the magnetic field. Furthermore the SFT contribute to the particle identification with momentum below $650MeV/c$. In combination with the PD (Photon Detector) particle identification can be provided for particles with higher momentum.

4.4.1   Detector

Particles passing material create electromagnetic radiation. In figure 4.10 this response for different materials and different particles are shown. The range indicated by red vertical lines can be used to identify passing protons
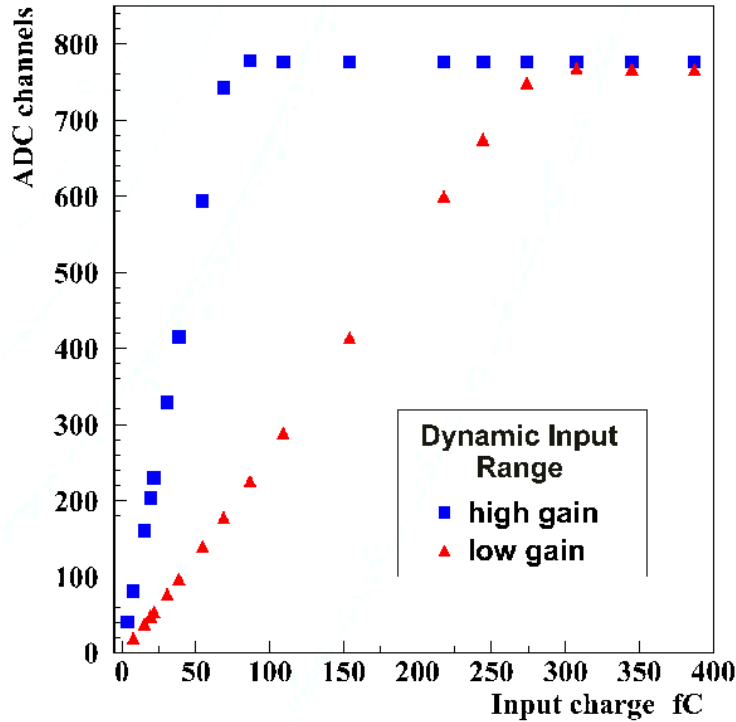
Figure 4.9: *The dynamic range of the silicon sensors are extended by factor 5 by charge division circuits as illustrated on the bottom. The ADC value of the high gain channel is used to reflect the accumulated input charge for the non-saturation regime. In case of saturation of the high gain channel the value of the low gain channel is used instead. [Hri+05]*

by the amount of deposited energy. Pions can be used as minimum ionizing particle as indicated by the green lines.

Figure 4.11 illustrate sample response of protons with different momentum and pions. Due to multiple scattering inside the fibers the response is smeared slightly to wider distributions.

The setup of the SFT consists of two barrels with two layers as indicated in figure 4.12(a) in order to support the track reconstruction. The fibers in the inner layer of the barrels are parallel to the beam axis while the outer layers of the barrels have an angle of 10° to the beam axis. In figure 4.12(b) the internal structure of a SFT module is illustrated. The overlap ensures a complete azimuthal coverage by the SFT detector. Due to this setup the SFT provides up to two additional space points. Together with the space points provided by the other subdetectors the particle tracks can be completely reconstructed.

The complete SFT detector is shown in figure 4.13. The active length
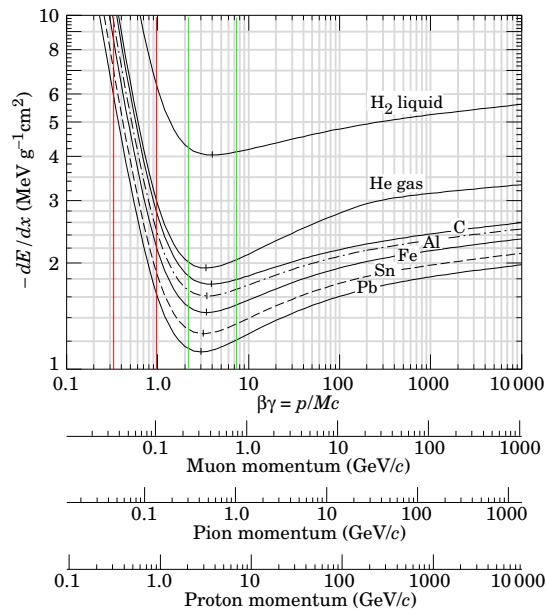
Figure 4.10: *Mean Energy loss versus momentum for different charged particles in different material. The response of scintillating fibers are similar to carbon. The vertical lines indicates the operational ranges for protons (red) and pions (green). [Eid+04]*
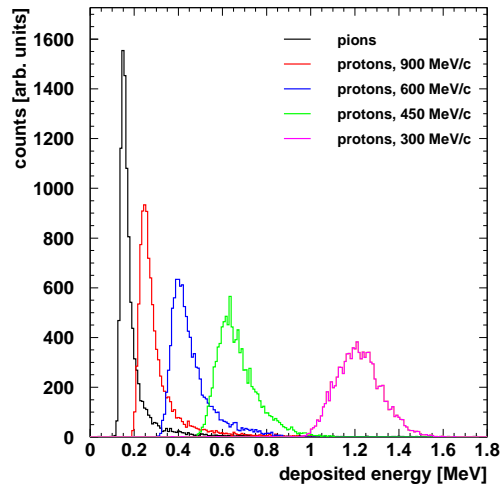
Figure 4.11: *Sample energy response distributions of the selected scintillating fibers for pions and protons for different momentums. [Hoe+07]*
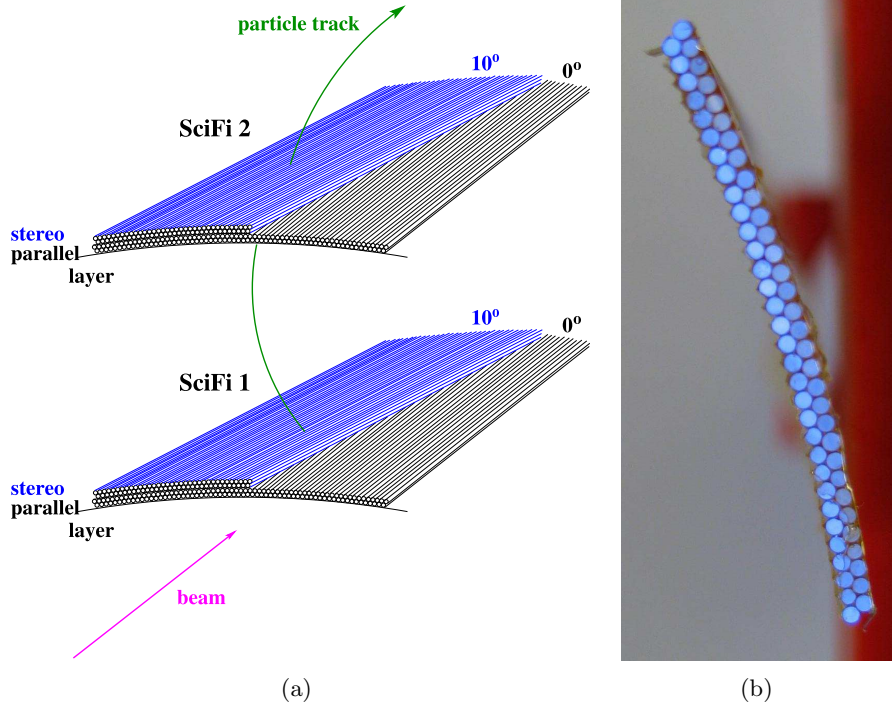
Figure 4.12: *Setup of the SFT (Scintillating Fiber Tracker). (a) Illustration of the concept for track reconstruction. (b) Photo of one stereo SFT module.*

of the fibers is around $280mm$ with an inner diameter of around $218mm$ while the outer diameter is around $375mm$. All fibers have $1mm$ diameter. The scintillating fibers for the detector are from Kuraray company, model SCSF-78M. The light guides between the detector and the photomultiplier tubes are built with clear Pol.Hi.Tec. fibers.

The inner barrel consists of 1318 parallel and 1320 stereo fibers while the outer barrel has 2198 parallel and 2180 stereo fibers. This yields to a azimuthal resolution of around 8mrad. As two fibers in the outer barrel are mapped to one MAPMT (Multi Anode Photomultiplier Tube) pixel almost 5k channels have to be readout. Particle identification for a momentum range between $250MeV/c$ and $650MeV/c$ is possible. Together with the PD (Photon Detector) particles with higher momentum can be identified. Even the SFT provides full azimuthal angular coverage the azimuthal angular acceptance for full tracking is limited by the SSD supporting frame to $\sim 70\%$. The polar angular acceptance is between $0.7rad$ and $1.35rad$.
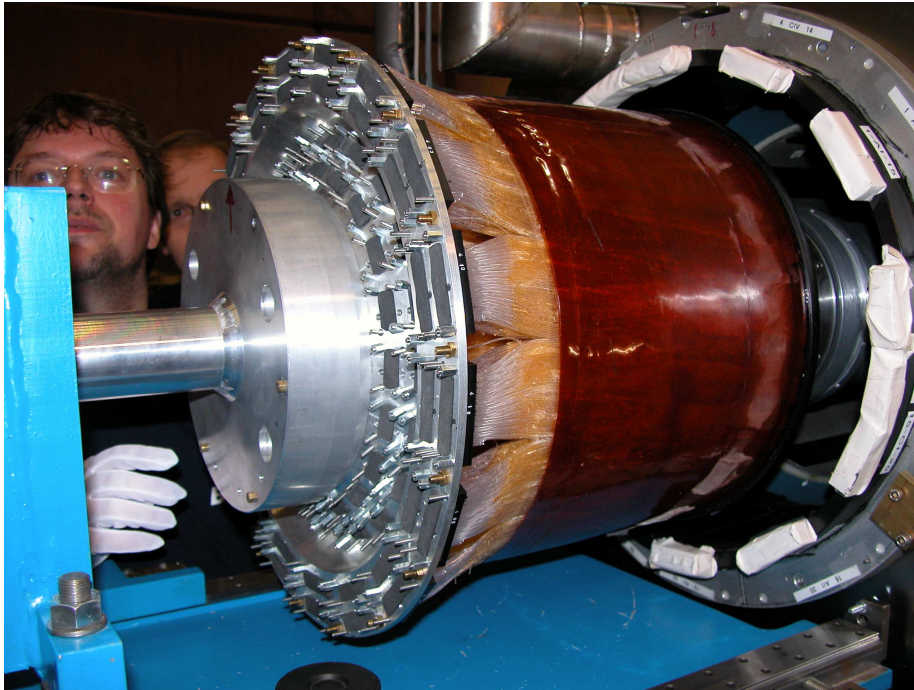
Figure 4.13: *Realization of the detector right before installation without. On the right the connector of the PD covered with withe tape is visible.*

4.4.2 Detection of light by MAPMT

The scintillating light is detected with H7546B MAPMT (Multi Anode Photomultiplier Tube) from Hamamatsu [Ham00]. These head-on type 8x8-MAPMT has the entry on the front side and the connector of the back side. It provides high speed response while the internal cross talk is very low despite of the high electronic density as illustrated in figure 4.14.

Each MAPMT pixel has 13 stages while an additional Dynode 12 output signal is available by accumulating all channels of the 12th stage. This Dynode 12 signal can be used for fast signal tracking.

The output of each channel of the 64ch-MAPMT works like a signal source. In order to maximize the available signal amplitude a resistive adaption to the digitizing units which works like a signal drain is required. In this case a CDC (Charge Division Circuits) illustrated in figure 4.15 consisting of a resistors-capacitors-circuit sitting on a PCB (Printed Circuit Board) is used.

In order to avoid malfunction by weak galvanic connection the MAPMT are soldered on to the CDC-PCB as shown in figure 4.16. The square soldering bed are surrounded by the resistance adaption.

(a) (b)
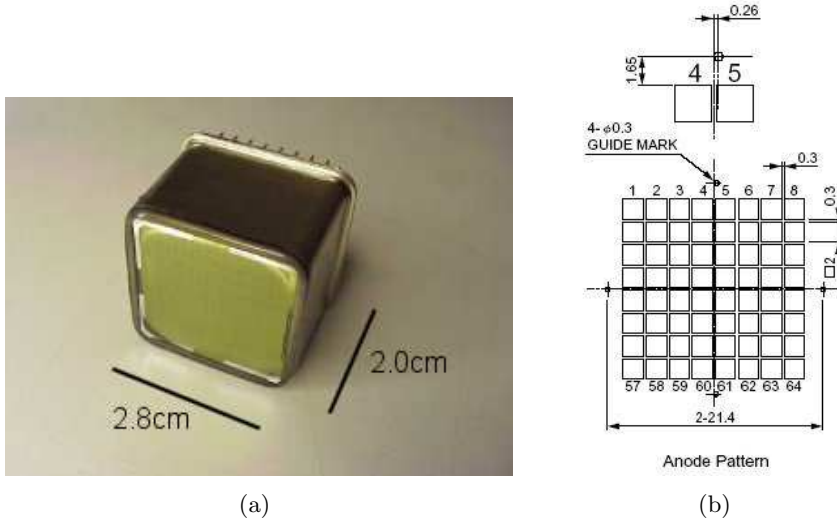
Figure 4.14: *MAPMT Hamamatsu H7546B [Ham00] for detection of scintillating light. (a) Photo of the core H5900-00-M64 MAPMT (Multi Anode Photomultiplier Tube) without housing and voltage divider. (b) The layout of the cathode plane illustrate the high density package of the 64ch-MAPMT.*
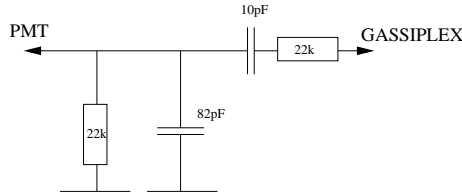

Figure 4.15: *Interface between MAPMT as signal source and the track and hold unit Gassiplex as signal drain. CDC (Charge Division Circuit) to adjust resistance of MAPMT and Gassiplex chips.*

4.4.3 Analog to Digital Converter

To improve the particle identification beside the topology of the track as well as the deposited energy inside the SFT have to be measured as simple hit informations generated by discriminators are not sufficient. Since 5120 MAPMT channels have to be readout and as the amount of space in the experimental area are limited standard hardware did not fit the necessary requirements. Therefore the inhouse high density ADC readout of the HADES (High Acceptance Di-Electron Spectrometer) experiment was used as the cost per channel are very low as well. A very detailed documentation about this Analog to Digital Converter can be found in [Kas+99] and
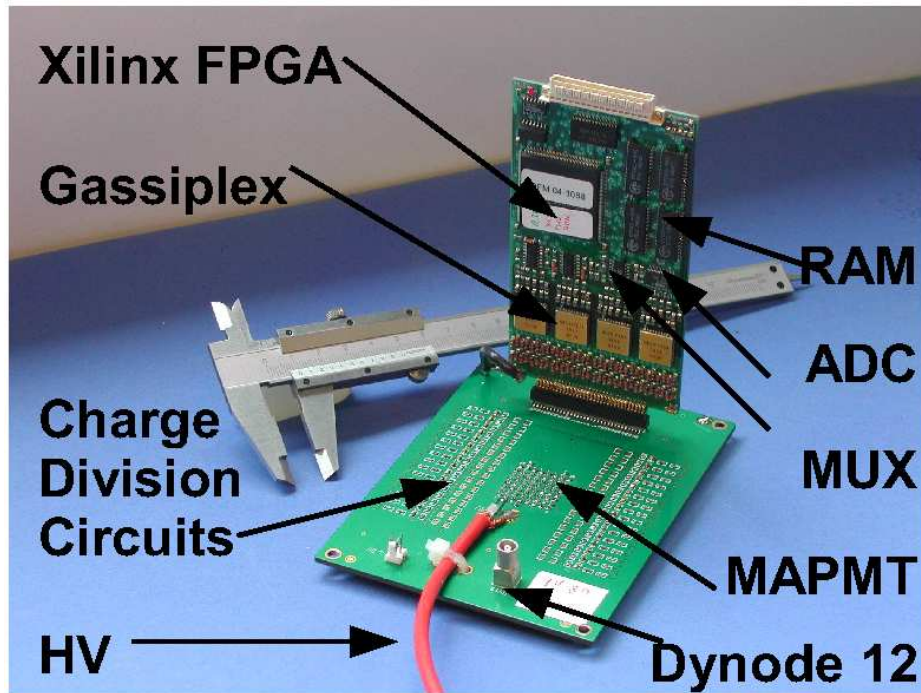
Figure 4.16: *Photo of the two PCB of the CDC and PFM. The CDC-PCB hold the soldered MAPMT and the charge division circuits while the PFM-PCB contains the electronics for the digitization and sparsification.*

[Boe00].

The Gassiplex chips [San+94], [San+01] which was developed at CERN were used as track and hold unit to store the analog signal for queued digitization with one fast and precise ADC. In figure 4.17 the internal setup of this chips is shown. All 16 input channels have charge sensitive amplifiers on the first stage. The second stage consist of selectable filter in order to change the polarity of the analog signal if desired. The third stage is a shaper with a integration time of around $600ns$. The output of the shaper are stored with a track and hold unit. On the last stage a 16:1 multiplexer is used to make the analog signal accessible to the Gassiplex output.

Figure 4.18 illustrate the setup of the ADC-PCB named PFM (Preprocessing Frontend Module). The tracked analog signal of the four Gassiplex chips are routed over a 4:1 videomultiplxer El441C [Ela96] from Elantec Inc. to the ADC chip ADS820 [AD08a] from Analog Devices, Inc. (former Burr-Brown Corp.). A threshold sparsification unit is implemented in order suppress small signals. All the components are controlled by a FPGA (Field Programmable Gate Array) XC4005E [Xil] from Xilinx which can be programmed in order to reflect improvements in the readout handling. The

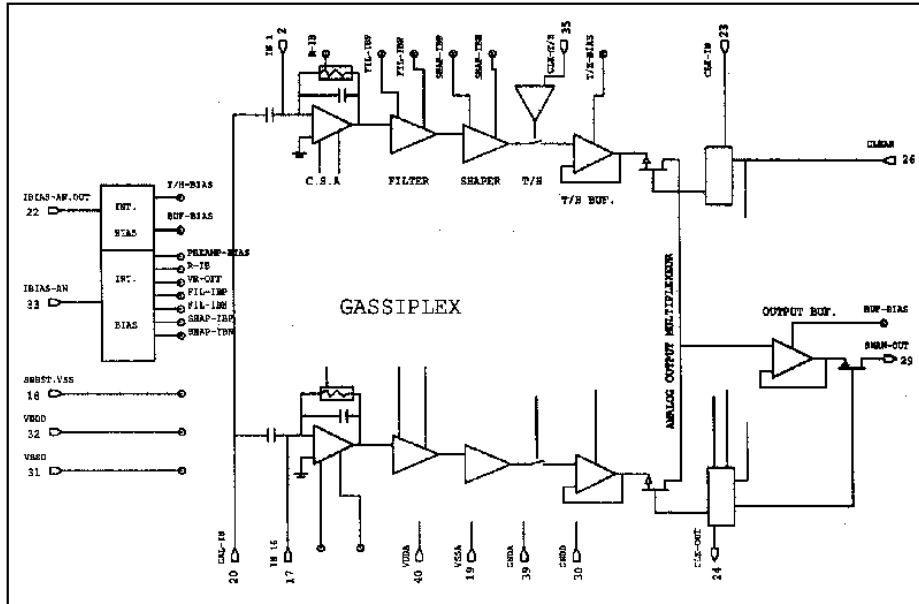CDC-PCB with the MAPMT and the PFM-PCB for the digitization are shown in figure 4.16.

Figure 4.17: *Sketch of the Gassiplex chips [San+94], [San+01] which was developed at CERN. This chips works as a track and hold unit and has an internal multiplexing to map 16 input channels on one output channel.*

In figure 4.19 a sample MAPMT signal is shown which has a narrow pulse width of few ns. As mentioned before the Gassiplex has a integration time of around $600ns$. The figure 4.20 indicate that the timing of the digitizer trigger is not very crucial.

The HERA bunch cycle time is $96ns$. This can lead to misinterpretation of the resulting analog signal as several independent interactions can be accumulated. In order to decide if the signal corresponds to the right bunch a secondary readout chain was implemented [Har04].

The selected MAPMT provides with the Dynode 12 output a fast tracking signal. By shaping the signal with a combination of amplifier and discriminator a multi-hit multi-event fast TDC (Time to Digital Converter) provide hit timing information with $100ps$ resolution for cross check of the corresponding ADC value.

4.4.4   ADC Readout

The readout of the SFT based on the hardware of the RICH (Ring Imaging Čherenkov) readout of the HADES Experiment. Detailed documentation in [Kas+99] and [Boe00] are available to describe the hardware used by the
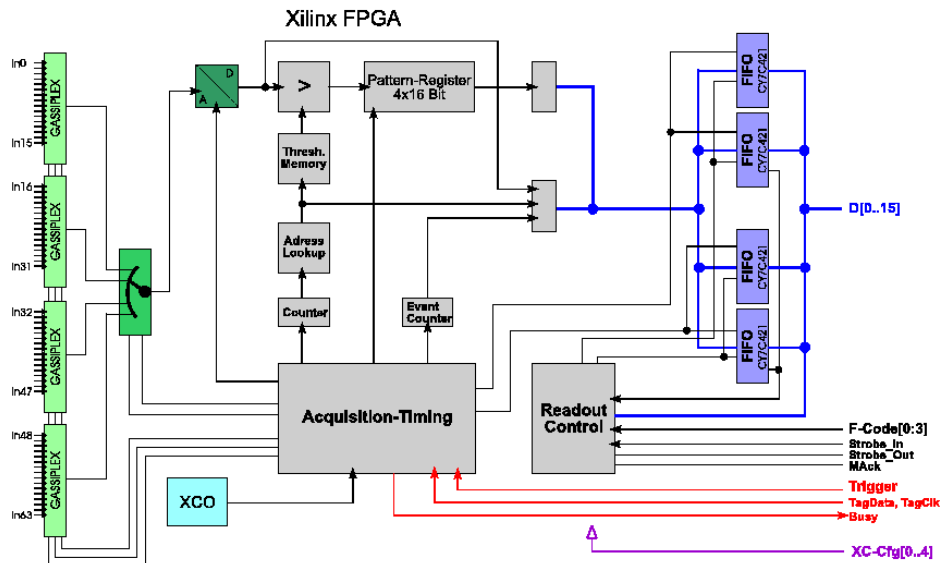
Figure 4.18:   *Scheme of the functionality of the PFM-PCB [Kas+99], [Boe00]. The green part is responsible for the digitization. Each of the 64 analog signal from the MAPMT are routed through one of four 16Ch-Gassiplex chips to a 4ch to 1ch video multiplexer. Therefore only one very fast and precise ADC-chips is needed. The gray part contains the Xilinx FPGA as local controller and the memory for the thresholds of the sparsification unit and after sparsification for the remaining data. The blue part represents the buffering of the interfacing signal*

ADC readout. Therefore the hardware details will be skipped. An general schematic of the readout is illustrated in figure 4.21.

The hardware is based on versatile FPGA chips which consists of a grid of logic gates and can be reprogramed for desired functionality. This provides flexible adjustment of the signal flow and of the control flow of the DAQ (Data Acquisition). The external trigger is delivered to the Gassiplex chips of the PFM (Preprocessing Frontend Module). After digitizing of the analog signals the optional sparsification is performed. The readout of the available data can be done either by a direct access to the RC (Readout Controller) via a standard PC or via a DSP (Digital Signal Processor) located on the VME crate controller. As the readout is based on the DTU (Detector Trigger Unit) which controls the readout controller several debugging informations about the internal state were provided to detect malfunction in the readout and to recover within the dead time of the readout.
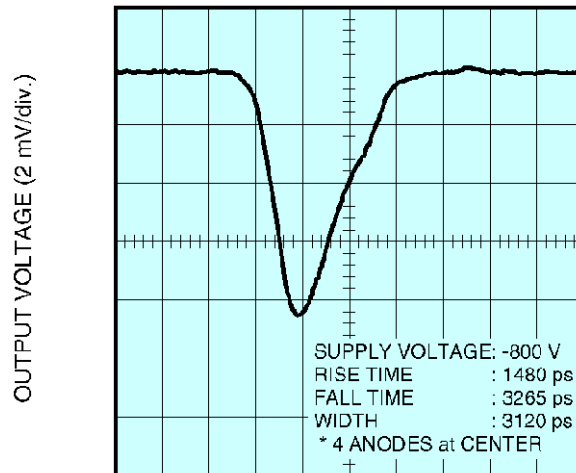
Figure 4.19: *Sample MAPMT [Ham00] signal as input to the track and hold unit.*

Recoil standalone readout

For test runs and maintenance of the Recoil Detector the SFT was readout directly by a PC based DAQ [SFT+06]. For this a simple console based program in the high level C programming language was written. The major informations like counters and event tagging was integrated into the data stream. This gives the opportunity to cross check the data integrity and in case of desynchronization between the ADC and TDC to resynchronize them again.

4.5 Photon Detector

The outermost and remaining subdetector of the RD is the PD (Photon Detector). It serves as an electromagnetic calorimeter in order to detect photons in the real experiment coming from decaying neutral particles and to provide a trigger generated by cosmic rays on the cosmic ray test run before the installation of the fully assemble RD into the HERMES experiment for studies on calibration, alignment and for stress tests of the implemented readout of the RD. A short overview about the PD will be given below while a detailed documentation can be found in [Haa07].

As neither the SSD nor the SFT are sensitive for neutral particles the key feature of the PD is to detect photons from decayed particles. A possible source of photons is intermediate Δ^+ resonance also called associated BH-process $ep \to e\Delta^+$ which decays in the chain $\Delta^+ \to p\pi^0 \to p\gamma\gamma$. When both produced photons are detected the decaying π^0 can be reconstructed. By
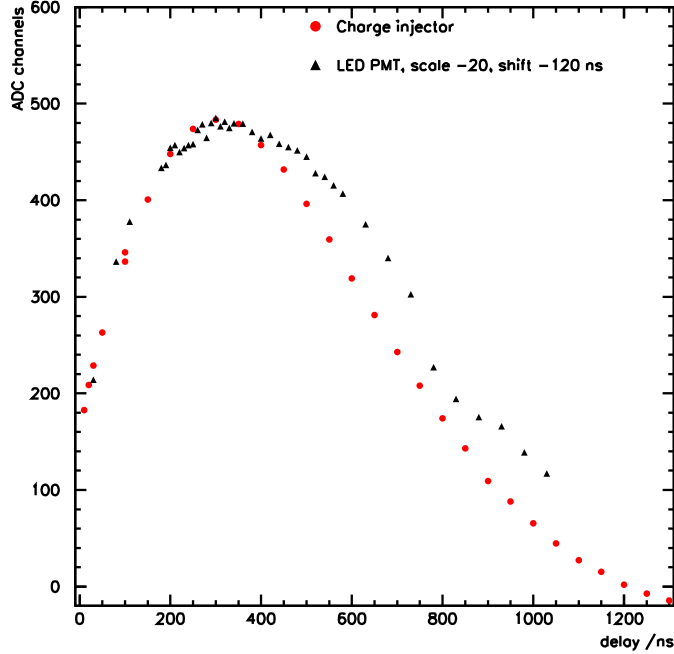
Figure 4.20: *Response of the Gassiplex chips for different delay of the underlying trigger system. [Har04]*

detecting these photons the Δ^+ background suppression for hard exclusive processes like DVCS can be improved. Additional feature of the PD is the contribution to the particle identification of protons and pions for momenta above $600 MeV/c$.

The setup of the PD consist of concentric barrels with three alternating layers of tungsten radiator as converter material and scintillating plastic strips for detecting the electromagnetic showers. The complete barrel has an inner diameter of $\sim 190mm$, an outer diameter of $\sim 250mm$ and a active length of $\sim 288mm$. The figure 4.22 shows the PD during the construction phase. The figure 4.23 illustrates the construction of the PD in a front and in a side view cut as a schematic while figure 4.24 displays the stripes.

The first layer of tungsten in front of the first scintillating layer has a thickness of $6mm$ while the other two layers of tungsten are $3mm$ thick. One radiation length corresponds to $3.5mm$ tungsten. These scintillating layers are build by strips to cover the 2π azimuthal angle and the polar angle between $0.78rad$ and $1.9rad$. The orientation of the strips in the layers with respect to the beam axis are from inner layer to outer layer 0°,
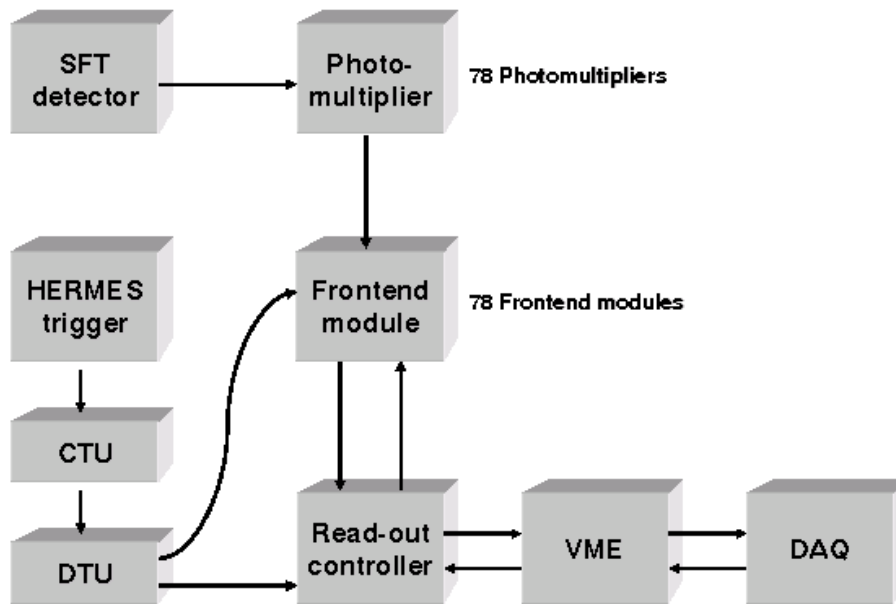
Figure 4.21: *Schematic illustration of the SFT readout system. The arriving trigger from the HERMES DAQ is distributed to the Frontend modules to start digitization. Afterwards the available data are read out over the VME based readout controller with conventional PC or with DSP.*

$+45^o$ and -45°. All together 60 strips with a with of $20mm$ and a thickness of $1mm$ forming the innermost parallel layer while each of the two stereo layers consist on 44 strips with comparable dimensions. On both sides of each strip a wavelength shifting fiber is embedded. The fibers shifting the generated scintillation light to the best acceptable for PMT wavelength and transporting the shifted light till PMT cathode.

These MAPMT H7546B from Hamamatsu are the same as used for the SFT. A shielding is used to attenuate the rest of the magnetic field from outside of the recoil magnet. The electronic signals from the MAPMT are transfered through a transmitter receiver chain from the experimental platform to the electronic trailer over more than $30m$ distance and through additional $80m$ shielded flat ribbon cables to several CDC (Charge to Digital Converters) V792 from CAEN. These CDC are readout by commercial VME based equipments and standard computer hardware.

4.6   Superconducting Magnet

In order to reconstruct the momentum by the deflection of the detected charged particles a superconducting magnet with a field strength of 1T at
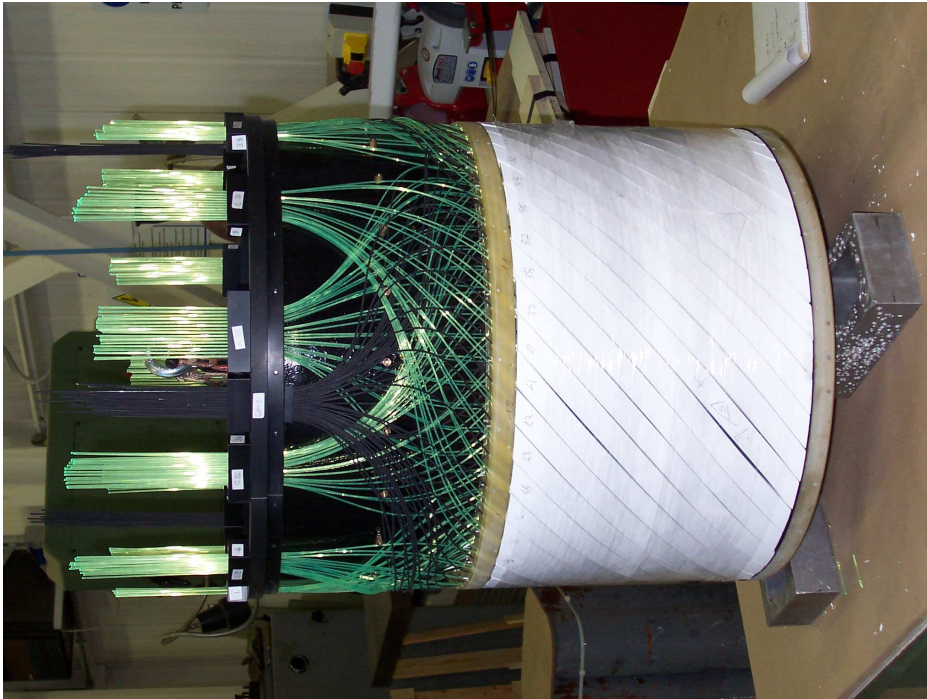
Figure 4.22:   *Internal setup of the Photon Detector during production and before mounting the light tide coverage. The green fibers of the wave-length shifters illustrate the three different orientation (0º,±45º) of the strip segments which are covered with white tape. The black fibers are used by the gain monitoring system. The picture is rotated by 90⁰ counterclockwise to present the final orientation.*

the beam axis is surrounding the RD. The magnet is furthermore protecting the RD, especially the SSD from background electron scattering processes like Møller or Bhabha scattering by bending their tracks to the forward direction.

The magnet constructed by the Efremov Institute in St. Petersburg [Sta06] is shown in figure 4.25 as schematic.

The shape of two superconducting Helmholtz coils cooled by a liquid helium bath is designed to ensure a homogeneous magnetic field parallel to the beam axis. The variation of the magnetic field inside the coils is less than 20%. The coils of the magnet are supported by a surrounding iron yoke which additionally attenuates the field outside of the RD to remaining $2mT$ in a perpendicular distance of $2m$ from the center.

For an incident particle passing the SSD and the SFT several space points are available to reconstruct the momentum by the trajectory. If the particle stuck in the inner part of the RD the momentum can be reconstructed by
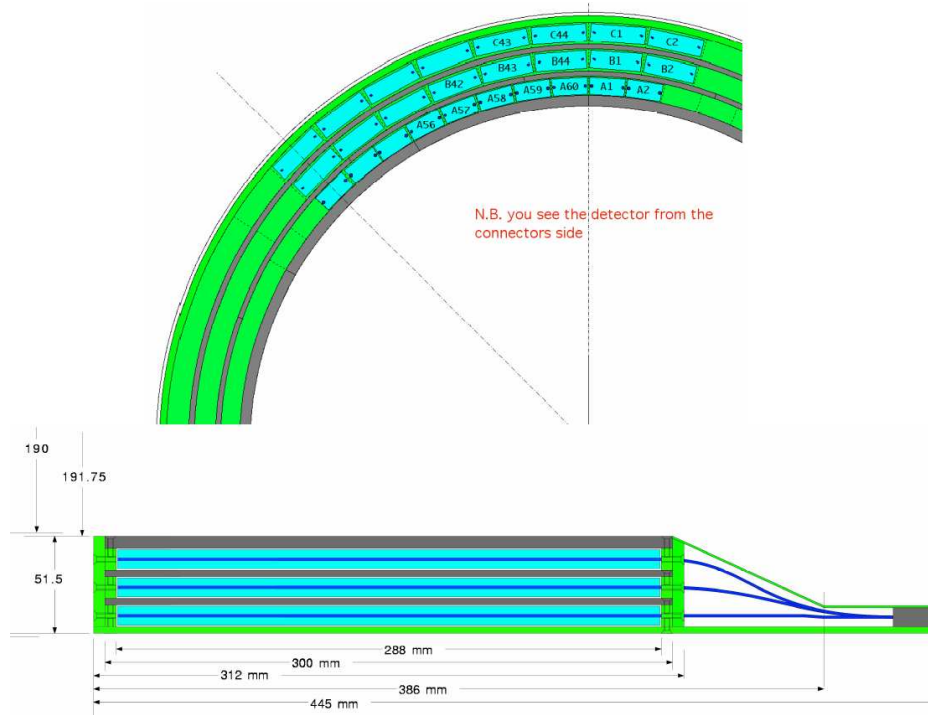
Figure 4.23: *The concept of the Photon Detector. The setup of the layers partially projected on the downstreamed x-y-plane in the upper schematic. The lower part is the projection on the x-z-plane. As indicated by the sequence of the gray tungsten preshower layer and the blue strip layer the upside part is in the inner part of the detector.*
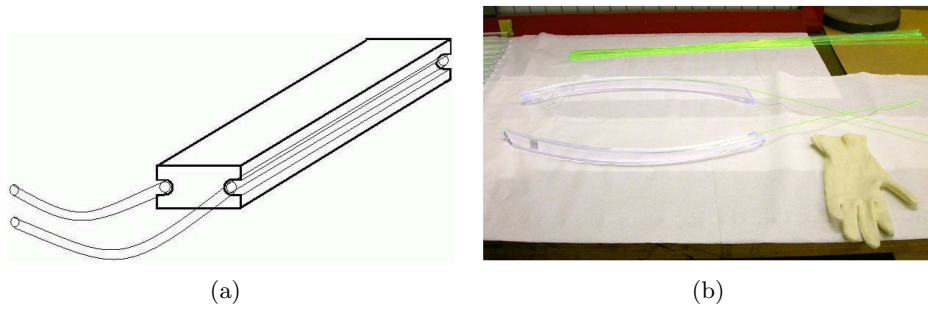

(a)   (b)

Figure 4.24: *Shape of the scintillating strips (a) The concept of the segmented strips and the wave-length shifters are shown. (b) Picture of the transparent stripe of the stereo layer and the green wave-length shifters in the background.*
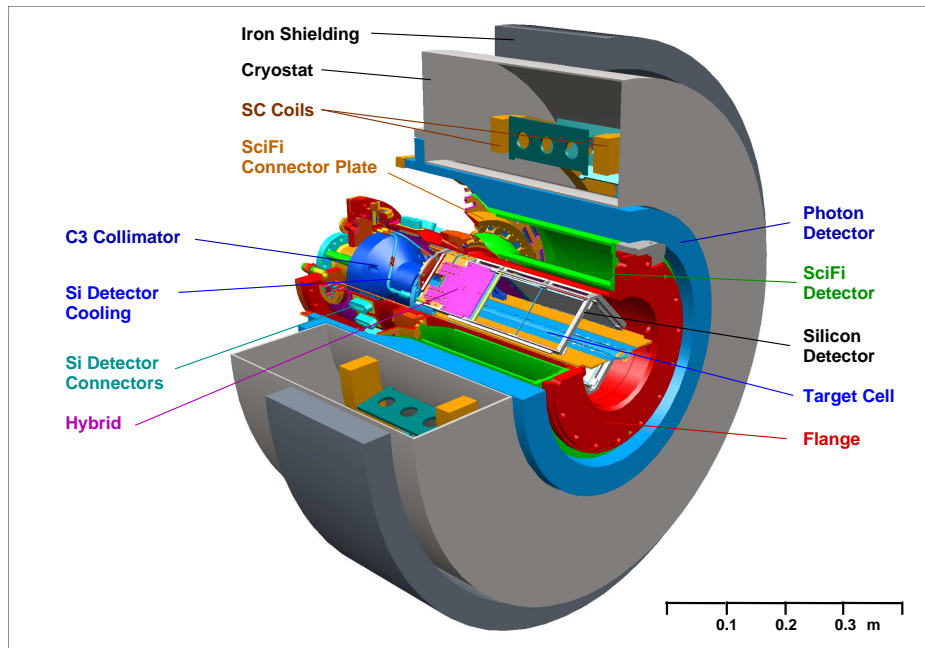
Figure 4.25: *Setup of the superconducting magnet together with the other parts of the Recoil Detector.*

the amount of deposited energy.

4.7 Installation of the Recoil Detector

The Installation of the Recoil Detector into the HERMES experiment started in November 2005. At the beginning the equipment for the polarized target was removed to prepare the area in front of the HERMES forward spectrometer. First the basement for the Recoil Detector and the liquid helium pipe for the superconducting magnet have been installed. Afterwards all the electronics and cabling were connected. The prepared Recoil Detector ready for data taking is shown in figure 4.26 right before the interlock of the restricted area was set. Due to the well prepared schedule and very focused activities the installation was very smooth and very successful.

Afterwards the apparatus of HERA were switched on in order to start to study the machines with low current at the beginning as many of beam magnet coils have been replaced. The investigations and preparations of the storage ring succeeded very fast so the normal running conditions were established soon with $\sim 110mA$ protons at $920GeV$ and $\sim 43mA$ electrons at $27.6GeV$.
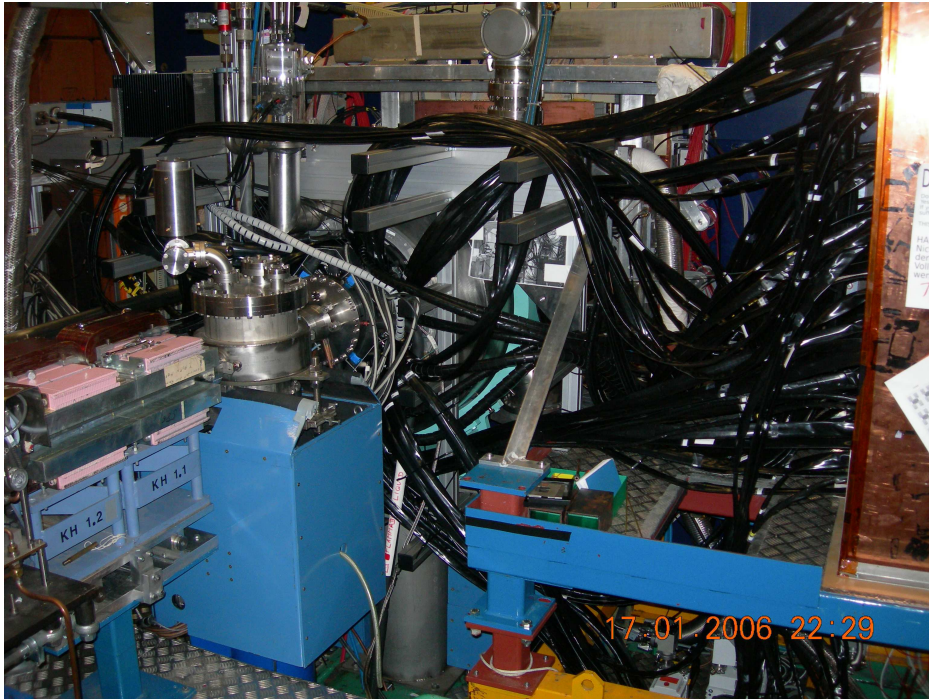
Figure 4.26: *The picture shows the installed Recoil Detector right before the interlock of the restricted area was set.*

HERMES based readout

The readout system of the Recoil Detector by the HERMES DAQ consists of several steps. The first step is the readout of the digitizers to the internal shared memory by the DSP (Digital Signal Processor) of the VME crate controller. The control program for the DSP was written in assembler. The next step is to collect data from all the VME crates by the DSP of the master VME crate. A standard PC based readout transfers in the next step the data inside the shared memory of the master VME crate controller to the local memory and merges additional status informations to the data. In the final step all event based collected data are written to the tape.

In case of the SFT additional debugging informations for each event about the internal state of the DTU and the RC are saved as well. Therefore additional cross check capability for the data quality in the offline analysis chain can be provided. Also slowcontrol data are important for later data analysis and detector recalibration.

Chapter 5

Performance

This chapter will focus on the SFT (Scintillating Fiber Tracker) which was the main contribution of the Giessen group to the RD (Recoil Detector). The other detectors are covered in detail in [Pic08] and in [Vil08] for the SSD (Silicon Strip Detector) and in [Haa07] for the PD (Photon Detector). First a short introduction about the bench tests like proof of concept, alignment run and the final cosmic ray test run will be given. Preliminary performance of the installed RD with the SFT in correlation with the HERMES forward spectrometer and first calculations of azimuthal asymmetries of hard exclusive reaction will be presented.

5.1 Proof of concept

As shown before the SFT is one of the major components for particle identification and track reconstruction. A series of simulations and measurements was done to proof the concept of the SFT. The required setup of the SFT proposed in [Kai+02] were designed by studying Monte Carlo simulations on pions and protons [Som03]. The measurements at GSI in Darmstadt/Germany were done in 2003 to proof the chosen realization of the SFT and to settle down final configuration parameters [Hoe+05], [Hoe+07]. The used hardware for the readout are documented in [Rub06].

5.1.1 Test beam environment

The SIS (Schwerionensynchrotron) at GSI (Gesellschaft für Schwerionenforschung) provides secondary beams over a wide momentum range generated by a primary proton or ion beam delivered by the SIS colliding with a production target [Dia+02]. For each of the four scheduled test beam experiments the secondary beam consisting of pions and protons was generated by a primary ^{12}C beam penetrating a $120mm$ thick B$_4$C target. The contamination by other particles was negligible or was excluded by parti-

from SIS

production
target

cave H

cave A

cave C

cave B

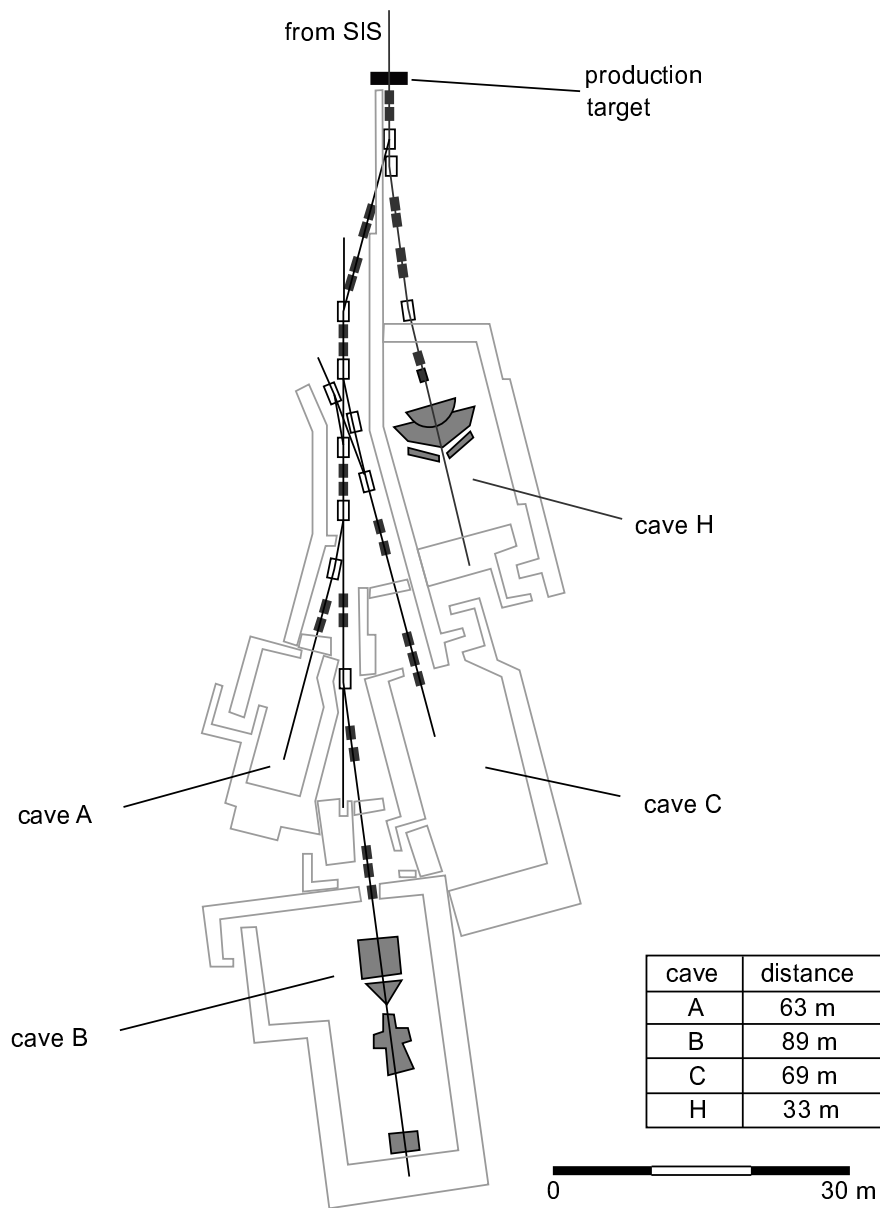| cave	distance
A	63 m
B	89 m
C	69 m
H	33 m

0   30 m

Figure 5.1: *This is a schematic of the first floor of the target hall at GSI [Dia+02]. The primary beam of protons or ions entering at the top penetrate the production target to generate secondary beams which are led by beam lines partially covered by high magnetic fields for particle selection in a wide momentum range to several experimental locations. The test experiment for the RD especially for the SFT is located in cave A.*

cle identification. The selected central momentums of the secondary beam with a smearing of below 10% was $300MeV/c$, $450MeV/c$, $600MeV/c$ and $900MeV/c$ to cover the design requirement. The setup was located in Cave A in the target hall as shown in figure 5.1.

5.1.2 Detector prototype

The SFT test module [Hoe+07] was built like a section of the SFT with two units representing an inner and an outer barrel each with a parallel and a stereo module as visualized in figure 5.2. The geometry was similar to the final SFT configuration. Each SFT module was connected via a light guide to a MAPMT.

Figure 5.2: *The test module used for the last test beam run in November 2003 [Hoe+07].*

5.1.3 Test beam setup

The test beam setup [Hoe+07] shown in fig 5.3 consists of the three sub detector of the Recoil Detector, four plastic scintillators and a MWPC (Multi Wire Proportional Chamber). Two plastic scintillators S_1 and S_2 are used to provide a primary trigger for the digitizing and readout. By combining this primary trigger with a third plastic scintillator S_0 time of flight information was available to provide particle identification. The fourth plastic scintillator S_3 was needed to study the efficiencies of the detectors. To monitor the beam position a MWPC was available as a reference system to study the resolution of the prototypes. The trigger logic was based on standard VME module while the readout was done with a standard PC. The electronics of the SFT readout [Hoe+05] as shown in figure 5.4(a) was tested as well.

5.1.4 Test beam results

Several test beam runs were carried out to investigate and to proof the concept of the detector. The major results will be presented.
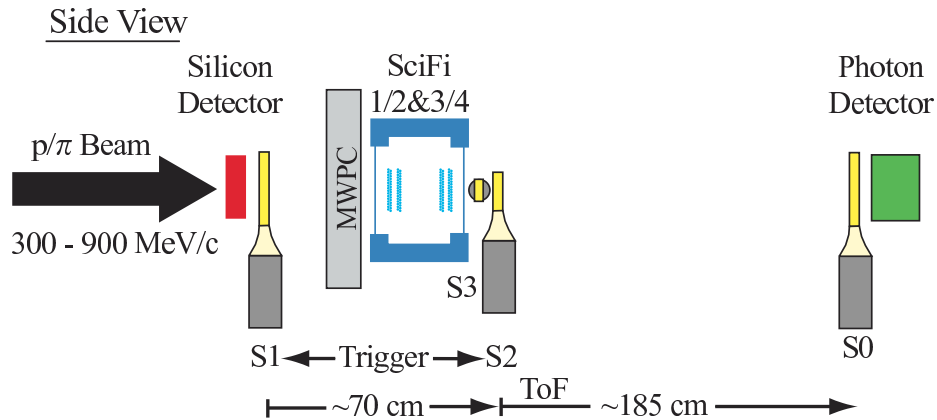
Figure 5.3: *The test beam setup [Hoe+07] used for the last test beam run in November 2003. The SSD (red), SFT (blue) and PD (green) are combined. S_1 and S_2 are used for trigger generation while S_3 is used for efficiency studies. S_0 is used for PID by time of flight separation. MWPC are used as a spatial reference of the combined $\pi - p$ beam in the momentum range between $300 MeV/c$ to $900 MeV/c$ which is entering from the left.*

ADC spectra

Typical raw ADC spectra [Hoe+07] is shown in figure 5.4(b). The pedestals stays at the raw ADC value around 925, while the larger signal are represented by smaller raw ADC values due to hardware implementation.

Particle identification

For particle identification [Hoe+05] the deposited energy and the time of flight informations are combined. As shown in figure 5.5 the particle separation between pions and proton for momentums around $300 MeV/c$ is very clean while for $900 MeV/c$ the areas getting close and a small contamination of heavier particles can be recognized.

Energy response

The energy response [Hoe+05] of the leading fiber is shown in figure 5.6(a) for pions and protons with several mean momentums. The corresponding Monte Carlo simulations done with GEANT [GEA93] for comparison are visualized in figure 5.6(b) and in good agreement with the measurements.

Efficiency

If N_{Ref} is the number of events with a hit in the reference plastic scintillator and if N_{SFT} is the number of events seen by the reference and the SFT, the

(a)   (b)
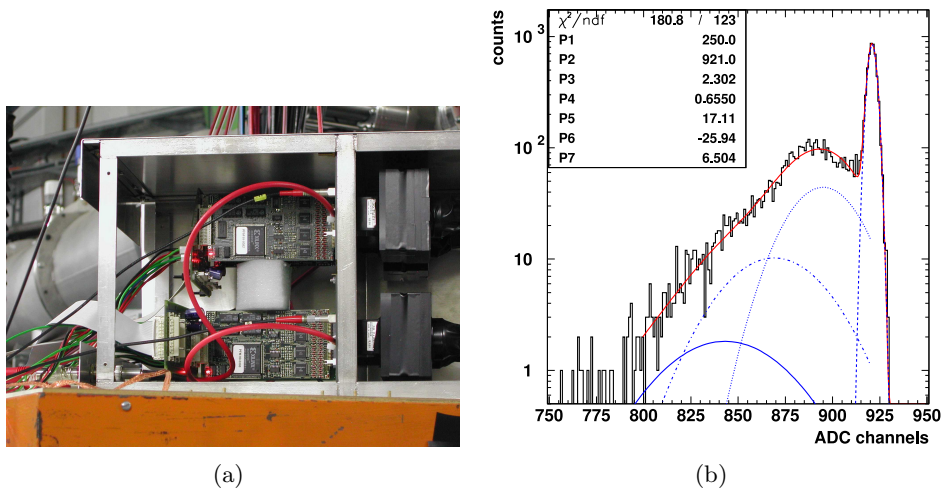
Figure 5.4:   (a) Picture of the electronics of the SFT readout. (b) Raw
ADC spectra for PMT response to a LED induced light. The contributions
of single, two and three photons are shown [Hoe+07]. N.B. due to hardware
implementation higher signals has lower raw adc values. Here the pedestal
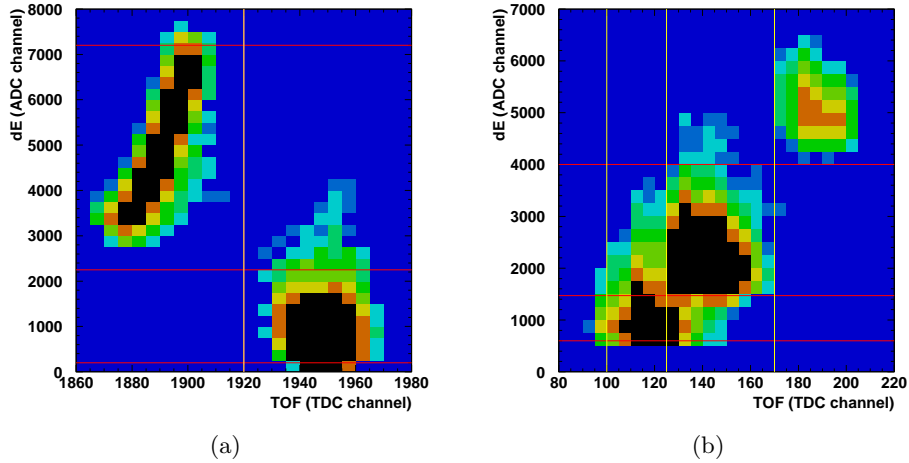stays at a raw adc value of 925.

(a)   (b)

Figure 5.5:   The particle identification is for $300MeV/c$ (a) well separated
while the response for $900MeV/c$ (b) are closer and some few heavier parti-
cles can be detected [Hoe+05].

efficiency is defined as the ratio $\epsilon = N_{SFT}/N_{Ref}$. In figure 5.7 the efficiency
ϵ for protons and pions is given for the investigated momentums and they

(a)   (b)
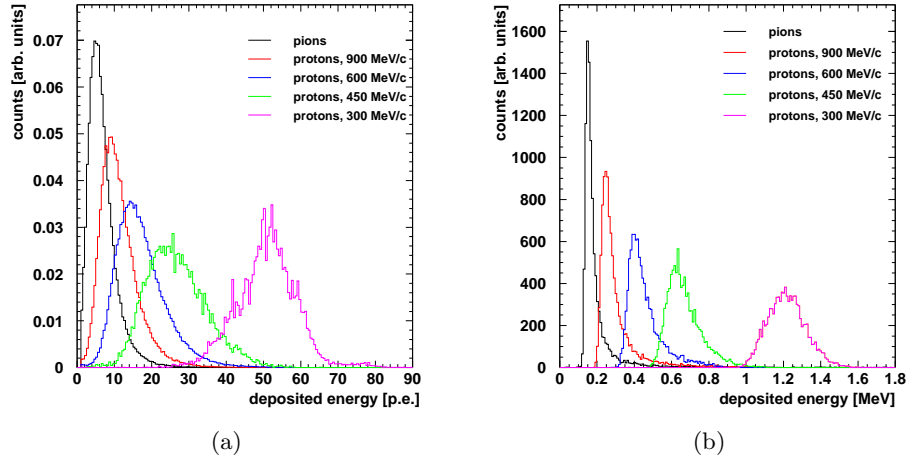
Figure 5.6:   *The leading fiber response for real data (a) and with GEANT Monte Carlo simulation (b) for different mean momentum of protons [Hoe+05].*

are determined to be above 98% for a module.

(a)   (b)
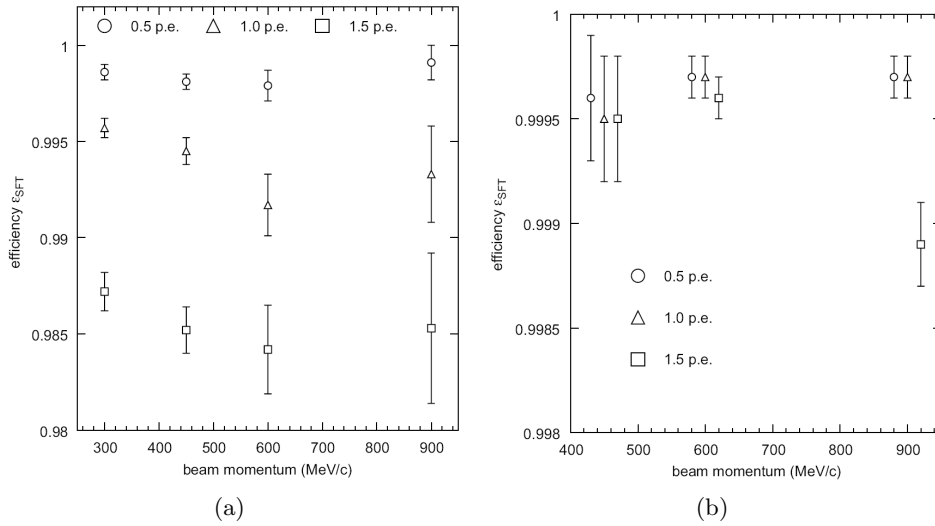
Figure 5.7:   *The efficiency for pions (a) and protons (b) versus the momentum is shown for different threshold level in units of photon electrons [Hoe+07]. The efficiency is independent of this signal cut off above 98%. The values for protons are shifted for better visibility to higher momentum.*

Readout implementation

Inside HERA at DESY four experiments have to cooperate. Therefore an access to the restricted area inside the interlock area is not trivial and the possibility for a repair or a hardware exchange is very limited. This forces to have an very robust readout as the readout electronic will stay inside the restricted area. Thus tests of the SFT readout had to be done. As shown in figure 5.8 some small problems occurred during the test beam runs [Hoe+05]. The error detection and error recovery have to be improved by storing the status informations into the data stream.

(a)   (b)
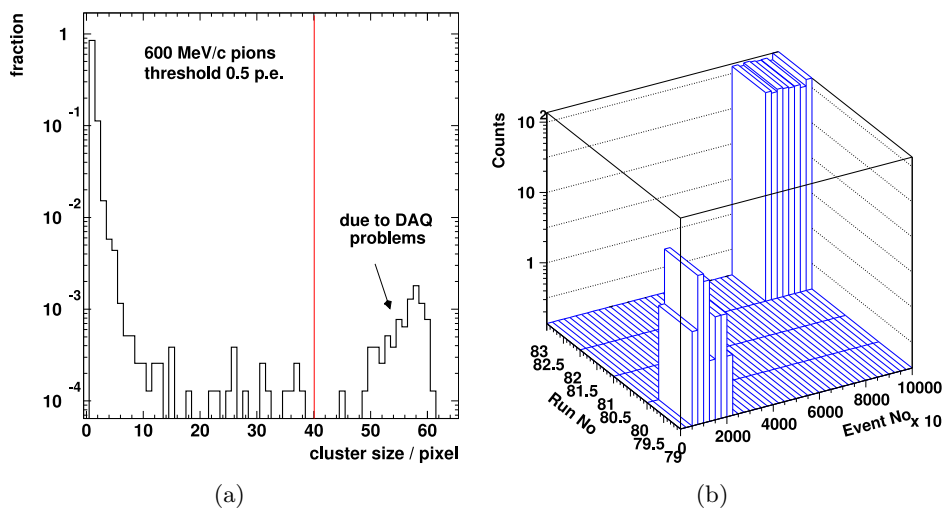
Figure 5.8: *Multiplicities of the clusters sizes in units of pixels [Hoe+05]. (a) A bunch of entries in the spectrum of the multiplicity of cluster sizes are due to problems in the readout of the SFT electronics. (b) These strange events are clearly located in some certain period of data taking and are excluded from further evaluations of the SFT.*

The other issue is the handling of the readout. During these tests the readout was running in the so called 'stop mode' [Rub06]. All the handshake signals for the readout had to be generated by the readout software running on a standard PC which limits the readout to an accepted trigger rate of around $100Hz$. In contrast to that in the HERMES experiment a trigger rate of several hundreds Hz during the high density runs or at the beginning of the fill is not unusual. Therefore the readout of the SFT had to be extended to the so called 'run mode'. In this readout mode most of the handshake signal are generated by the hardware itself and several informations about the internal state are available for error detection. It's implementation was one of the main topic of this work.

Conclusion for the testbeam run

The test beam experiment was very successful to improve the understanding of the components, to settle down final configuration parameter and to provide reference data and plots to tune further setups.

5.2   Alignment run

The intermediate test run for the SFT was the alignment run [Ste+05]. One aim was to implement the readout named 'run mode' and to test it under real conditions. The measurement of the SFT internal alignment for the later space point reconstruction of each fiber was the second goal of this alignment run.

5.2.1   Environment at test beam 22

The test beam areas at DESY II [Beh+07], [Gre+04] shown in figure 5.9 provide a e^- or e^+-beam up to 7GeV beam energy.

Accelerated electrons or positrons stored in DESY II generate a primary γ-ray by Bremsstrahlung on a $7\mu m$ carbon fiber. A metal plate of selectable material and thickness is used to convert the γ-ray by pair production into electrons and positrons. The leptons are bend due to a dipole magnet behind the converter. A set of collimators are used to form the extracted lepton beam before it enters the test beam areas. As the setup is very simple the desired beam energy and particle types can be selected by varying the converter properties and the magnetic field behind the converter.

5.2.2   Setup of the alignment run

The figure 5.10 illustrates the setup of the alignment run. The Zeus telescope consisting of three silicon strip detector. It was used as reference measurements of the properties of the lepton beam. The plastic scintillators S_1 and S_2 are used to generate a trigger signal for digitizing and readout. The active size of the reference telescope is $\sim 32x32mm^2$. As shown, the axis of the barrel of the SFT is turned to vertical direction and is mounted on a rotational frame sitting on a movable table. This gives the opportunity to rotate and shift the barrel accordingly to measure the whole detector step by step.

5.2.3   SFT readout in 'run mode'

For the data taking a readout of the Zeus reference telescope running with LabVIEW was available. A first readout of the SFT was implemented in this framework too. In order to minimize the necessary amount of time to scan
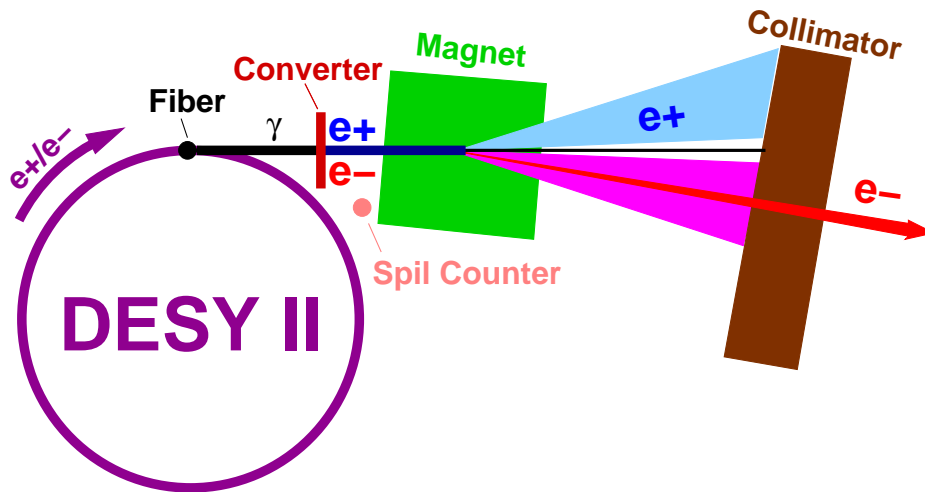
Figure 5.9:   *Accelerated electrons or positrons stored in DESY II generate primary γ-rays by Bremsstrahlung. These γ-rays are converted by pair production to electrons and positrons of a wide range of momentum. The dipole magnet behind the converter provide momentum separation of the secondary beam by deflection to a flat fan out. A set of collimators forms the final beam of selected momentum range and particle type. [Beh+07]*

the whole detector a standalone console program without the framework was developed with a gain in speed of more than one order of magnitude.

During the alignment run the SFT readout using the run mode of the readout controller was implemented and tested. Small hardware modifications had been made to terminate the signals properly and to provide the few essential handshake signals. Due to these simplifications the readout has been speed up to read unsparsified data with an accepted trigger rate of several hundred Hz. Technical details can be found in [SFT+06].

5.2.4   Alignment run results

Zeus telescope internal resolution

The hits in the three silicon detectors are used to reconstruct the projectile trajectory by combining these space points. The internal resolution of the reference system with the SFT in front is shown in figure 5.11. The resolution for the middle silicon sensor is around $20\mu m$ while the resolution without the disturbance of the SFT is around $19\mu m$. This gives a possibility to measure the path of the fibers very precisely.
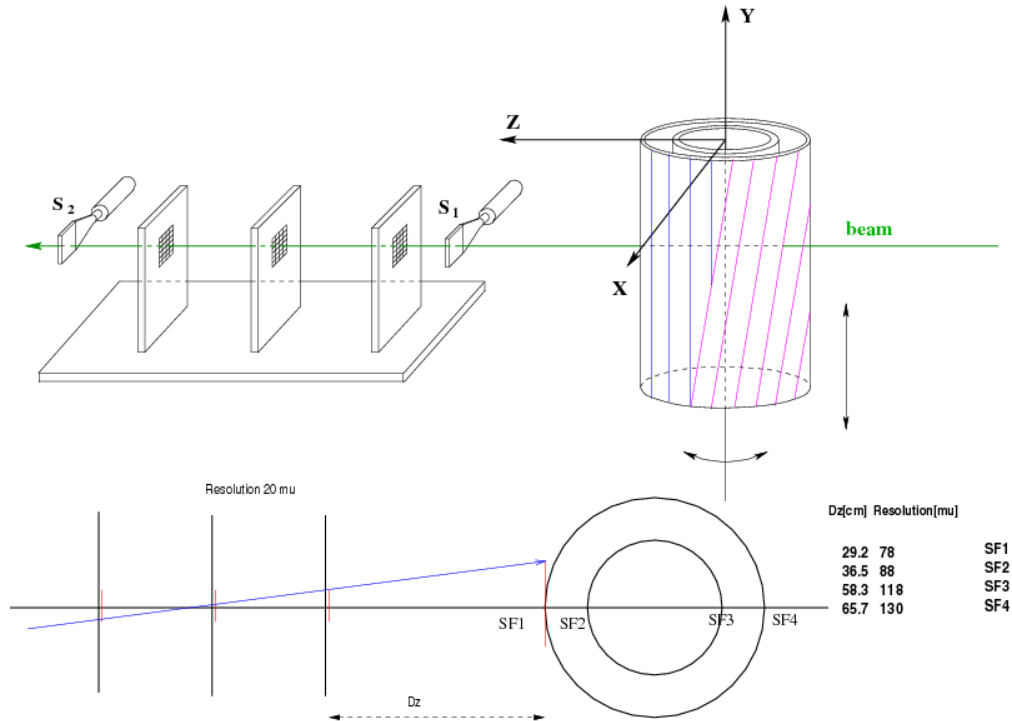
Figure 5.10:   *Setup of the alignment run [Ste+05] with the SFT detector in front of the Zeus telescope with the three silicon sensors and two plastic scintillators S_1 and S_2 for trigger generation. The beam enters the area from the right. The upper part is the side view while the lower part shows a top view with the achieved resolutions.*

Reconstruction of a single fiber

The reconstruction of the fibers are done in two steps. First single measurements are used to determine the short paths of the fibers in the clipping area. The reconstruction of a single fiber is shown in figure 5.12. The gathered positions are fitted with an gaussian curve visualized as a blue curve wherein the intrinsic fiber distribution and the distributions of the telescope are folded together. The contribution by the Zeus reference telescope itself is shown as a red curve. As the fiber diameter is $1mm$ the resolution of the reconstructed fibers around $400\mu m$ is very good.

Database of fiber positions

In the second step the results of each clip are combined by adjusting the overlap region to built a global 3D-picture of the SFT detector. For further
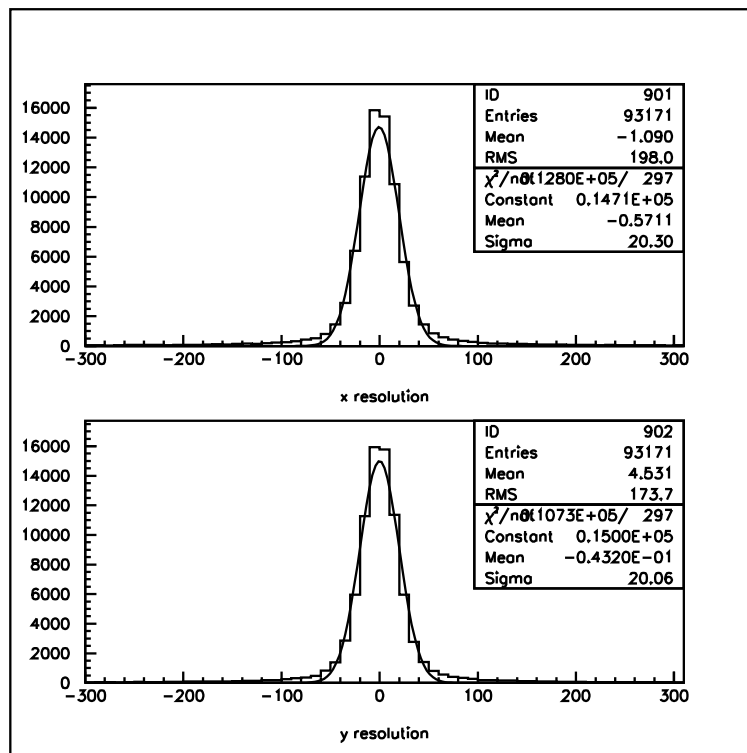
Figure 5.11: *The internal resolution of the Zeus telescope [Ste+05] is shown for the x direction (upper) and for the y-direction (lower). The sigma of each plot is* 20μm. *Without the disturbance of the SFT detector the sigma is* 19μm.

usage the paths of the fibers are described by polynominals up to fourth degree as shown in figure 5.13. These informations are afterwards used to align the SFT barrels to the other subdetectors of the Recoil Detector. Once the internal alignment is done elastic scattering events can be used to align the Recoil Detector to the HERMES forward spectrometer. The final fiber position resolution of 280μm is very close to the theoretical resolution of 220μm for a fiber with 1mm diameter [Yas07].

Final SFT readout

In order to include the SFT readout into the HERMES DAQ an DSP (Digital Signal Processor) have to be used. The used DSP is a ADSP 21061L SHARC-processor from Analog Devices [AD08b] which are based on a Harvard architecture where data and code are in separate memory space. The DSP has to be programmed in native assembler due to execution speed as a compiler based program has a high framework overhead. The alignment run
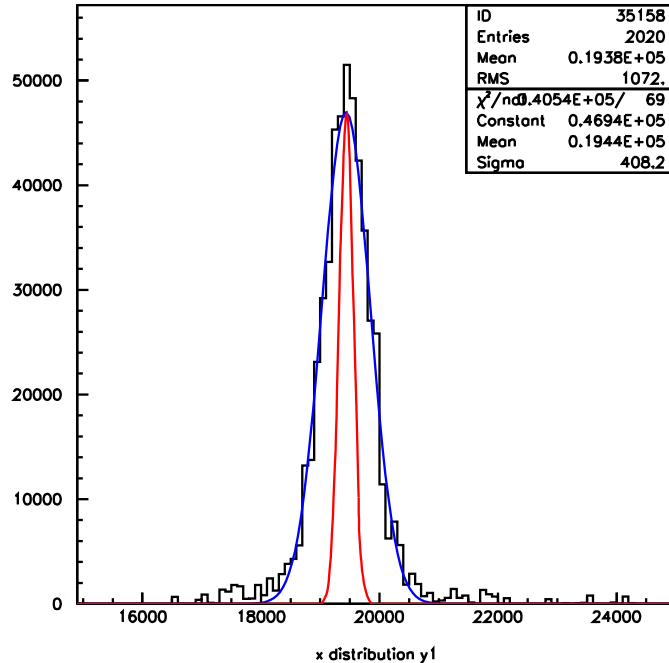
Figure 5.12: *Reconstruction of a single fiber position together with the fit as blue line and the contribution of the intrinsic resolution of the Zeus telescope as red is shown. [Ste+05]*

showed that the unsparsified readout speed of the SFT will be most likely not sufficient in all cases for the final implementation which will use twice the number of channels to be read out. In order to be on the safe side in any case concerning available data rate and to simplify the readout of the SFT it was decided to implement the final SFT readout with the support of the DTU (Detector Trigger Unit).

Conclusion for the alignment run

This second bench test was very successful. The intermediate readout was implemented, tested and running very stable. In total more than 600 runs with each 100k events had been taken. The paths of the fibers was measured very precisely.
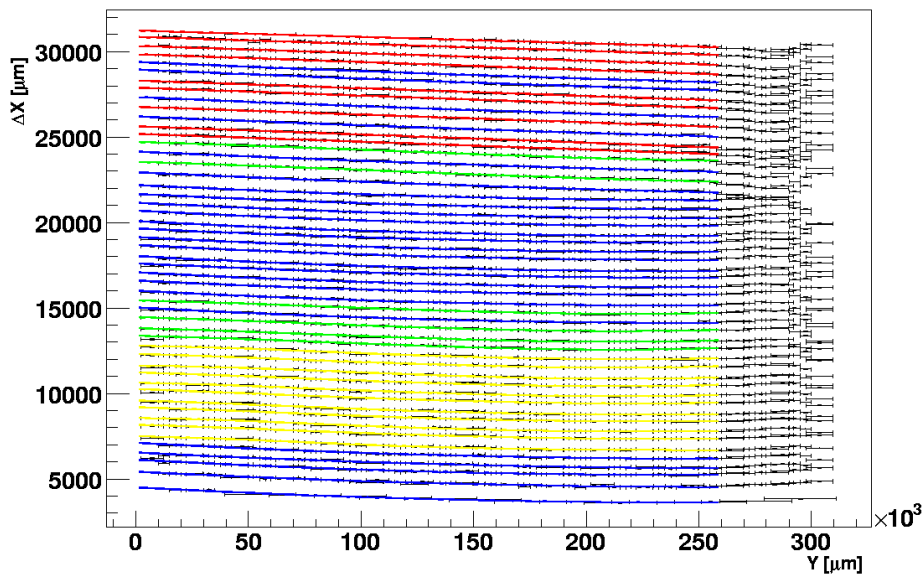
Figure 5.13:   *The trajectory of the reconstructed fibers are described by polynominals up to fourth degree which are visualized by different colors. The boundaries of the SFT modules are around y=22500 as visible on the right side. [Ste+05]*

5.3   Cosmic ray test run

In 2005 the cosmic ray test run as shown in figure 5.14 was performed to prepare the installation of the RD into the Hermes Detector environment.

For this an area in the east hall close to the HERMES detector but outside of the interlock area was established to perform extended stress tests. The RD was put as close as possible to the final setup. The superconducting magnet was installed and tested under the experimental conditions. The readout of the RD was implemented and prepared to be merged into the HERMES DAQ together with the slowcontrol chain, which collects secondary informations of the detectors and the condition of HERA running. The setup was ready for data taking in March 2005.

5.3.1   Readout of the SFT

During the previous test runs the readout for the SFT was improved step by step [SFT+06]. The change from stop mode to run mode increased the accepted trigger rate by one order of magnitude. A further improvement was possible with the use of the DTU which controls the signal flow over the backplane. This VME based device generates the handshake signals by a SM (State Machine) realized with a FPGA. A SM is a model of a machine
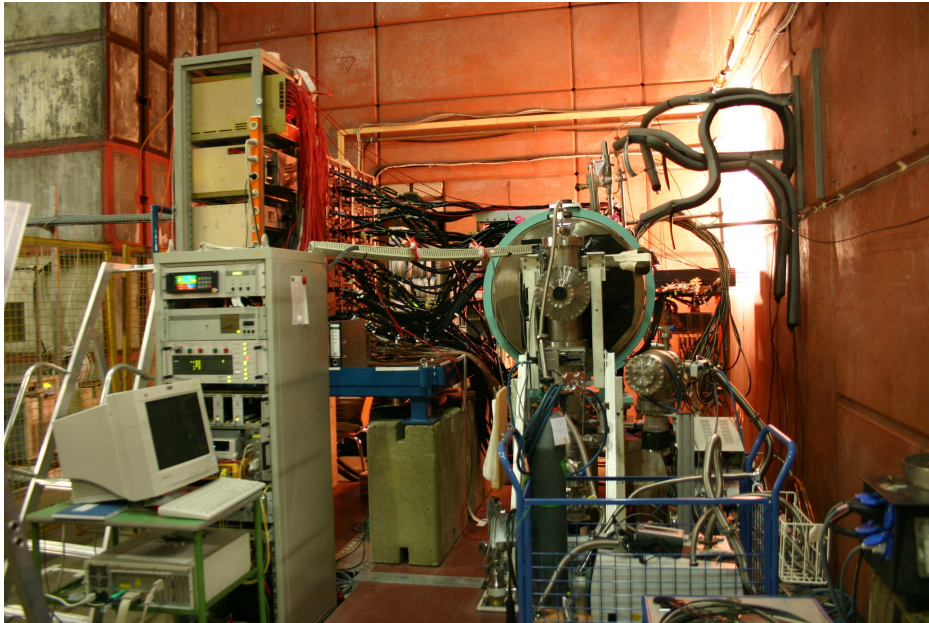
Figure 5.14:   *The complete installation of the cosmic ray test run setup consists of the Recoil Detector with the superconducting magnet in the center, the pump stand (front right), the magnet control system (front left), the platform with the rack for the readout electronic and the PMT wall of the SFT (left to RD) and the barely visible readout racks of the other RD components in the background.*

where state transitions and actions are performed by a set of rules stored in the internal memory. Additional debugging facilities were implemented into the SM as well. They provide informations about internal counters and tagging of events in order to detect desynchronisation during readout and to be able to resynchronize them if desired.

During the cosmic ray test run some malfunctions in the readout have been detected. It turned out that the timing of the signal flow in the PFM (Preprocessing Frontend Module) was slightly disturbed. With extensive stress tests the problem was found to be caused by the design of the back-plane shown in figure 5.15(upper) which were used. The layout of the conducting paths was done with an auto router which took no informations about the purpose of a path into account. The paths can have significant different path length and therefore different propagation times. The power lines have the same small width as the signal lines but drives much higher currents. Therefore the voltage drop was too high to keep the four PFM in a stable operational state under all running conditions. Under heavy load the voltage drop is that high that the signal propagations are partially delayed

due to longer rise time and thus edge detections so that the timing is not matching properly anymore. After these observations the backplane was completely redesigned keeping only the locations of the connectors as shown in figure 5.15(lower). The routing was done manually. It turned out that the new backplanes and the previous modification of the readout controlled by the DTU the unsparsified readout of the SFT was now running with more than 1kHz accepted trigger rate very fast and very stable.
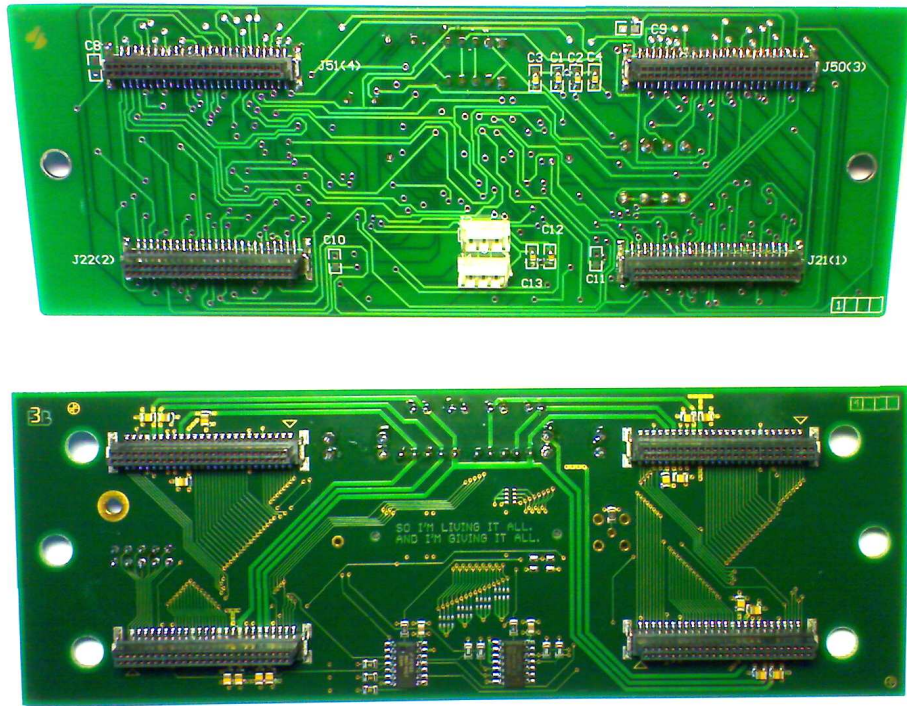

Figure 5.15: *A backplane with two layers of the first production (upper) where the designing and the routing of the conducting paths were made by the auto router. Significant different conducting path lengths and voltage drop over the undersized power lines causing improper timing thus readout malfunctions under high load. A sample of the new production with four layers and with hand made routing is shown in the lower half.*

5.3.2 Recoil Detector readout

From April 2005 until the shutdown of the cosmic ray test run in August 2005 a large amount of data where taken. The local Data acquisition was

prepared for two major modes, either connected to the HERMES DAQ or in a standalone mode.

The standalone mode is split into four sub modes.

- pedestal mode
  In this mode all available channels of all detectors were read out by self generated trigger. These data are used to measure the signal background.

- gain monitoring mode
  In order to monitor the gain of the MAPMT this readout mode where established and running unsparsified too. Similar to the pedestal mode a trigger was generated to start the digitization. in addition this signal also triggers a light source to imprint a certain amount of light led by light guides into the detector and into the reference PMT for cross check.

- reference MAPMT readout mode
  An alpha source inside the reference PMT housing was used to generate a signal which is used to trigger the digitization and the unsparsified readout. These signals are used to monitor the stability of the gain monitoring system of the MAPMT.

- cosmic ray data taking mode
  Cosmic muons where used to generate a trigger when a particle is passing through the detector. By combining certain strips a dedicated cosmic ray trigger could be provided. This mode was used to study calibrations, alignments, track reconstructions and efficiencies of the RD.

While all the preparations and tests were carried out more than 1G events (2TB data) were taken. The results from cosmic ray test run will be discussed in next sections.

5.3.3   Superconducting magnet

The setup for the superconducting RD magnet was prepared as well. For this an area was foreseen to hold the vessel with liquid helium. Even with the limited vessel volume the magnet was running for several hours to test the compatibility of the used hardware to the surrounding magnetic field. Another important issue is the preparation and test of the track finding, the reconstruction algorithm and the implemented routines as charged particles are deflected in the magnetic field. A detailed documentation about the superconducting magnet can be found in [Sta06].

5.3.4 Cosmic ray test run results

During the cosmic test run many stress tests were carried out to check possible design flaws or missing demands. As the attention for data taking and data preparation switched to the real production only few results are gathered yet.

Hit distribution for cosmic ray events

The major cosmic ray trigger setup was done by combining the lower half of the strips of the PD. As most muons are passing from upside to downside this setup ensures the particle passes through the detector as it covers the width of the detector. In figure 5.16 the hit distribution for the inner parallel SFT layer is shown. As the trigger is generated by the lower half of the PD the hit probability for the lower half are slightly higher than for the upper part. Therefore the slight asymmetry in the multiplicity is expected. As a straight vertical passing particle has a higher probability to hit several fibers per event at the side than in the middle of the barrel the two large dips are expected as well.

Realignment

The inner parallel layer consists of 21 SFT-modules with 64 fibers while the outer parallel layer consists of 18 modules with 128 fibers. As the light guides and within this the according MAPMT are counted clock wise starting at the top the fibers in the inner and outer parallel layers have an intrinsic offset. To see the correlation between the parallel layers the hits are plotted in figure 5.17 versus fiber numbers in each layer. The bisectioning line has the expected small tilt as a straight cosmic ray line enters the inner layer under a different angle than the outer layer. The mean value of the distribution projected perpendicular to the bisectioning line measures the relative rotation. The virtual relative rotation for the minimum mean value gives the relative of the layer to each other and confirms very well the expected value.

Conclusion for the cosmic ray test run

The cosmic ray test run was an important and very successful intermediate step to install the Recoil Detector. Few design flaws like broken hardware, some timing issues in the electronics and the cabling scheme of the light guides for example has been gathered and solved. After the partial disassembly some broken components were replaced so that the RD and the corresponding components were prepared to be installed during the winter shutdown in 2005.
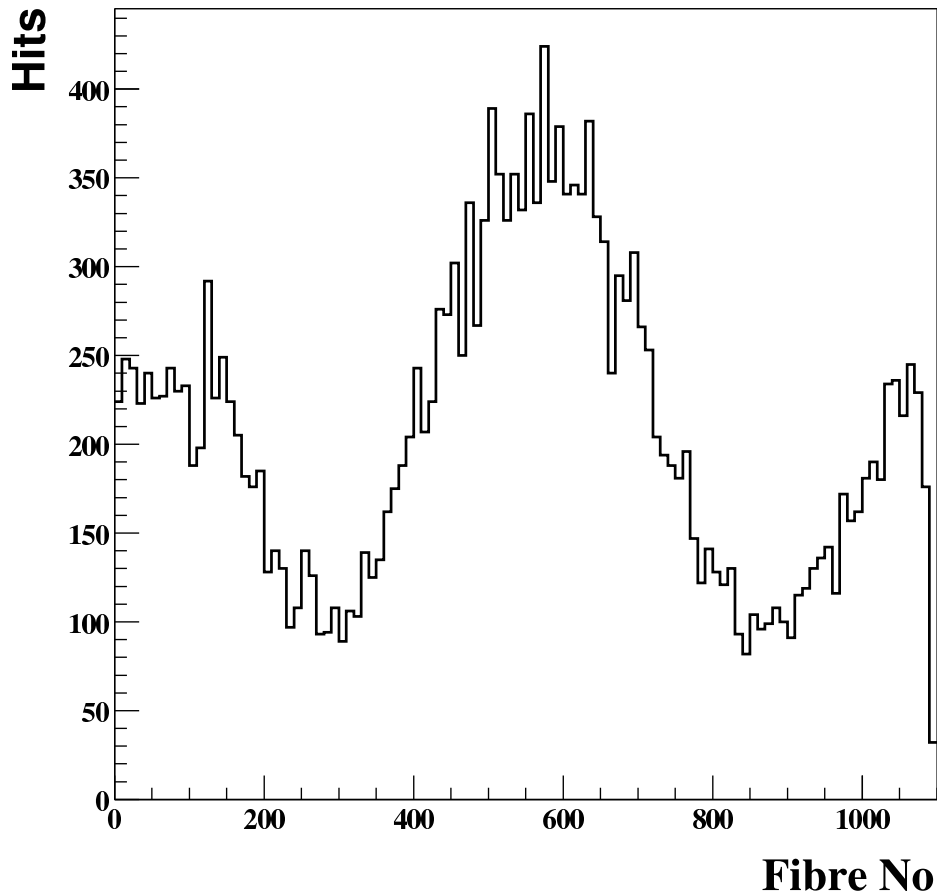
Figure 5.16:   *Hit distribution for two space point tracks for cosmic rays in the inner parallel SFT layer. The fiber 1 and 1096 are at top position downstream with clockwise counting. The trigger generation by the lower half of the PD is the reason for the asymmetry in the hit count for the upper (top around 1) and lower half (bottom around 550). The hit count around fiber 300 and around fiber 900 is due to higher hit multiplicity of vertical passing particles per event .*

5.4   HERMES experiment run

The Installation of the RD during the winter shutdown of HERA in 2005 into the HERMES detector was smooth and successful. Some results of the experimental run will be discussed in this section.
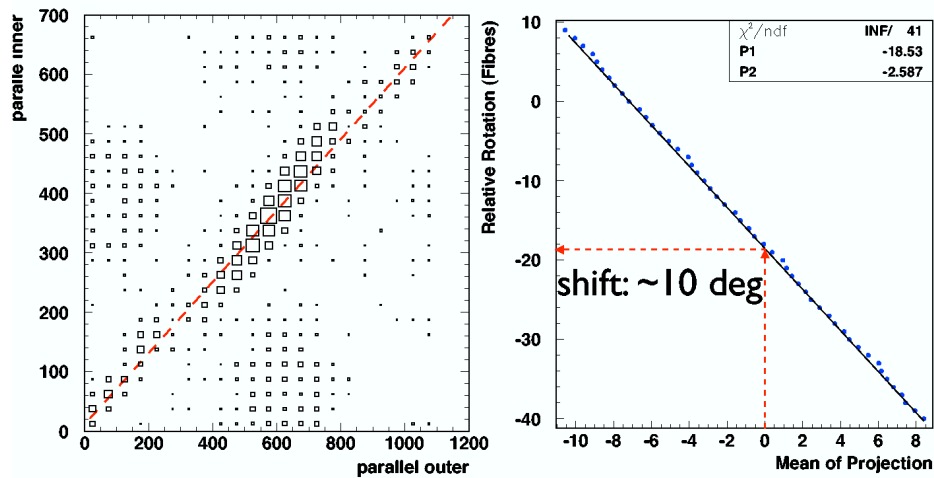
Figure 5.17: *Cross check of the SFT internal alignment. On the left side the raw fiber hits in the inner versus the outer parallel layer are plotted. On the right side the mean value of the projection of these hits by shifting certain number of fibers is shown and confirms the known offset.*

5.4.1 Production

A short introduction about the available productions and how they are generated will be introduced.

Data taking

The HERMES Detector was upgraded during the winter shutdown in 2005 with the Recoil Detector, the slowcontrol branch was adjusted and the readout of the Recoil Detector was merged into the HERMES DAQ. At the beginning an electron beam was used until the mini shutdown (June 2006) followed by a positron beam until the end of HERA. At the end of HERA running the protons energy were changed twice to make additional studies in different kinematic regions for collider experiments H1 and ZEUS. A summary of available runs is given in table 5.1.

The whole data taking interval of the RD can be separated into five periods.

1. From start to mid of March
   The RD was fully assembled. The SFT was running from the beginning. As found later neither the PD nor the SSD was fully operational until the reassembly of the RD. Furthermore the SFT-TDC might be desynchronized due to a error in the DSP assembler code which can be resynchronized again as tagging informations are available.

projectile	e^- electrons	e^+ positrons	E_{proton}/GeV
helicity in 2006			
-1 $\leftarrow\rightarrow$	1-10958		920
$+1$ $\rightarrow\rightarrow$	10959-14244	14245-43990	920
-1 $\leftarrow\rightarrow$		43991-48195	920
helicity in 2007			
-1 $\rightarrow\rightarrow$		1-17981	920
$+1$ $\leftarrow\rightarrow$		17982-34735	460
$+1$ $\leftarrow\rightarrow$		34736-40840	575

Table 5.1: *List of runs of accumulated data samples with Recoil Detector helicity states parallel ($+1$ $\rightarrow\rightarrow$) and anti-parallel (-1 $\leftarrow\rightarrow$) to the beam direction. At the end of HERA running the energy of the protons were varied for studies in different kinematic regions for collider experiments H1 an ZEUS. HERMES was running with electron and positron beam only but the background might be dependent on proton beam energy.*

2. From mid of March to beginning of May
   The background signal in the SSD jumped suddenly clearly to higher contribution. During the maintenance access beginning of May some collimators were removed to look inside the target area. A burned hole was found as most likely reason for the sudden increased electrical noise in the SSD. Unfortunately during the reassembly of the target cell was crunched. This was the cause for very high parasitive radiation while trying to get HERA running again and therefore part of the SSD was damaged by these radiations. In order to repair the SSD it was removed.

3. From beginning of May until end of June
   The SSD was absent for repair while PD and SFT was partially recabled up again for some studies and fixing all the remaining problems.

4. from end of June to beginning of September
   The complete RD was reassembled and under commissioning again.

5. from September to the end of HERA
   The RD enters the fully operational phase and running smooth even after the shutdown of HERA for cosmic ray data taking for additional alignment and calibration.

During the data taking with electron beam only the SFT part of the RD was operational. As the additional space points of the SSD are not available the resolution of the reconstructed track with only the SFT will drop in the low momentum region. On the other side the extrapolation of

kinematic variables in the limit $t \to 0$ will be difficult as the SSD covers the low momentum region. Therefore the analysis of the electron data of the Recoil Detector for physical content will be challenging.

Preparation of data

The raw data taken with the HERMES DAQ [Her+03] was stored on the tape robot in the EPIO (Experimental Physics Input Output) format [McL+93]. This EPIO format was designed at CERN. Processed data productions are stored in the DAD (Distributed ADAMO Database) [Wan+95] format which was developed by the HERMES collaboration. The DAD format using the entity-relationship database of ADAMO (ALEPH data model) [ADA95] as underlying layer.

In order to provide data for physical analysis a two level data processing were created at HERMES. The first process called HRC(HERMES reconstruction)-production is used for studies of the detectors and for determine configuration data like calibration, alignment and other time dependent properties. The data of the first process are merged afterwards together with the slowcontrol data by the second process called DST(Data Summary Tape)-production in order to provide high quality data for physics analysis.

In order to generate the HRC-productions the raw data from the tape robot are piped through several level of post processing routines. The first major task is to translate informations like rack numbers, crate numbers, module numbers, channel numbers to geometrical information like coordinates upon a time based lookup table. In the second stage the raw signal values are translated to informations like energy depositions or timestamps. The third stage is combining these information to reconstruct tracks. In a first step short tracks within sub detectors are searched and in a second step these short tracks are combined to long tracks which covers the complete trajectory of a particle. Due to characteristic behavior of particles the response in the sub detectors are combined to give likelihoods of the detected particle. Finally the extracted informations are used to calculate the parameters for alignment and for calibration and to determine the efficiencies of the production. Investigations made with these productions are used to gather parameters for the next iteration.

The HRC-production follows the naming convention **YYv** where **YY** are the two least significant decimal digits of the year and **v** the version of the production. For the DST-production the data stream of the slowcontrol branch are merged with the HRC-production. Due to this the naming convention for the DST-productions **YYvr** are correlated to the underlying HRC-production with **r** as the additional revision number. These DST-productions are now used to physics analysis. Nevertheless important informations for the HRC-productions can be gathered by comparing DST-productions of different years.

As all the time new algorithms and research tools are implemented and codes are bug fixed. As the understanding in detector calibration reaches saturation some versions of production are frozen and physics analysis starts. For the following overviews the HRC-production 06d and the DST-production 06d0 were used which was released recently. For investigations with the Recoil Detector the track reconstruction method 7 was used as the final tracking method is not settled down yet. Especially the usual event selections are applied to be comparable to other analysis in this field. More investigations and results on previous productions with the Recoil Detector are documented in [Vil08] and constantly updated on [Her+08].

5.4.2 Overview of elastic scattering events

Elastic scattering of electrons or positrons on protons is a clean and simple way to study the intersection of the whole HERMES forward spectrometer with the Recoil Detector. In order to select an elastic scattering event few criteria are requested. The event has to have exactly one track of the scattered beam particle. The energy of this particle must be above $25.5 GeV$ and below the beam particle energy. The starting vertex have to be between $0 cm$ and $25 cm$ in z-direction which is along the beam axis and at a distance below $0.75 cm$ to the beam axis.

Some geometrical properties measured by the HERMES forward spectrometer are compared with those measured by the Recoil Detector. The vertex reconstruction in z-direction (see figure 5.18) of the scattered beam lepton by the HERMES forward spectrometer shows a clear correlation to the vertex of the recoiled particle reconstructed with the data available by the Recoil Detector and the difference of these values are narrow.

The reconstructed polar angle (see figure 5.19) is a weaker crosscheck as the distribution by the HERMES forward spectrometer is smeared due to the large level arm to the calorimeter. Nevertheless the transverse components of the polar angle are in good agreement.

The azimuthal angle (see figure 5.20) reconstructed by the spectrometer has to have the opposite direction to the one reconstructed with the RD due to momentum conservation. As the geometrical component parallel to the beam axis is not involved the adjusted azimuthal angles has very narrow correlation. The width of the distribution is almost as small as the expected azimuthal resolution of the SFT.

In summary, even in this early stage the results are already in promising good agreement with previous productions and with expected performance.

5.4.3 Overview of Deep Inelastic Scattering events

Another set of events for cross check of the performance of the detectors are deep inelastic scattering processes. In this case only the scattered beam
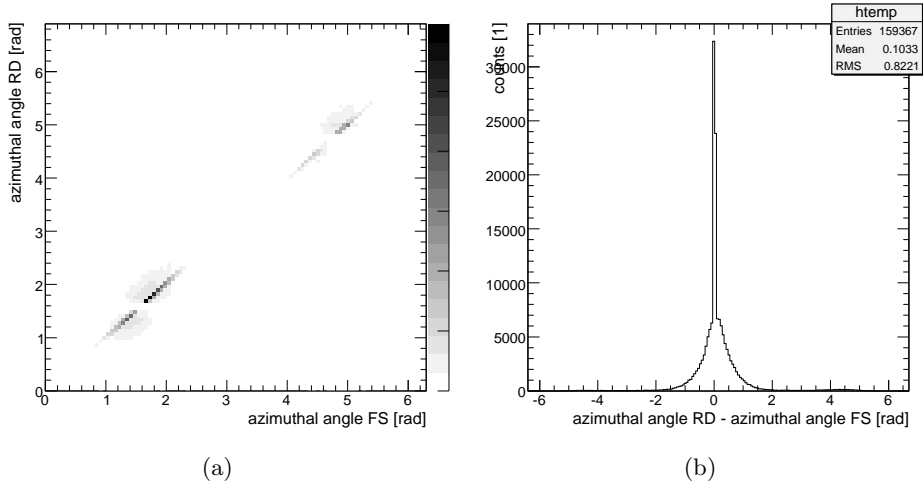
(a)   (b)
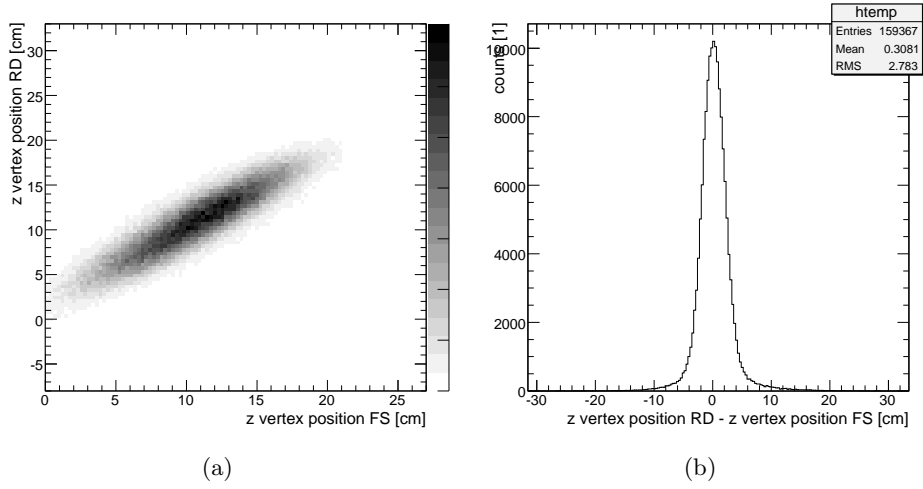
Figure 5.18:   *The correlation for elastic events between HERMES forward spectrometer (FS) and Recoil Detector (RD) for the vertex in z-direction is in good agreement. (a) 2D-plot of vertex position along the beam axis. (b) Distribution of the differences.*
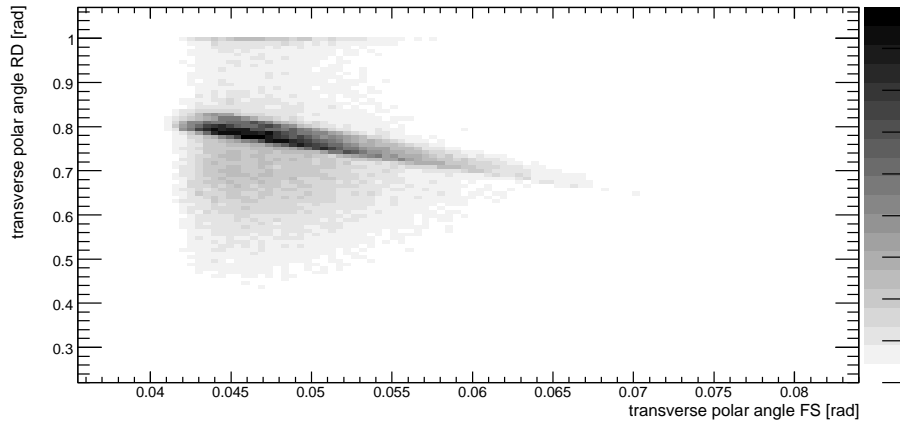
Figure 5.19:   *Correlation for elastic events between HERMES forward spectrometer (FS) and Recoil Detector (RD) as 2D-plot of transverse polar angle θ component is smeared due to limited resolution in the HERMES forward spectrometer. Few remaining background is visible.*

particle has to be detected in the final state and given therefore an simple probe.

For the event selection a designated bit pattern (0x441e1bce) [Her+08] of the data quality was used which contains general informations about the

Figure 5.20:   *Correlation for elastic events between HERMES forward spectrometer (FS) and Recoil Detector (RD) for the azimuthal angle is in a very good agreement. (a) 2D-plot of azimuthal angle. (b) Distribution of the differences. The small peak is as small as the fiber diameter of the SFT.*

rating of the data. Furthermore the usual and extended fiducial volume cuts were applied to ensure that detected and scattered beam lepton passes from the interaction region in the target cell to the electromagnetic calorimeter. The vertex has to full fill $5 < VertexZ/cm < 20$ for the z-direction and has to have a smaller distance from the beam axis than $0.75cm$. For the following kinematic variables the requirements to ensure DIS regimes are listed in table 5.2

variable	unit	lower limit	upper limit
x	1	0.03	0.35
Q^2	$(GeV/c)^2$	1	
W^2	$(GeV/c)^2$	9	
ν	GeV		22

Table 5.2:   *List of some kinematic cuts for deep inelastic scattering event.*

The distributions of the usual observables for the 06d0 productions are summarized in figure 5.21. The triangle shape of the reconstructed vertex in z-direction is in good expectation. The gas target is injected at $z = 12.5cm$ with the highest density and are pump out at the two ends of the target cell. The shape of the distribution of the vertex distance to the beam axis are indicating a close to beam axis interaction area as well. The ϕ-distribution of the scattered beam lepton reflect the upper and lower half of the HERMES

forward spectrometer very well. Together with the θ-distribution of the scattered beam lepton the acceptance of the forward spectrometer is indicated as well. The distributions of the transfered momentum fraction and the transfered energy fraction is as expected too. In total, these observables are in a good agreement with previous data productions.

5.4.4   Overview of DVCS events

For the event selection of DVCS additional requirements are needed in order to ensure exclusivity. The event has to consists of exactly one scattered beam lepton and exactly one real photon. The momentum transfer Q^2 due to the scattered beam lepton has to be below $10 GeV^2$. Beside the fiducial volume cut for the real photon the energy deposition in the H2 preshower must be above $0.001 GeV$ while the energy deposition inside the electromagnetic calorimeter must be above $3 GeV$. The calculated angle $\theta_{\gamma^*\gamma}$ between the virtual photon and the produced real photon has to be in the range between $5 mrad$ and $45 mrad$. The constrained four momentum transfer t_c

$$(5.1) \qquad t_c = \frac{-Q^2 - 2\nu \left(\nu - \sqrt{\nu^2 + Q^2} \cos\left(\theta_{\gamma^*\gamma}\right) \right)}{1 + \frac{1}{M_p} \left(\nu - \sqrt{\nu^2 + Q^2} \cos\left(\theta_{\gamma^*\gamma}\right) \right)}$$

between initial and final nucleon of the momentum transfer to the target calculated in the laboratory frame with the missing invariant mass value must be above $-0.7 GeV^2$. The squared missing invariant mass M_x^2 has to be in the range $-2.25 GeV^2$ to $+2.89 GeV^2$.

The distributions of the usual kinematic observables are shown in figure 5.22. The distribution of the squared four momentum transfer Q^2 by the scattering beam lepton reflect the constraints to have more statistics but to ensure factorization. The center of mass distribution of the system consisting of the real photon and the recoiling target has the required limitation of $W^2 > 9 GeV^2$. The restriction for the transfered momentum fraction x to the target limits the correlated transfered energy fraction y accordingly. To ensure the selection of deeply virtual Compton scattering from Bethe-Heitler process the angle between the virtual photon to the real photon are limited accordingly while the distribution of the energy of the real photon are intrinsic inside the boundaries.

In figure 5.23 the distribution of the squared four momentum transfered to the target with respect to the missing invariant mass is shown. To reject background exclusivity the events of the exclusive regions are requested. The pure calculation of the squared four momentum transfer with the proton mass for a hydrogen target achieves to a broad distribution around zero. This does not reflect the true kinematics. By using the missing invariant
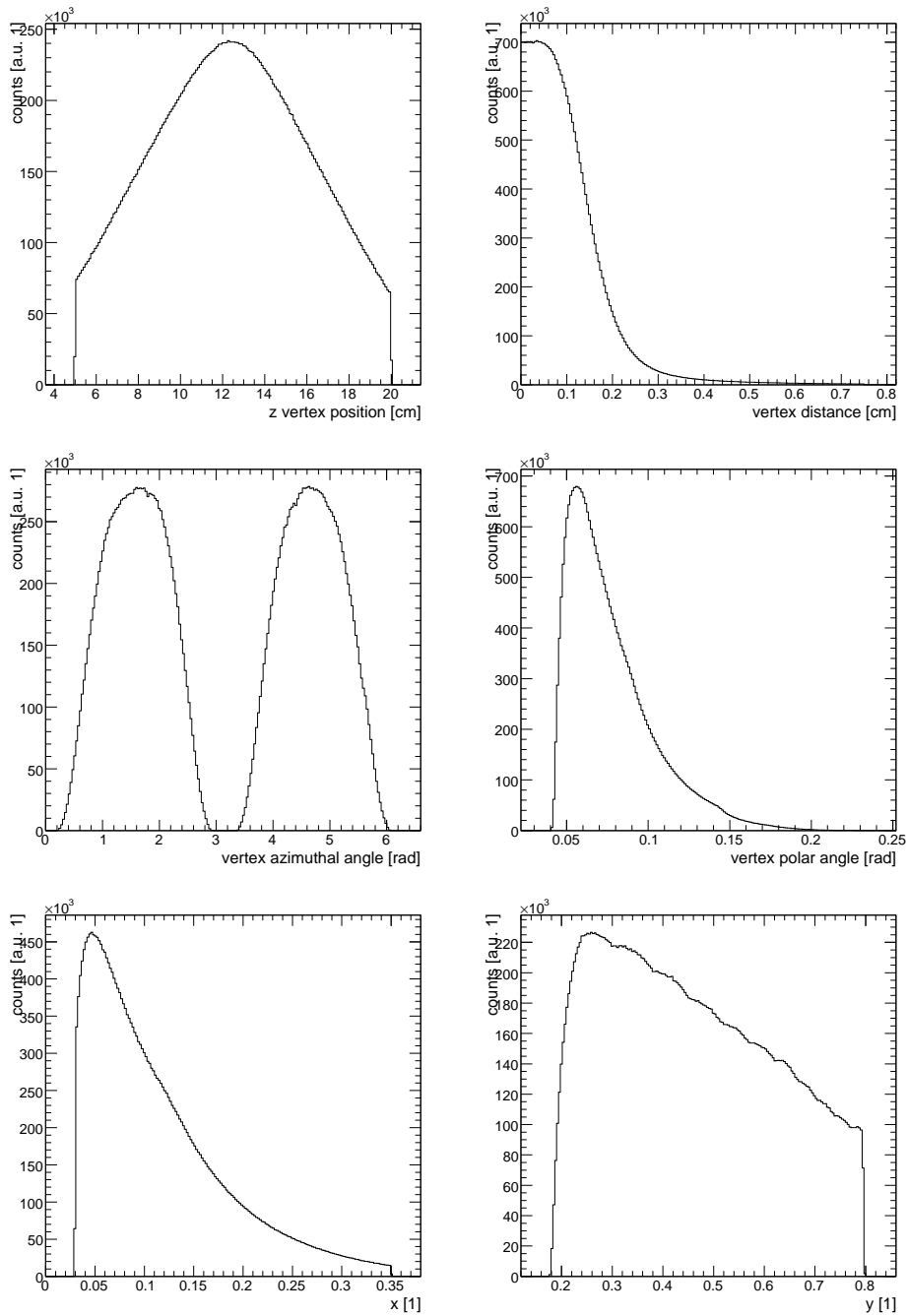
Figure 5.21:   *General kinematic variables of the HERMES forward spectrometer gathered by measuring the scattered beam lepton only in good agreement with previous data productions.*
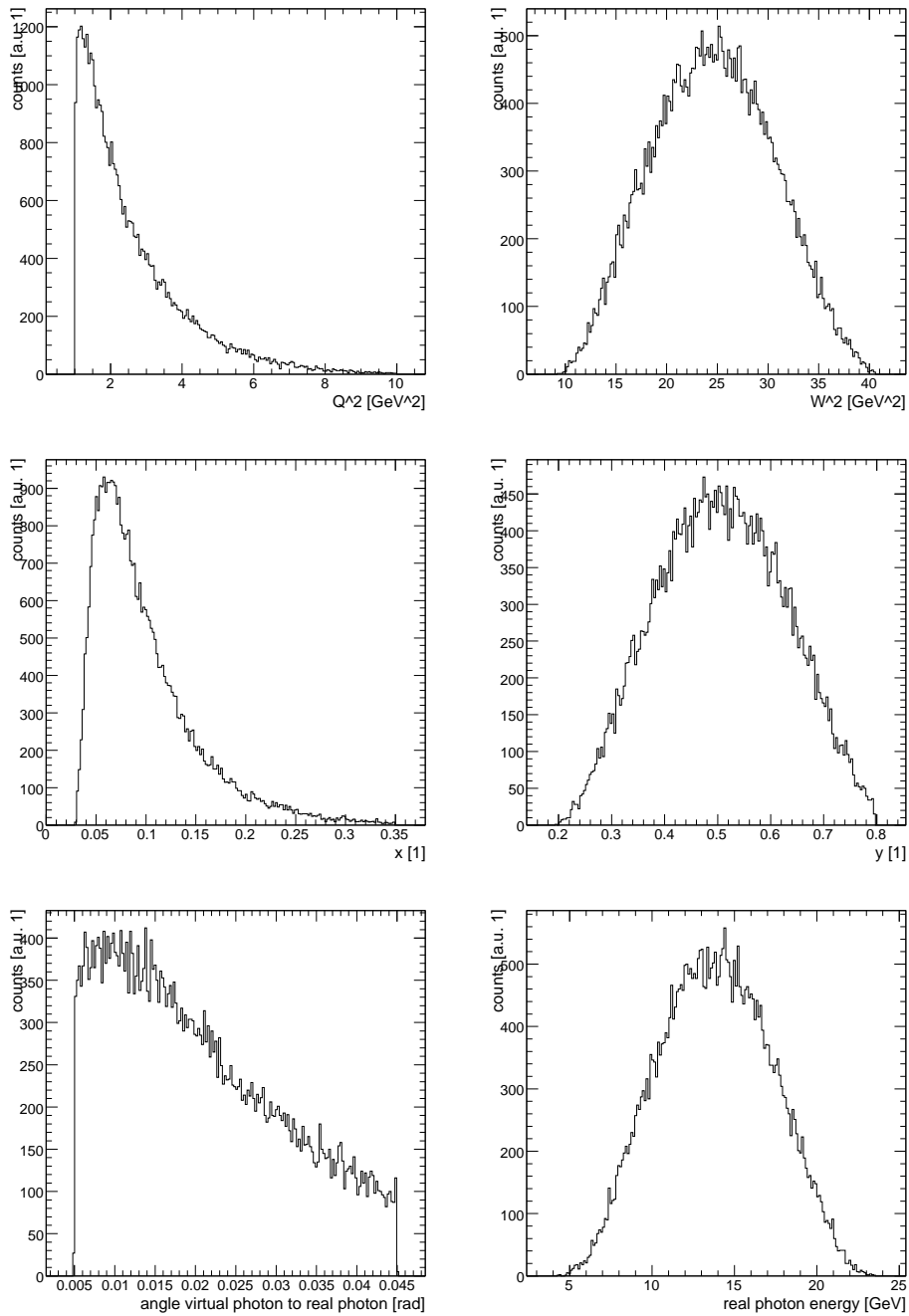
Figure 5.22: *General kinematic variables of the HERMES forward spectrometer gathered for DVCS events in good agreement with previous data productions.*

mass to calculate this observable the shape looks like expected and is below zero as a space like property.

Figure 5.24 shows the different shape in the distributions of the vertex distance for the 06b2 and for the 06d0 data production. After the realignment for the 06d production the distribution is closer to the beam axis. Further studies of the impact of the realignment is currently under investigation.

As result, the general observables agree very well to those of previous productions as well.

5.4.5   Overview of Azimuthal Asymmetry

Events which fulfill the requirements of hard exclusive processes are used to calculate the azimuthal asymmetries. During the data taking with the RD the gas target was unpolarized, thus beam spin asymmetry and beam charge asymmetry can be accessed. As mentioned before the latest data production 06d/06d0 was used to access these azimuthal asymmetries.

The distributions for the missing invariant mass shown in figure 5.25 indicate small beam charge dependency for the exclusive part but not for the broad semi-inclusive region. The reason might be a not yet perfect calibration of the calorimeter which is currently under investigation. The wavelike deviation in the angle ϕ between the scattered plane and production plane as shown in figure 5.25 is not taken into account as well. As the calculations of the azimuthal asymmetries are not yet cross checked the data points are not fitted.

Beam Spin Asymmetry

In case of beam spin asymmetry the selected events are sorted by the helicity of the beam projectiles. The values plotted in figure 5.26(a) are determined by calculation of

$$(5.2) \qquad\qquad A_{LU} = \frac{1}{<P_B>} \frac{N^+ - N^-}{N^+ + N^-}$$

whereas A_{LU} is the Amplitude for longitudinal polarized beam (L) and unpolarized target (U) while N^+ and N^- are the relative numbers of events with parallel and anti-parallel beam helicity. The beam polarization is taken into account by the averaged beam polarization $<P_B>$. The error bars are larger than expected by previous analysis [Vil08] while the shape roughly follows previous results.
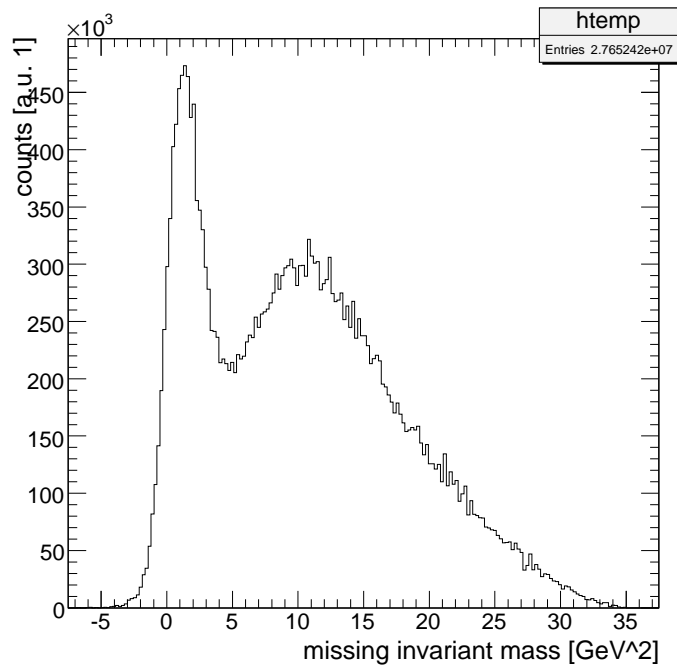
(a)
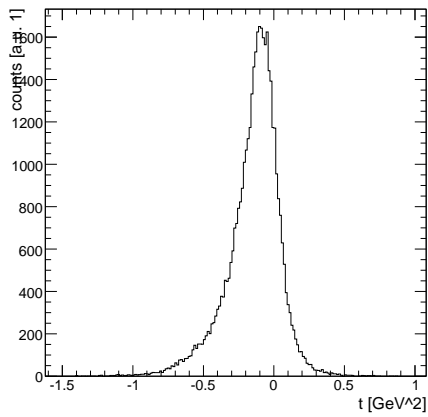
(b)
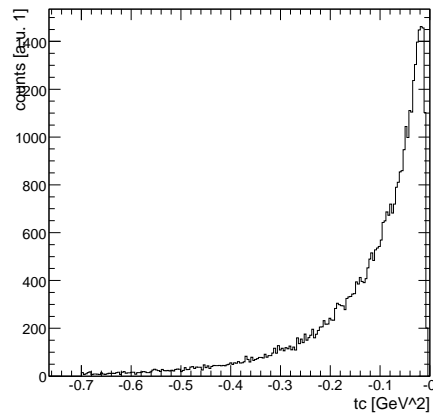
(c)

Figure 5.23: *Distribution of the invariant missing mass are shown in (a) after applying all cuts for DVCS event selection. For exclusive region the range from $-2.25GeV^2$ to $+2.89GeV^2$ is assumed. Distributions of squared four momentum transfer to the hydrogen target with constant proton mass calculation (b) and with missing invariant mass calculation (c) for the exclusive region which is in good agreement with previous results.*

(a)   (b)
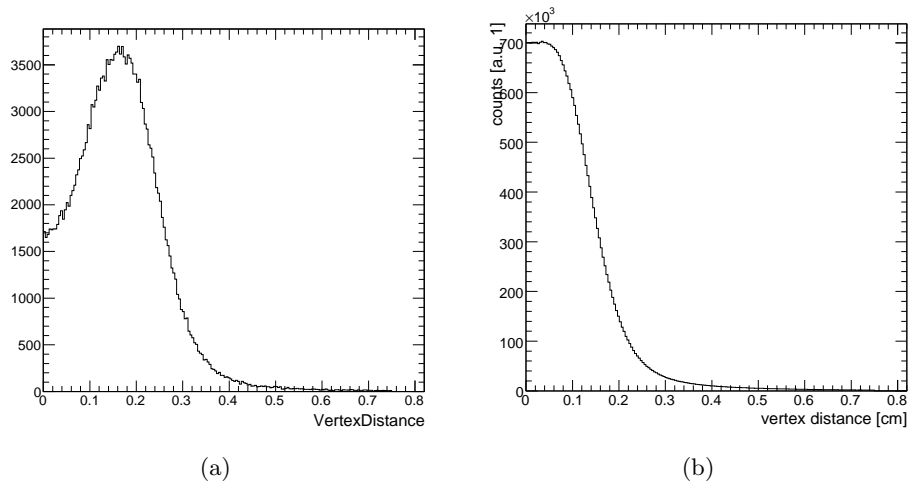
Figure 5.24:   *Distributions of the vertex distance for the 06b2(a) and for the 06d0(b) [Vil08] data productions for comparison. The shift to lower values are due to change in the HERMES internal coordinate system.*

(a)   (b)
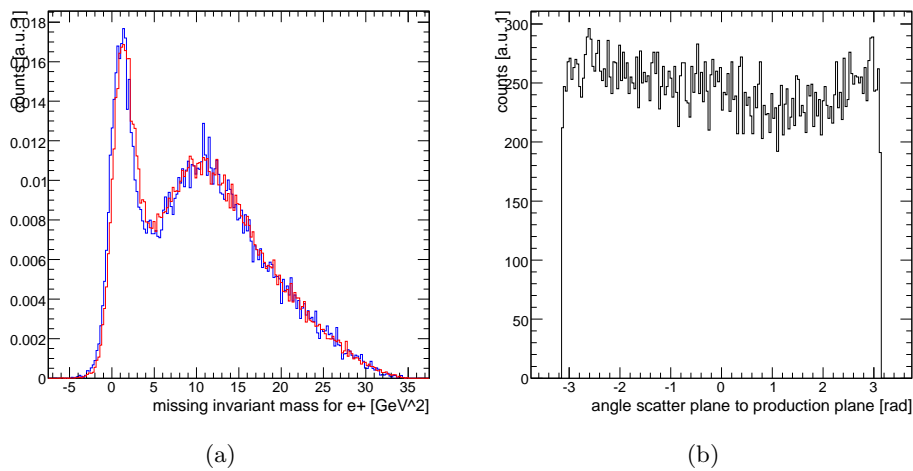
Figure 5.25:   *Small side effects currently under investigation. (a) Small shift in the response by the calorimeter for electrons (blue) and positrons (red) for missing mass distribution for the exclusive region. (b) Wavelike differences in angle distribution between scattering plane and production plane.*

Beam Charge Asymmetry

In case of beam charge asymmetry which is unique at HERA, the exclusive events are sorted by the charge of the beam particles and the values plotted
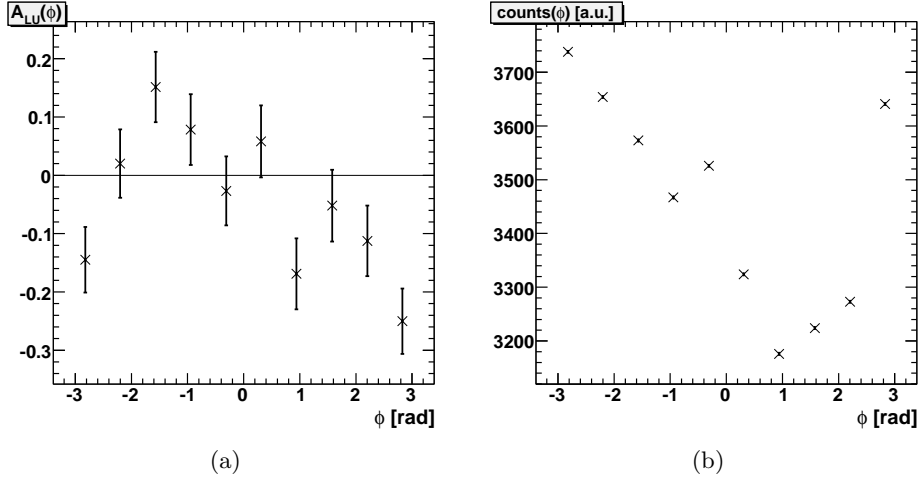
Figure 5.26:   *(a) φ dependency of the leading amplitude of the beam spin asymmetry. (b) Differences in available data per bin in φ can lead to small deviations.*

in figure 5.27 are calculated with respect to

$$(5.3) \qquad\qquad A_C = \frac{N^+ - N^-}{N^+ + N^-}$$

whereas A_C denotes the amplitude of the beam charge asymmetry. The relative number of events with positrons or electrons are N^+ and N^-. The error bars and the shape of the curve are closer to previous results [Vil08].

5.4.6   Overview of SFT response

One of the key contribution of the SFT is the particle identification. By combining the reconstructed momentum of the recoiled particle to the energy deposition particle separation is possible. The correlation between these parameters is shown in figure 5.28. Events with required two space points in the SFT - one in the outer barrel and one in the inner barrel - show a separation between pions and protons with a small overlap region. By requesting events with four space points - two in the SSD and two in the SFT - a clear separation between pions and protons is possible and a likelihood based particle identification might be implemented in the future as well.

5.4.7   Overview of improvements by the Recoil Detector

The contribution to improve exclusivity of DVCS samples by the Recoil Detector is shown in this section. As reminder the reaction of DVCS events can be expressed by

(a)

(b)
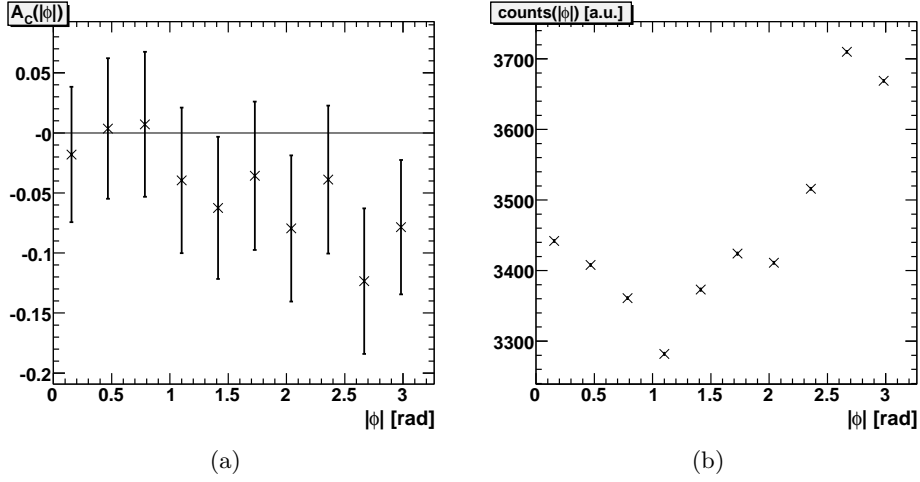
Figure 5.27: *(a) $|\phi|$ dependency of the leading amplitude of the beam charge asymmetry. (b) Differences in available data per bin in ϕ can lead to small deviations.*

(5.4)
$$l + p \rightarrow l' + \gamma + p'$$

where l and l' are the initial and scattered lepton, γ is the generated real photon and p and p' are the initial and scattered proton.

The three-momentum p'^{FS} of the previously undetected scattered proton is calculated with data measured with the HERMES FS (forward spectrometer) by the missing invariant mass technique. With the RD (Recoil Detector) the three-momentum p'^{RD} of the recoiling proton is measured directly.

The correlation of these three-momenta is shown in figure 5.29. On the left in figure 5.29(a) the difference of the x-component versus the difference of the y-component of these three-momenta are shown. The distribution is focused clearly below $100 MeV$. On the right in figure 5.29(b) the correlation of the ϕ-components are shown. As expected the distribution is concentrated on the bisectioning line. The clear horizontal gaps in the acceptance of the Recoil Detector caused by the holding frame of the SSD is visible. Additional the quadrant $0 < p'^{RD}_{\phi}/rad < \pi/2$ for the RD has lower counts due to higer noise in the SSD.

The distribution of the difference of the ϕ-component of these three-momenta is shown in figure 5.30. The black solid line is a Gaussian fit within the range of $\pm 0.1 rad$ and gives $\sigma = 0.094 rad$. The red part is the 3σ range, which is used to improve exclusive event selection.

Figure 5.31 shows the distribution of the missing invariant mass M_x^2 which is normalized for better comparison. For the black curve all general

event selections for DVCS events except for M_x^2 are performed. The usual event selection on the missing invariant mass M_x^2 for exclusive events is from $-2.25 GeV^2$ to $+2.89 GeV^2$. Requesting a single proton track above the solid line in figure 5.28(b) results to the blue curve in figure 5.31(a). For the red curve the additional requirement is to have a coincidence for the missing proton between HERMES Forward Spectrometer and Recoil Detector within 3σ for the p'_ϕ distribution as shown in figure 5.30. The blue curve in figure 5.31(b) results if events with only a pion in the Recoil Detector are requested. Even without the final alignments and calibrations a clear improvement by the Recoil Detector is visible as the contamination is reduced. In future, with an improved tracking and particle identification much better results are expected.

5.4.8   Conclusion and Outlook

The recently released HRC-production 06d and the DST-production 06d0 are used to discuss the current state. The distribution of usual observables has the expected shape and are in good agreement with previous productions. The positron data investigated with the Recoil Detector give expected results too.

Nevertheless some challenging tasks are still waiting for investigations. Some previous studies show that there is a slight difference in the response of the electromagnetic calorimeter for electrons and positrons. Beside this the final calibration and alignment of all detector parts are performed currently. The positron data gives a possibility to tune the tracking system and particle identification system of the Recoil Detector for the electron data as only data taken with the SFT are available yet.

A lot of new informations about the response of the upgraded HERMES detector can be gathered by the study of the data with the Recoil Detector. By iterating of previous analysis with these new informations improvements will be possible to review the map of the constituents of the nucleon spin budget.
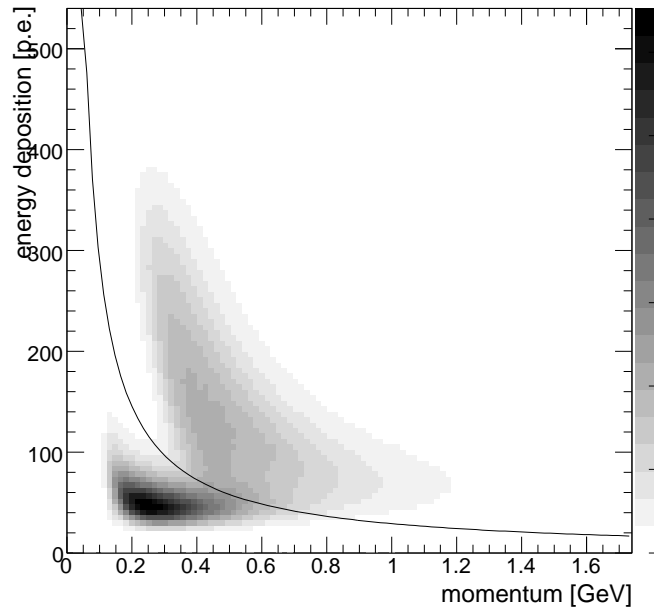
(a)
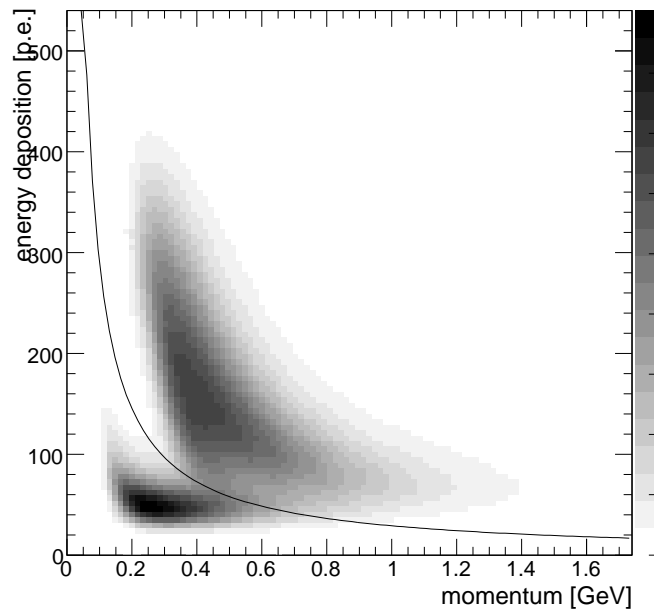
(b)

Figure 5.28:   *Correlation between energy deposition (in units of photo electrons) inside the SFT and the reconstructed momentum of the track (in GeV). The distributions shows a separation between lower left pions and protons with requirements of two space points in the SFT (a) and with the requirements of four space points in SFT and SSD together (b). The solid line indicates a possible separation by dE * p = 29.**
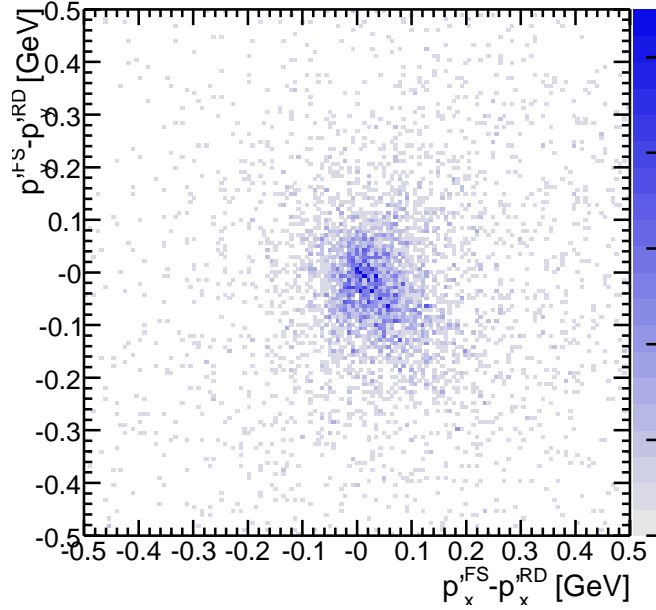
(a)
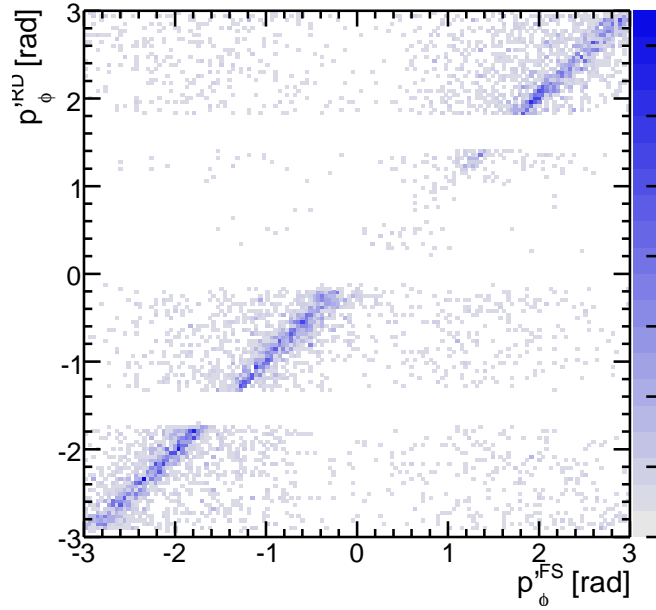
(b)

Figure 5.29: *Correlation between several components of the three-momenta p'^{FS}, p'^{RD} of the recoiled proton, which are calculated by the missing invariant mass technique using the HERMES FS and by measurement with the RD. (a) Correlation for the differences in the x-components versus the differences in the y-components. (b) Correlation between the ϕ-components. The horizontal gaps due to the holding frame of the SSD and the additional lower counts for the quadrant $0 < p_\phi^{RD}/rad < \pi/2$ due to higer noise in the SSD is clearly visible.*
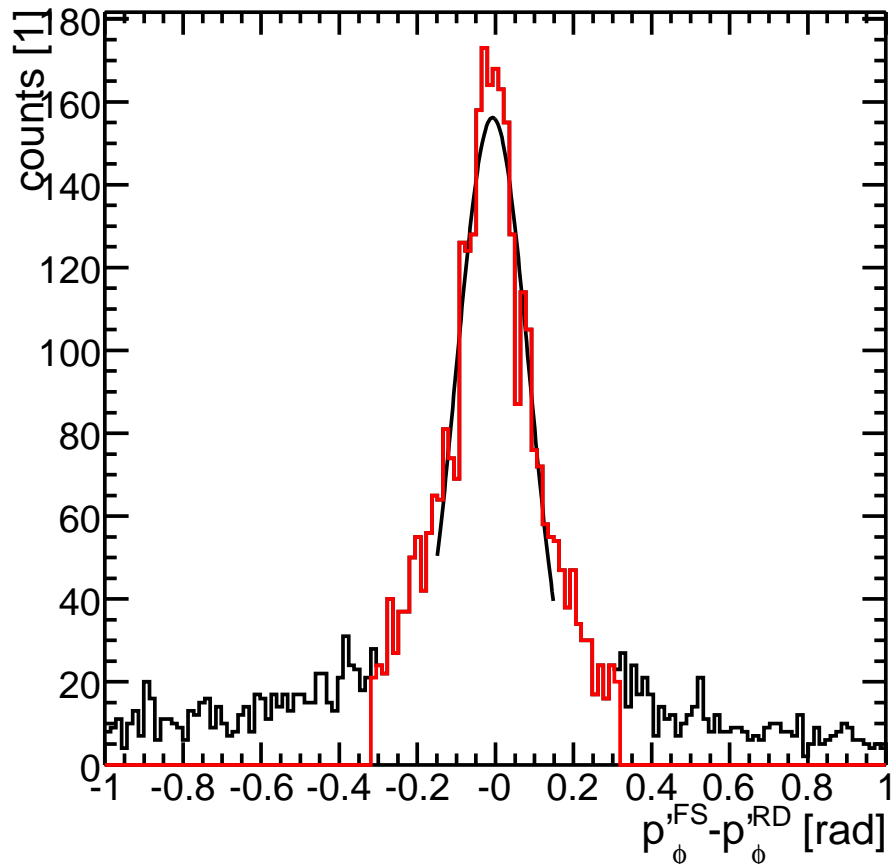
(a)

Figure 5.30: *Distribution of the p'_ϕ difference calculated with data available from FS and with data measured with RD. A fit with an Gaussian function (solid black line) in the range $\pm 0.1 rad$ results to $\sigma = 0.094 rad$, whereas a 3σ range (red) is used to improve exclusive event selection.*
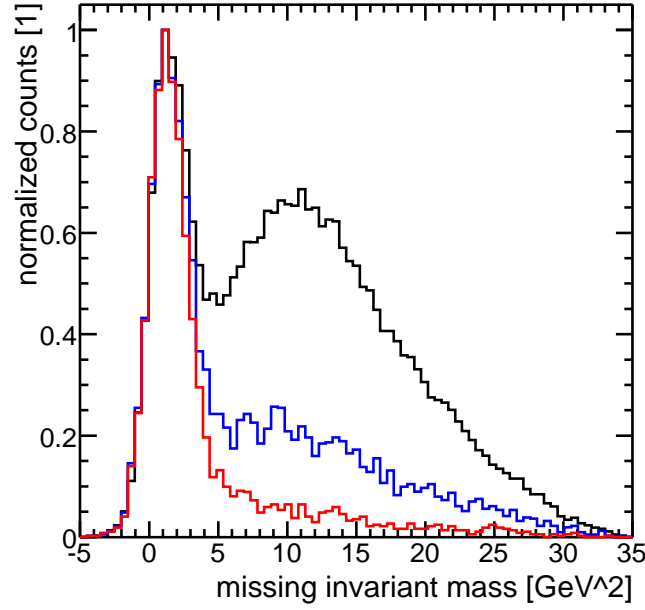
(a)
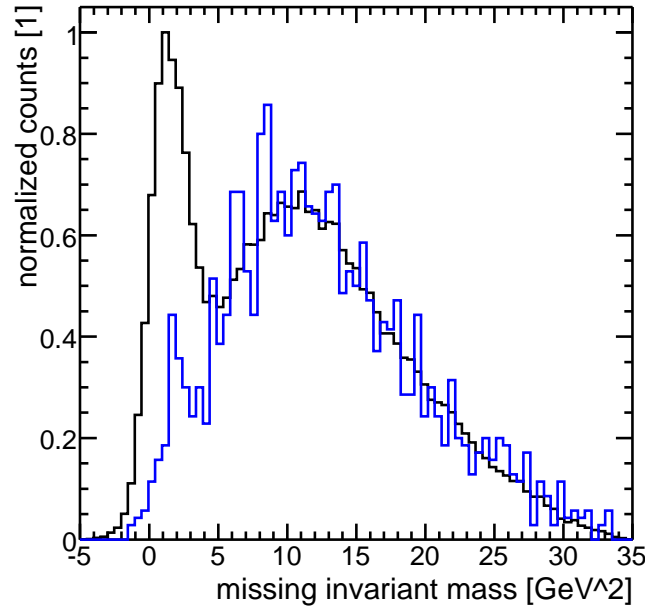
(b)

Figure 5.31: *Arbitrary normalized missing invariant mass distribution mea-sured with the HERMES Forward Spectrometer only (black) and with the contribution by the Recoil Detector on event selection for DVCS candidates. (a) Additional request of a single proton track (blue) and furthermore a coincidence for the missing proton between HERMES Forward Spectrometer and Recoil Detector within 3σ of the $p'^{FS}_{\phi} - p'^{RD}_{\phi}$ distribution. (b) Additional request of a single pion track (blue).*

Chapter 6

Summary

The standard model of particle physics is available to describe the the atomic world. Nevertheless the constituents of atoms like electrons, protons and neutrons are not completely understood. While the electrons seems to have point like properties the protons and the neutrons behave like compounded objects. The current standard model to describe protons and neutrons is based on quarks as partons, whereas photons, gluons, W- and Z-bosons are the carrier of the electromagnetic, the strong and the weak forces. In this model the aspect of gravity is not yet taken into account. Furthermore on large distance scale the calculations are not solved analytical yet. One particular problem is the incomplete nucleon spin budget as well. Measurements at EMC (European Muon Collaboration) showed that the naive picture that three quarks contribute to the nucleon spin budget is not matching.

The GPDs (Generalized Parton Distributions) illustrated in figure 6.1(a) are a recently developed model to describe transverse spatial distributions and longitudinal momentum distributions simultaneously without violating the uncertainty relation. The transverse spatial distributions named FFs (Form Factors) can be measured by elastic scattering, while the longitudinal momentum distributions named PDFs (Parton Distribution Functions) are measurable by deep inelastic scattering. GPDs are not only a combination of these two other models, rather new informations getting available. For example the sum rule researched by Ji gives the opportunity to access the nucleon spin budget.

These GPDs can be measured with hard exclusive reactions where a scattered projectile interacts via a virtual photon. As an hard exclusive reaction the target stays after interaction intact and all produced particles are detected. Furthermore the GPDs can be measured selectively by the requested final state. For example ρ^0 meson production enables the access to distributions of quarks and of gluons of the same and of linear order.

But the cleanest way to access GPDs is DVCS (deeply virtual Compton scattering) as shown in figure 6.1(b). Due to same initial and final state the
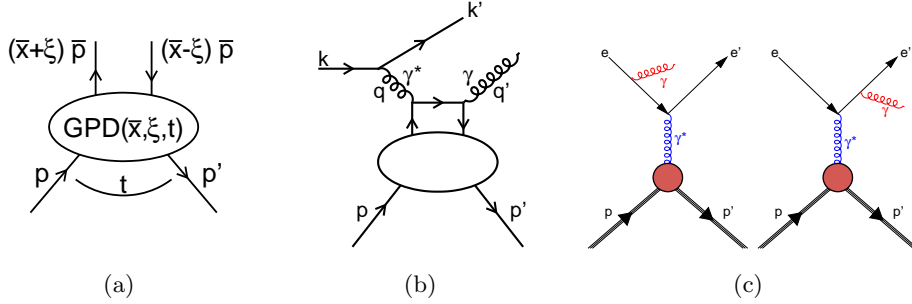
Figure 6.1:   (a) Description of GPDs by average longitudinal momentum fraction $\bar{x}$, fractional longitudinal momentum transfer ξ named skewness and momentum transfer t. (b) Principe of deeply virtual Compton scattering (c) Indistinguishable initial and final state of the Bethe-Heitler process.

elastic BH (Bethe-Heitler) process is indistinguishable (see figure 6.1(c)). In order to calculate the cross section the amplitude of the photo production by BH τ_{BH} and by DVCS τ_{DVCS} are added together to the combined amplitude τ by

$$(6.1) \qquad |\tau|^2 = |\tau_{BH}|^2 + |\tau_{DVCS}|^2 + \tau_{BH}^* \tau_{DVCS} + \tau_{DVCS}^* \tau_{BH}.$$

For the kinematic range at the HERMES experiment the amplitude of the BH process is much larger than for DVCS by more than one order. As the pure BH contribution can be precisely calculated in the frame of quantum electro dynamics and by neglecting in leading order the pure DVCS contribution the mixed interference term gives the opportunity to access GPDs.

One of the experiments carried out to make more investigations on the nucleon spin budget is the HERMES (HERA measurements of spin) experiment at HERA (Hadronen Elektronen Ring Anlage) at DESY (Deutsches Elektronen-Synchrotron) in Hamburg / Germany. The HERMES forward spectrometer as shown in figure 6.2 was designed to access the nucleon spin budget by DIS (deep inelastic scattering). Due to better understanding and new models like GPDs in the meantime the scientific program of HERMES was widely extended by investigations of different polarized gas targets.

The HERMES detector consists of a tracking system to measure the momentum of charged particles which are deflected in the magnetic field of the HERMES magnet. A set of detectors provide a high efficient particle identification in order to reconstruct scattering processes. Even the recoiled particle can not be detected at HERMES due to the polarized target facility exclusive reactions can be still investigated by the missing invariant mass technique M_x^2 which is illustrated in figure 6.3. Due to the limitation
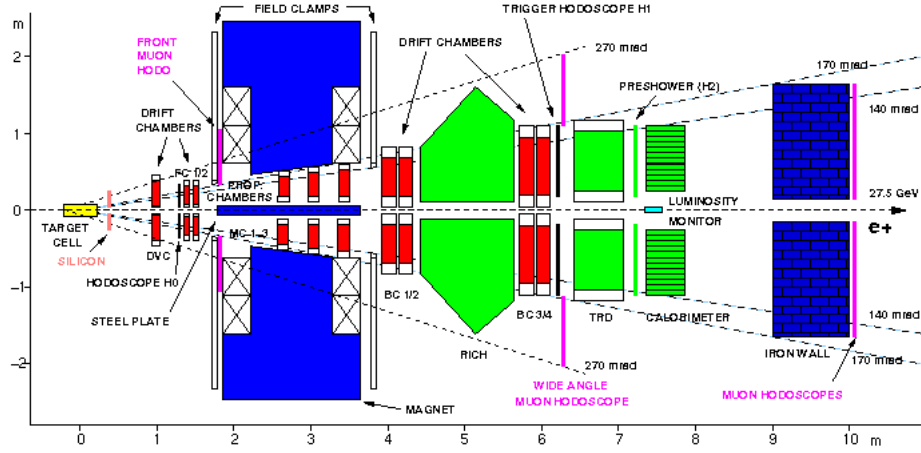
Figure 6.2: *Schematic of the HERMES forward spectrometer. The tracking system is colored in red, while the particle identification system is in green. Dashed lines indicate acceptance range.*

of the resolution by the HERMES forward spectrometer the background contamination is around 15%.
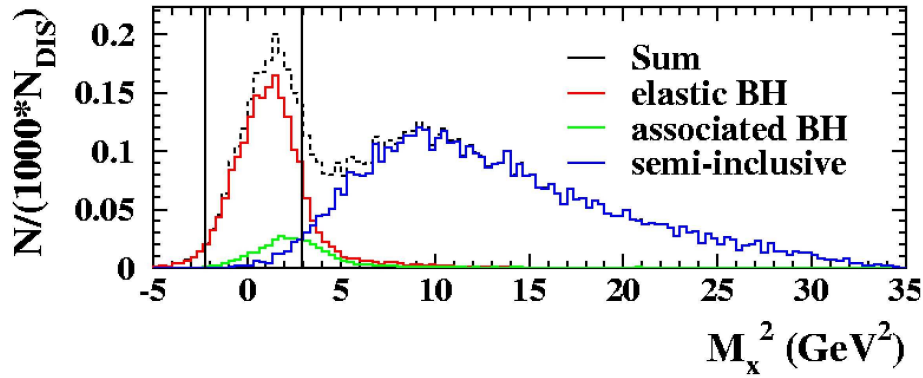
Figure 6.3: *Missing invariant mass distributions for different reactions studied with Monte Carlo simulations. Exclusive region indicated by vertical solid lines is in the range of $-2.25 GeV^2$ and $+2.89 GeV^2$. The contamination is around 15%.*

In order to improve exclusivity and the resolution of kinematic variables, the collaboration decided to upgrade the HERMES forward spectrometer with the Recoil Detector. As this new part of the HERMES Detector surrounds the target area recoiling particles can be detected due to the big

acceptance. This Recoil Detector consists of three sub detectors as shown in figure 6.4. A SSD (Silicon Strip Detector) which stays in the beam vacuum of HERA is the inner part. In the middle part the SFT (Scintillating Fiber Tracker) are positioned. The PD (Photon Detector) complete as the outer part.

The aim of these components is to provide space points for the Recoil Detector internal tracking system which works independent of the HERMES tracking system and to provide particle identification by energy deposition. The Recoil Detector is enveloped by a 1T superconducting magnet for momentum reconstruction.
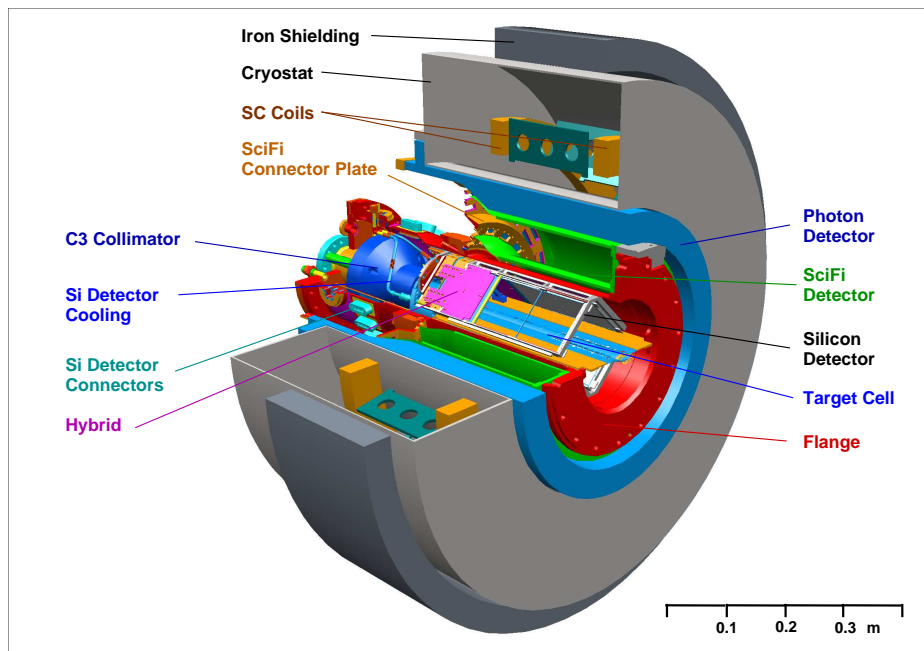
Figure 6.4: *The realization of the Recoil Detector.*

The design requirements were studied by extensive Monte Carlo simulations. The scattering polar angle θ versus the momentum of the recoiling proton p of several involved reactions together with the coverage by the Recoil Detector are illustrated in figure 6.5. By identifying and suppression of background the remaining contamination can be decreased below 1%.

The contributions of the Giessen group is the SFT which is one of the key part of the Recoil Detector. This subdetector was designed to contribute for particle identification and for track reconstruction.

A set of tests were carried out to proof the designed properties and to settle down final configuration parameters. An alignment test run were performed to measure the SFT internal alignment of each single fiber over the

(a)   (b)
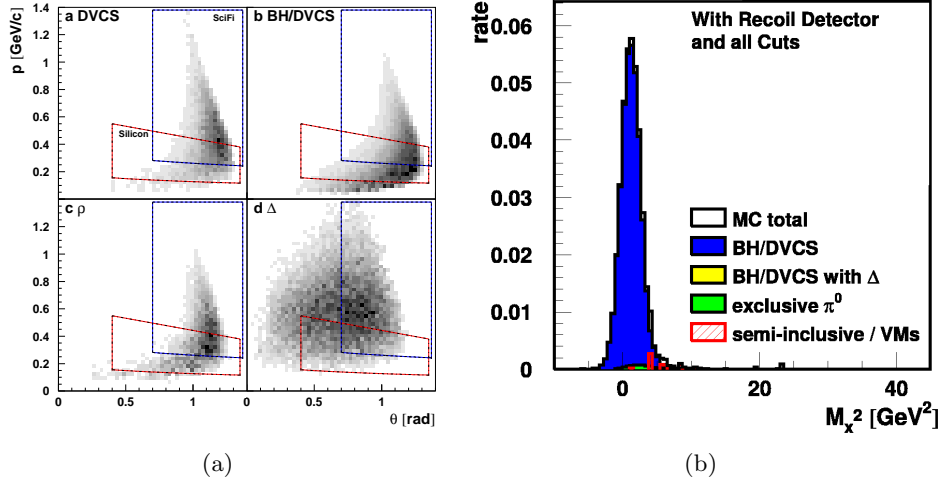
Figure 6.5:   *(a) Distributions of particle momentums p versus polar angle*
θ studied with MC simulations for (a) DVCS process, (b) DVCS / BH in-
terference term, (c) ρ-meson production and (d) Δ resonances or associated
BH-process. The red area of low momentum protons are covered by the SSD,
while the blue area of higher momentum protons are capped by the SFT. (b)
The expected total remaining background investigated by Monte Carlo study
is below 1%.

whole active area. The database of these fibers consists of a list of poly-
nominals up to fourth degree which describes each fiber path. A cosmic ray
test run was set up to check the complete Recoil Detector and to implement
the readout of the Recoil Detector to the HERMES data acquisition. The
Recoil Detector was installed during the winter shutdown of HERA in 2005
and was taking data until the end of HERA in June 2007.

The recently available 06d/06d0 data production was used for investi-
gations of the current performance. The distributions of usual kinematic
variables are in good agreement with analysis of previous productions.

Investigations of elastic events show a very clear correlation for the re-
constructed azimuthal angle between the HERMES forward spectrometer
and the Recoil Detector as shown in figure 6.6.

Preliminary calculations of the leading amplitude for beam charge asym-
metry and for beam spin asymmetry versus the angle ϕ between the scatter-
ing plane and the production plane was performed and shown in figure 6.7.
Comparisons to previous results based on the 06b2 production show good
agreement. The amplitudes for the beam charge asymmetry follows even
with bigger error bars the shape of previous results while the results and
error bars for beam spin asymmetry are closer. Deviations due to change in
the HERMES coordinate system and differences in the response of the elec-

(a) (b)
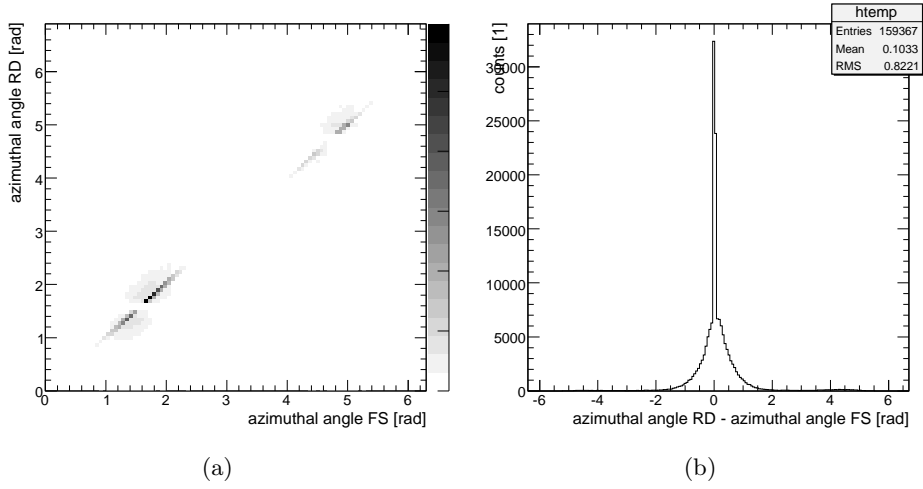
Figure 6.6: *Correlation between HERMES forward spectrometer (FS) and the Recoil Detector (RD). (a) 2D-plot of adjusted azimuthal angle of the starting vertex. (b) Distribution of the adjusted differences. The small peak is as small as the fiber diameter of the SFT.*

tromagnetic calorimeter for electrons and protons can led to small deviations which are currently under investigations.

(a) (b)
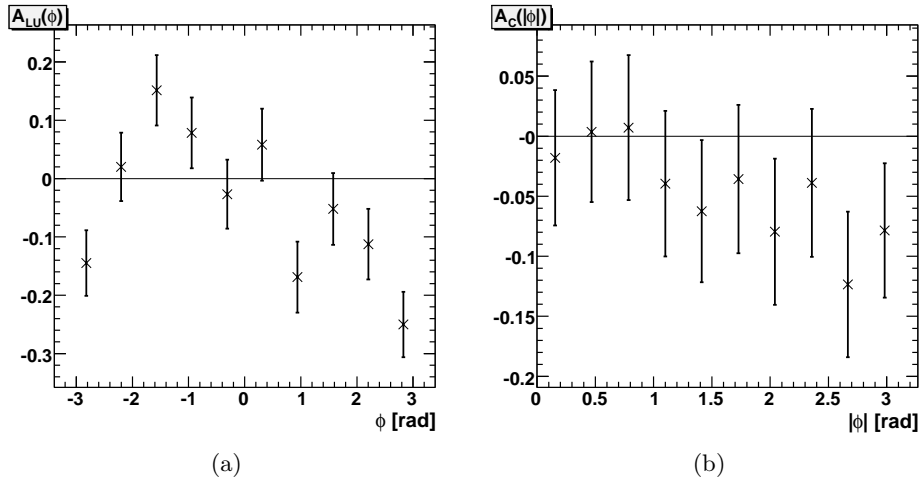
Figure 6.7: *(a) ϕ dependency of the leading amplitude for beam spin asymmetry. (b) $|\phi|$ dependency of the leading amplitude for beam charge asymmetry.*

The preliminary particle identification by the SFT as shown in figure 6.8 is already working and promising to be a good tool in PID scheme. The

separation between pions in the lower left corner and the protons by the solid line is illustrated.

(a)   (b)
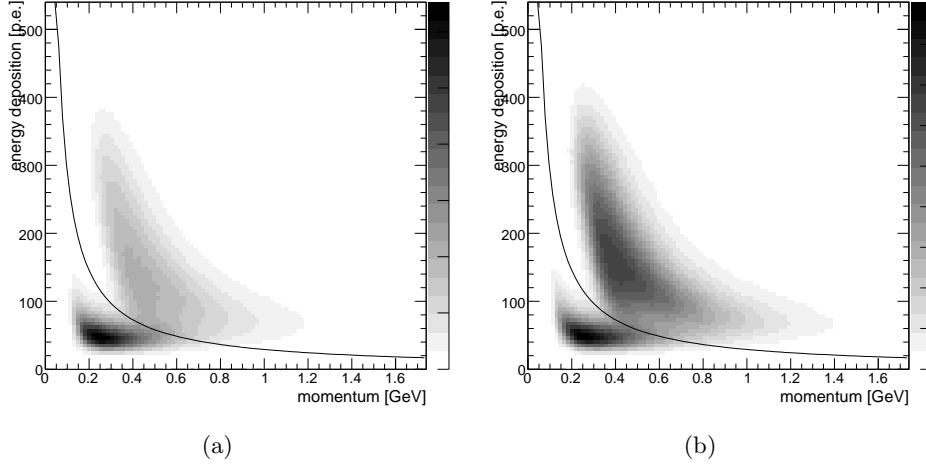
Figure 6.8:   *Particle identification by combining energy deposition dE (in units of photon electrons) with reconstructed particle momentum p (in GeV). Distributions in case of two space points in SFT (a) and four space points in RD (b). The solid line indicates a possible separation by dE ∗ p = 29.*

The normalized distribution of the missing invariant mass M_x^2 in figure 6.9 shows the impact of the Recoil Detector for DVCS event selection. As reminder the reaction of DVCS events can be expressed by

$$(6.2) \qquad\qquad l + p \rightarrow l' + \gamma + p'$$

where l and l' are the initial and scattered lepton, γ is the generated real photon and p and p' are the initial and scattered proton. The black line shown the distribution after applying all event selections for DVCS events but the one for the missing invariant mass M_x^2. The usual event selection on M_x^2 for exclusive events is from $-2.25 GeV^2$ to $+2.89 GeV^2$. By requesting an additional event selection for a single proton track above the solid line in figure 6.8(b) in the Recoil Detector yields to the red curve in figure 6.9(a). Due to undetected bremsstrahlung a small tail to higher missing invariant mass remains. The blue curve in figure 6.9(b) results if events with only a pion in the Recoil Detector are requested. Even without final alignments and calibrations a clear improvements for background suppression is shown.

Currently the fine tuning of the configuration parameters like alignment, calibration and particle identification is in progress and a main data production will be started soon. Informations gathered by investigations with
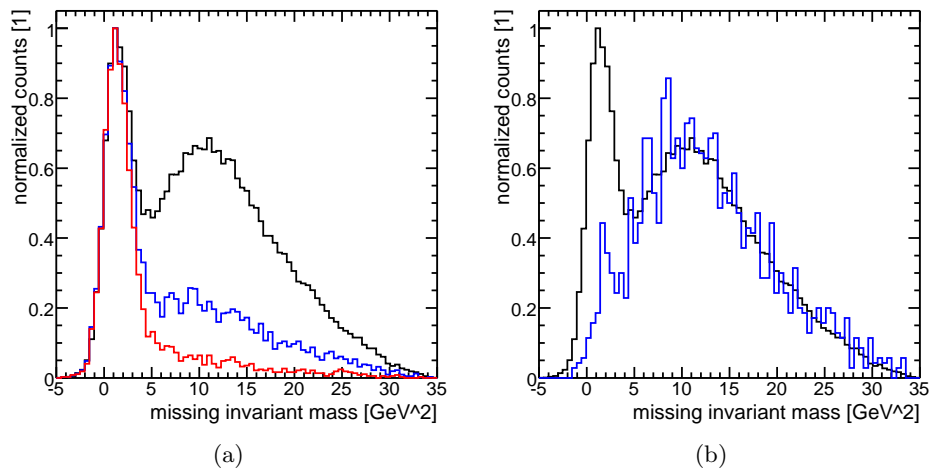
Figure 6.9:   *Arbitrary normalized missing invariant mass distribution mea-*
sured with the HERMES Forward Spectrometer only (black) and with the
contribution by the Recoil Detector on event selection for DVCS candidates.
(a) Additional request of a single proton track (blue) and furthermore a coin-
cidence for the missing proton between HERMES Forward Spectrometer and
Recoil Detector within 3σ for the $p_\phi'^{FS} - p_\phi'^{RD}$ distribution. (b) Additional
request of a single pion track (blue).

the Recoil Detector will be used to iterate previous analysis and to improve
the understanding of the nucleon spin budget.

Appendix A

Data formats

This chapter describes the data format of the standalone readout and of the experiment readout whereas a '*' denotes a variable content.

A.1 Data format for standalone readout

This chapter describes the data format which was used for the standalone readout. In general the data stream is organized as a stream of nodes. Each node consists of a head part to identified the purpose and a data part for the raw data. In the following sections the structure of the all parts are presented.

A.1.1 Node structure

Each node (see table A.1) starts with four signature bytes in order to identify the content of the node. A 32-bit unsigned integer is used to indicate the amount of data bytes containing this node without the head part itself. After this head part the data part of the according size and content are stored. This yields to a total length in bytes of 8+len.

byte offset	byte size	content	comment
0	1	*	signature 1
1	1	*	signature 2
2	1	*	signature 3
3	1	*	signature 4
4	4	len	length of node data in bytes
8	len	*	data part of the node

Table A.1: *Node structure*

116

A.1.2 Sequence of nodes

The stream of data (see table A.2) consists of a sequence of nodes. The sequence starts with a signature to indicate the content of the data stream. A head initiator and a head terminator surrounds the head part. Each event starts with a data initiator and ends with a data terminator. In between a node for each requested sub detector can be found in any order. The list of sub detectors are the Silicon Strip Detector, the ADC part of the Scintillating fiber tracker, the TDC part of the Scintillating fiber tracker and the Photon Detector. The data stream ends with a tail initiator and a tail terminator.

type	comment
signature	a signature entry to identify the stream content
head initiator	a node to initiate the head content
head terminator	a node to terminate head part
data initiator	a node to initiate the data of a event
detector data	readout dependent list of nodes for the sub detector
data terminator	the terminator for each data initiator
tail initiator	a node to initiate the tail content
tail terminator	a node to terminate tail part

Table A.2: *Sequence of nodes of the data stream.*

Signature

This signature (see table A.3) is used like the linux 'file' command in order to identify the content of the stream and has a length of 8 bytes.

byte offset	byte size	content	comment
0	1	4	byte size of length variable in this case 4 times 8 bits = 32 bits unsigned integer
1	1	';'	first filler character
2	1	')'	second filler character
3	1	0	c-string like terminator
4	4	0	zero length for no remaining data

Table A.3: *Content of the signature node.*

Head initiator

The head initiator (see table A.4) contains the status information (see table A.5) about the run number and the timestamp of the start of data taking.

byte offset	byte size	content	comment
0	1	'H'	signature 1
1	1	'E'	signature 2
2	1	'A'	signature 3
3	1	'D'	signature 4
4	4	16	status informations

Table A.4:   *Head initiator content*

byte offset	byte size	content	comment
0	4	0	versioning tag
4	4	*	run number
8	8	*	start of data taking timestamp of struct timeval filled by the call of the c-function 'gettimeofday'

Table A.5:   *Status informations of the head initiator*

Head terminator

The head terminator (see table A.6) does not contain any additional information yet.

byte offset	byte size	content	comment
0	1	'h'	signature 1
1	1	'e'	signature 2
2	1	'a'	signature 3
3	1	'd'	signature 4
4	4	0	zero length for no remaining data

Table A.6:   *Head terminator content*

Data initiator

The data initiator (see table A.7) contains the status informations (see table A.8) about the event number within this run, the timestamp of the event and the source of the trigger.

byte offset	byte size	content	comment
0	1	'D'	signature 1
1	1	'A'	signature 2
2	1	'T'	signature 3
3	1	'A'	signature 4
4	4	20	status informations

Table A.7: *Data initiator content*

byte offset	byte size	content	comment
0	4	0	versioning tag
4	4	*	event number
8	8	*	timestamp of the event
			of struct timeval filled by the
			call of the c-function 'gettimeofday'
16	4	*	source of trigger

Table A.8: *Status informations of the data initiator*

Data node for the Silicon Strip Detector

The data node (see table A.9) contains the data of the Silicon Strip Detector (see section A.2.1). This node is only available if this sub detector is requested to be read out during the data taking.

byte offset	byte size	content	comment
0	1	'S'	signature 1
1	1	'I'	signature 2
2	1	'_'	signature 3
3	1	'_'	signature 4
4	4	len	remaining data of the event

Table A.9: *Data node for the Silicon Strip Detector*

Data node for the ADC of the Scintillating Fiber Tracker

The data node (see table A.10) contains the ADC data of the Scintillating Fiber Tracker which consists of several continuous readout controller buffers (see section A.2.2). This node is only available if this sub detector is requested to be read out during the data taking.

byte offset	byte size	content	comment
0	1	'S'	signature 1
1	1	'F'	signature 2
2	1	'f'	signature 3
3	1	'i'	signature 4
4	4	len	remaining data of the event

Table A.10: *Data node for the ADC part of the Scintillating Fiber Tracker*

Data node for the TDC of the Scintillating Fiber Tracker

For the first implementation of the TDC readout a different TDC named v767 [CAE08c] from CAEN was used. Therefore the data structure of the standalone readout of the TDC chain has the buffer structure of the v767. Even as the TDC hardware was changed to the v1190A [CAE08b] from CAEN the data structure was kept for compatibility purpose. The readout was adjusted to mimicry the buffer structure accordingly.

The data node (see table A.11) contains the TDC data of the Scintillating Fiber Tracker which consists of a (see table A.12). Detailed technical informations can be found in [CAE08c]. This node is only available if this sub detector is requested to be read out during the data taking.

byte offset	byte size	content	comment
0	1	'S'	signature 1
1	1	'F'	signature 2
2	1	'd'	signature 3
3	1	'y'	signature 4
4	4	len	remaining data of the event

Table A.11: *Data node for the TDC part of the Scintillating Fiber Tracker*

byte offset	byte size	comment
0	4	header informations
4	len	hit data
8+len	4	end-of-block informations

Table A.12: *Buffer structure of the TDC v767 from CAEN.*

Data node for the Photon Detector

The data node (see table A.13) contains the data of the Photon Detector (see section A.2.3). This node is only available if this sub detector is requested to be read out during the data taking.

byte offset	byte size	content	comment
0	1	'P'	signature 1
1	1	'D'	signature 2
2	1	'_'	signature 3
3	1	'_'	signature 4
4	4	len	remaining data of the event

Table A.13: *Data node for the Photon Detector*

Data terminator

The data terminator (see table A.14) does not contain any additional information yet.

byte offset	byte size	content	comment
0	1	'd'	signature 1
1	1	'a'	signature 2
2	1	't'	signature 3
3	1	'a'	signature 4
4	4	0	zero length for no remaining data

Table A.14: *Data terminator content*

Tail initiator

The tail initiator (see table A.15) does not contain any additional information yet.

byte offset	byte size	content	comment
0	1	'T'	signature 1
1	1	'A'	signature 2
2	1	'I'	signature 3
3	1	'L'	signature 4
4	4	0	zero length for no remaining data

Table A.15:   *Tail initiator content*

Tail terminator

The tail terminator (see table A.16) contains the status (see tableA.17) informations about the run number, the timestamp for the end of data taking, the number of containing events and the back reference to be start of the tail entry terminator as the very last item for direct access of these data.

byte offset	byte size	content	comment
0	1	't'	signature 1
1	1	'a'	signature 2
2	1	'i'	signature 3
3	1	'l'	signature 4
4	4	24	status informations

Table A.16:   *Tail terminator content*

byte offset	byte size	content	comment
0	4	0	versioning tag
4	4	*	run number
8	8	*	end of data taking timestamp
			of struct timeval filled by the
			call of the c-function 'gettimeofday'
16	4	*	number of stored events
20	4	*	backreference to the start of the tail entry terminator
			for a direct short cut access

Table A.17:   *Status informations of the tail terminator*

A.2 Data format for experiment readout

The data format for the experiment consists of the individual buffers for each Recoil subdetector and are event based as well.

A.2.1 Silicon Strip Detector

The readout of the Silicon Strip Detector consist on four HADC (HERMES Analog to Digital Converter) VME-modules which was originally designed for the Lambda Wheel Detector. The complete buffer is just the sequence of four such HADC modules where each of them contains a header entry (see table A.18), a trigger counter entry (see table A.19), an optional trailer entry (see table A.20) and optional data entry (see table A.21). Extended informations about the Silicon Strip Detector can be found in [Pic08] and in [Vil08].

first bit	last bit	bit size	content	comment
0	11	12	*	event number
12	15	4	*	module number
16	28	13	*	length of events alias number of data entries
29	29	1	*	indicator for trailer error
30	30	1	*	extended header of trailer available
31	31	1	1	indicate header informations

Table A.18: *Header informations are packed in a 32-bit unsigned integer.*

first bit	last bit	bit size	content	comment
0	11	12	*	number of accepted triggers
12	19	8	*	number of rejected triggers
20	31	12	*	number of recognized triggers

Table A.19: *Trigger counter informations are packed in a 32-bit unsigned integer.*

A.2.2 Scintillating Fiber Tracker

In contrast to the standalone readout for the experiment readout by the DSP the buffers for the ADC and TDC are merged to a common block (see table A.22). The common block consists of the 32-bit length value of the TDC content, the TDC content itself, the 32-bit length value of the ADC

first bit	last bit	bit size	content	comment
0	7	8	*	ADC0 trailer
8	15	8	*	ADC1 trailer
16	24	8	*	ADC2 trailer
25	31	8	*	ADC3 trailer

Table A.20:   *Trailer entry consists of four values consisting of a 32-bit unsigned integer.*

first bit	last bit	bit size	content	comment
0	9	10	*	raw ADC value
10	18	9	*	raw common mode value
19	25	7	*	channel number
26	28	3	*	Helix number
29	30	2	*	ADC chip number
31	31	1	0	indicate data informations

Table A.21:   *Each hit data is packed in a 32-bit unsigned integer.*

content, the ADC value itself and a status buffer for additional informations about the ADC readout.

The structure of the TDC data follows the original v1190A [CAE08b] buffer structure in contrast to the standalone readout. The buffer for the ADC can contain several continuous readout controller buffers (see section A.2.2). The content of the status information buffer is summarized in section A.2.2.

byte offset	byte size	comment
0	4	length of TDC buffer in bytes inclusive this
4	len TDC	TDC v1190 from CAEN buffer structure
4 +len TDC	4	length of ADC block in bytes inclusive this
8 +len TDC	len ADC	several readout controller buffers
12 +len TDC +len ADC	len DBG	status information buffer

Table A.22:   *Data buffer for the Scintillating Fiber Tracker for the experiment readout.*

Readout controller buffer structure

Each of the readout controller buffer consists of a header part which is always available and a hit data part where the amount of data depends on sparsification. The entries of such a buffer are all 32-bit integer values and has the sequence which is shown in table A.23 whereas each hit data has the localization information and the adc value together (see table A.24). A remark to reduce confusion about the content of the adc values. Due to hardware implementation the pedestal has a high raw adc value and higher signals has lower raw adc values.

byte offset	byte size	content
0	4	event size in bytes inclusive the this
4	4	event decoder (not used)
8	4	event ID for error indication
12	4	event tagging for synchronization check
16	len	len of remaining hit data of the event

Table A.23: *Buffer structure of the readout controller. The amount of hit data depends on sparsification. N.B. due to hardware implementation the pedestal has a high raw adc value and higher signals has lower raw adc values.*

first bit	last bit	bit size	comment
0	9	10	raw adc value
10	15	6	channel number
16	18	3	module number
19	21	3	port number
22	25	4	readout controller number
26	31	6	not used

Table A.24: *Hit data content packed in a 32-bit unsigned integer.*

Status information buffer

For the readout of the SFT additional status informations are saved for offline data quality checks. It consists of 3 times 32-bit integers for the DTU and 3 times 32-bit integers for each readout controller.

The content for the DTU covers low level informations as bit pattern. DTU0 contains informations about status bits, control bits and version informations. DTU1 covers four counters to track the internal synchronization

by a bank switch counter, a readout counter, a trigger counter and a tagging counter. DTU2 stores internal state and transition informations of the state machine inside the FPGA which is mounted on the DTU.

The monitoring content of the readout controller has informations which are comparable to the DTU. RCdbg0 contains informations about electronic state of certain signals of the handshaking between DTU and RC. RCdbg1 reflect the tagging counter and the trigger counter. RCdbg2 covers the counter for the readout and for the bank switching.

An extended documentation on bit level can be found in [SFT+06]. All these saved informations can be used to verify the data integrity of the SFT and a tools is available to detect desynchronizations and to resynchronized them again.

A.2.3   Photon Detector

The readout of the Photon Detector consist of six commercial charge to digital converter V792 from CAEN. The complete buffer is just the sequence of six such V792 buffers where each of them contains a header entry (see table A.25), hit data entry (see table A.26) and a end-of-block entry (see table A.27). The amount of hit data depends on sparsification. Further informations about the Photon Detector are available in [Haa07] and in [CAE08a].

first bit	last bit	bit size	content	comment
0	7	8	*	not defined
8	13	6	*	number of data entries
14	15	2	0	not defined
16	23	8	*	crate number
24	26	3	010	bit pattern for header content
27	31	5	*	slot number

Table A.25:   *Header information of the V792 buffer.*

first bit	last bit	bit size	content	comment
0	11	12	*	raw adc value
12	12	1	*	overflow bit
13	13	1	*	underflow bit
14	15	2	*	not defined
16	20	5	*	channel number
21	23	3	*	not defined
24	26	3	000	bit pattern for data content
27	31	5	*	slot number

Table A.26:   *Hit data informations of the V792 buffer*

first bit	last bit	bit size	content	comment
0	23	24	*	event counter
24	26	3	100	bit pattern for end-of-block content
27	31	5	*	slot number

Table A.27:   *End-of-block informations of the V792 buffer*

Bibliography

[Ack+98] *The HERMES Spectrometer*
K. Ackerstaff, *et al.*, Nucl. Instrum. Meth. **A417** (1998) 230

[ADA95] *Entity-Relationship Programming System, Version 3.3* Programming Techniques Group, ECP Division, CERN (1995),
http://adamo.web.cern.ch/Adamo/ADAMO_ENTRY.html

[AD08a] *Single Supply, Rail to Rail Low Power FET-Input Op Amp AD820*
Analog Devices Inc. (former Burr Brown)

[AD08b] *ADSP-21061L SHARC*
Analog Devices Inc.

[Air+01] *Measurement of the Beam-Spin Azimuthal Asymmetry Associated with Deeply-Virtual Compton Scattering*
A. Airapetian, *et al.*, Phys. Rev. Lett. **87** (2001) 182001

[Air+05a] *The Time-of-Flight Technique for the HERMES experiment*
A. Airapetian, *et al.*, Nucl. Instr. Meth. **A540** (2005) 305

[Air+05b] *The HERMES polarized hydrogen and deuterium gas target in the HERA electron storage ring*
A. Airapetian, *et al.*, Nucl. Instr. Meth. **A540** (2005) 68

[Air+06] *The Beam-Charge Azimuthal Asymmetry and Deeply Virtual Compton Scattering*
A. Airapetian, *et al*, arXiv:hep-ex/0605108v3 (2006)

[Air+08] *Measurement of Azimuthal Asymmetries With Respect To Both Beam Charge and Transverse Target Polarization in Exclusive Electroproduction of Real Photons*
A. Airapetian, *et al.*, arXiv:hep-ex/0802.2499v2 (2008)

[Ako+02] *The HERMES Dual-Radiator Ring Imaging Čherenkov Detector*
N. Akopov, *et al.*, Nucl. Instrum. Meth. **A479** (2002) 511

[And+01] *Multiwire Proportional Chambers in the HERMES experiment*
A. Andreev, *et al.*, Nucl. Instrum. Meth. **A479** (2001) 482

[Asc+00] *Optical characterization of n=1.03 silica areogel used as radiator in the RICH of HERMES*
E.C. Aschenauer, *et al.*, Nucl. Instrum. Meth. **A440** (2000) 338

[Ash+88] *A measurement of the spin asymmetry and determination of the structure function g_1 in deep inelastic scattering*
J. Ashman, Phys. Lett. **B206** (1988) 364

[Ash+89] *An investigation of the spin structure of the proton in deep inelastic scattering of polarized muons on polarized protons*
J. Ashman, Phys. Lett. **B328** (1989) 1

[Ava+98] *Performance of the Electromagnetic Calorimeter of the HERMES Experiment*
H. Avakian, *et al.*, Nucl. Instrum. Meth. **A417** (1998) 69

[Bac+04] *Single-spin asymmetries: the Trento conventions*
A. Baccetta, U. D'Alesio, M. Diehl, C.A. Miller, arXiv:hep-ph/0410050v2 (2004)

[Bar+93] *The HERA polarimeter and the first observation of electron spin polarization at HERA*
D.P. Barber, *et al.*, Nucl. Instr. Meth. **A329** (1993) 79

[Bau+02] *An Atomic Beam Polarimeter to Measure the Nuclear Polarisation in the HERMES Gaseous Polarized Hydrogen and Deuterium Target*
C. Baumgarten, *et al.*, Nucl. Instr. Meth. **A482** (2002) 606

[Bau+03a] *Measurements of atomic recombination in the HERMES polarized hydrogen and deuterium storage cell target*
C. Baumgarten, *et al.*, Nucl. Instr. Meth. **A496** (2003) 263

[Bau+03b] *The storage cell of the polarized internal H/D gas target of the HERMES experiment at HERA*
C. Baumgarten, *et al.*, Nucl. Instr. Meth. **A496** (2003) 277

[Bau+03c] *A gas analyzer for the internal polarized target of the HERMES experiment*
C. Baumgarten, *et al.*, Nucl. Instr. Meth. **A508** (2003) 268

[Bec+02] *The Longitudinal Polarimeter at HERA*
M. Beckmann, *et al.*, Nucl. Instr. Meth. **A479** (2002) 334

[Beh+07] *Test Beams at DESY*
T. Behnke, *et al.*, note,
http://www.eudet.org/e26/e28/e182/e283/eudet-memo-2007-11.pdf

[Bel+02] *Theory of Deeply Virtual Compton Scattering on the nucleon*
A. Belitsky, *et al.*, Nucl. Phys. **B629** (2002) 323

[Ben+01] *The luminosity monitor of the HERMES experiment at DESY*
T. Benisch, *et al.*, Nucl. Instr. Meth. **A471** (2001) 314

[Ben98] *Polarisierte Bhabha-Streuung und Luminositaetsmessung im HERMES-Experiment*
T. Benisch, Dissertation, HERMES 98-045 (1998)

[Ber+95] *Design and Performance of the Large HERMES Drift Chambers*
S. Bernreuther, *et al.*, Nucl. Instrum. Meth. **A367** (1995) 96

[Ber+98] *The HERMES Back Drift Chambers*
S. Bernreuther, *et al.*, Nucl. Instrum. Meth. **A416** (1998) 45

[Bjo69] *Asymptotic Sum Rules at Infinite Momentum*
J.D. Bjoerken, Phys. Rev. **179** (1969) 1547

[Boe00] *Das Auslesesystem für den Ringabbildenden Čherenkovdetektor im HADES Spektrometer*
M. Boehmer, Diploma Thesis, TU München 2000

[Boh13] *On the Constitution of Atoms and Molecule*
N. Bohr, Philosophical Magazine, Series **6**, Volume **26** (1913) 1-25, 476-502 and 857-875.

[Bra+01] *The HERMES forward tracking chambers: construction, operation and aging effects*
J.T. Brack, *et al.*, Nucl. Instr. Meth. **A469** (2001) 47

[Bro+07] *Moments of generalized parton distributions and quark angular momentum of the nucleon*
D. Brömmel, *et al.*, arXiv:hep-lat/0710.1534v1 (2007)

[Buo+86] *HERA variable-energy "mini" spin rotator and head-on ep collision scheme with choice of electron helicity*
J .Buon, K. Steffen, Nucl. Instr. Meth. **A245** (1986) 248

[CAE08a] *CAEN VME V792 (32 Channel Multievent QDC)*
CAEN S.p.A. - PI 00864500467
http://www.caen.it/nuclear/product.php?mod=V792&fam=vme&fun=qdc

[CAE08b] *CAEN VME V1190A (128 Channel Multihit Multievent TDC)*
CAEN S.p.A. - PI 00864500467
http://www.caen.it/nuclear/product.php?mod=V1190A&fam=vme&fun=tdc

[CAE08c] *CAEN VME V767 (128 Channel Multihit Multievent TDC)*
CAEN S.p.A. - PI 00864500467
http://www.caen.it/nuclear/product.php?mod=V767&fam=vme&fun=tdc

[Dem07] *The polarization of Lambda hyperons in quasi-real photoproduction*
M. Demey, Dissertation, HERMES 07-005 (2007)

[Dia+02] *Design and commissioning of the GSI pion beam*
J .Diaz, *et al.*, Nucl. Instr. Meth. **A478** (2002) 511

[Die03] *Generalized Parton Distributions*
M. Diehl, arXiv:hep-ph/0307382v2 (2003)

[Die+04a] *Generalized parton distributions from nucleon form factor data*
M. Diehl, *et al.*, arXiv:hep-ph/0408173v2 (2004)

[Die+04b] *Quarks vs. gluons in exclusive rho electroproduction*
M. Diehl, A.V. Vinnikov, arXiv:hep-ph/0412162v2 (2004)

[Due+92] *Test of a polarized hydrogen gas target based on the storage cell technique*
M. Düren, *et al.*, Nucl. Instr. Meth. **A322** (1992) 13

[Due95] *The HERMES Experiment: From the Design to the First Results*
M. Düren, Habilitation, HERMES 95-002 (1995)

[Eid+04] *Passage of particles through matter*
S. Eidelmann, *et al.*, Phys. Lett. **B592** (2004) 1

[Ela96] *EL4421C/22C/41C/42C/43C/44C-data sheet Rec.C.*
Elantec inc. (1996)

[Ell03] *Beam-Charge and Beam-Spin Azimuthal Asymmetries in Deeply-Virtual Compton Scattering*
F. Ellinghaus, Dissertation, HERMES 03-044 (2003)

[Ell+05] *Can the total angular momentum of u-quarks in the nucleon be accessed at HERMES?*
F. Ellinghaus, W.-D. Nowak, A.V. Vinnikov, Z. Ye, arXiv:hep-ph/0506264v1 (2005)

[Ell07] *DVCS at HERMES: Recent Results*
F. Ellinghaus, conference proceedings, arXiv:hep-ex/0710.5768v1 (2007)

[Eme96] *Modeling of the HERMES Transition Radiation Detector*
J. V. Emerson, M. Sc. Thesis, HERMES 96-038 (1996)

[GEA93] *GEANT - Detector Description and Simulation Tool*
CERN Program Library Long Writeup W5013 (1993)

[Goe+01] *Hard Exclusive Reactions and the Structure of Hadrons*
K. Goeke, M.V. Polyakov, M. Vanderhaegen, arXiv:hep-ph/0106012v2 (2001)

[Gre+04] *Study of the First Prototype for the HERMES Silicon Recoil Detector with the ZEUS Beam Telescope*
I.M. Gregor, note, HERMES 04-016 (2004)

[Gri87] *Introduction to Elementary Particles* D.J. Griffiths, Wiley, John & Sons, Inc., **ISBN 0-471-60386-4** (1987)

[Guz+06] *The dual parameterization of the proton generalized parton distribution functions H and E and description of the DVCS cross sections and asymmetries*
V. Guzey, T. Teckentrup, arXiv:hep-ph/0607099 (2006)

[Haa07] *The* HERMES *recoil photon detector and nuclear p_t-broadening at* HERMES
Y. van Haarlem, Dissertation, HERMES 07-020 (2007)

[Hae+07] *Nucleon Generalized Parton Distributions from Full Lattice QCD*
P. Hägler, *et al.*, arXiv:hep-lat/0705.4295v2

[Ham00] *Multi-anode Photomultiplier Tube Assembly H7546 data sheet*
Hamamatsu (2000)

[Har04] *The TDC readout of the 12th dynode for the SciFi PMTs*
M. Hartig, note, HERMES 04-066 (2004)

[Hee03] *Quasi-real photo-production of hyperons on polarized $^{1,2}H$ targets*
D. Heesbeen, Dissertation, HERMES 03-052 (2003)

[Her+03] *HERMES DAQ*, HERMES DAQ group, notes (2008),
http://www-hermes.desy.de/groups/daqgrp

[Her+08] *Hermes DataCops*
HERMES Data Quality group, notes (2008)
http://www-hermes.desy.de/groups/daqlgrp

[Her+93] *HERMES Technical Design Report*
HERMES collaboration, note, HERMES 93-015 (1993)
HERMES collaboration, DESY-PRC-93-06 (1993)

[Hoe+05] *Performance of the Recoil Scintillating Fibre Tracker in a Test Beam at GSI*
M. Hoek, *et al.*, note, HERMES 05-013 (2005)

[Hoe06] *Design and Construction of a Scintillating Fibre Tracker for measuring Hard Exclusive Reactions at HERMES*
M. Hoek, Dissertation, HERMES 06-098 (2006)

[Hoe+07] *Performance and response of scintillating fiber modules to protons and pions*
M. Hoek, *et al.*, Nucl. Instr. Meth. **A572** (2007) 808

[Hri+05] *HERMES Recoil Silicon Detector Calibration to MIPs at T22 at DESY*
I. Hristova, note, HERMES 05-014 (2005)

[Jaf96] *Spin, Twist and Hadron Structure in Deep Inelastic Processes*
R.L. Jaffe, arXiv:hep-ph/9602236v1 (1996)

[Ji97a] *Deeply Virtual Compton Scattering*
X.D. Ji, Phys. Rev. **D55** (1997) 7114

[Ji97b] *Gauge-invariant decomposition of nucleon spin*
X.D. Ji, Phys. Rev. Lett. **78** (1997) 610

[Kai+02] *The HERMES Recoil Detector*
R. Kaiser, *et al.*, note, HERMES 02-003 (2002)

[Kai+97] *Particle Identification at HERMES*
R. Kaiser, *et al.*, note, HERMES 97-025 (1997)

[Kas+99] *Fast detector readout for the HADES-RICH*
A. Kastenmüller, *et al.*, Nucl. Instr. Meth. **A433** (1999) 438

[Kiv+01] *DVCS on the nucleon: Study of the twist - three effects*
N. Kivel, M. Polyakov, M. Vanderhaeghen, Phys. Rev. **D63** (2001) 114014

[Kor+02] *Future measurements of Deeply Virtual Compton Scattering*
V.A. Korotkov, W.D. Nowak, Eur. Phys. J. **C23** (2002) 455

[Kra05] *Deeply Virtual Compton Scattering and the HERMES-Recoil Detector*
B. Krauss, Dissertation, HERMES 05-007 (2005)

[Kro07] *Hard exclusive scattering at Jlab*
P. Kroll, arXiv:hep-ph/0710.2771v1 (2007)

[Maz+07] *Deeply Virtual Compton Scattering off the neutron*
M. Mazouz, *et al.*, arXiv:nucl-ex/0709.0450v2 (2007)

[McL+93] *EPIO Experimental Physics Input Output*
I. McLaren, *et al.*, CERN Program Library entry **I101** (1993)

[Men01] *Determination of the Gluon Polarization in the Nucleon*
F. Menden, Dissertation, HERMES 01-073 (2001)

[Mue+94] *Wave functions, evolution equations and evolution kernels from light-ray operators of QCD*
D. Muller, *et al.*, Fortschr. Phys. **42** (1994) 101

[Nas+03] *The HERMES polarized atomic beam source*
A. Nass, *et al.*, Nucl. Instr. Meth. **A505** (2003) 633

[PDG08] *The Review of Particle Physics*
W.M. Yao, *et al.* (Particle Data Group), J. Phys. G 33, 1 (2006) and 2007 partial update for the 2008 edition

[Pic08] *Commissioning of the Recoil Silicon Detector for the HERMES Experiment*
N. Pickert, Dissertation, HERMES 08-002 (2008)

[Rei07] *Quasi-real photo-production of hyperons and their impact on the Lambda polarization measurements*
A.J. Reischl, Dissertation, HERMES 07-004 (2007)

[Ros+07] *Transverse Target-Spin Asymmetry of Exclusive ρ^0 Meson Production on Proton at HERMES*
A. Rostomyan, *et al.*, arXiv:hep-ex/0707.2486v1 (2007)

[Rub06] *Search for the Pentaquark States in Lepton-Nucleon Scattering at HERMES*
L. Rubáček, Dissertation, HERMES 06-071 (2006)

[Ruh99] *Measurement of the Polarized Quark Distributions of the Nucleon at HERMES*
M. Ruh, Dissertation, HERMES 99-051 (1999)

[San+01] *The Gassiplex0.7-2 Integrated Front-End Analog Processor for the HMPID and the Dimuon Spectrometer of ALICE*
J.C. Santiard and K. Marent [Alice Collaboration], **CERN-Alice-PUB-2001-49** (2001)

[San+94] *GASPLEX: a low noise analog signal processor for readout of gaseous detectors*
J.C. Santiard, *et al.* **CERN-ECP-94-17** (1994)

[Sch+98] *The HERMES Polarized ^{3}He Internal Gas Target*
D. De Schepper, *et al.*, Nucl. Instr. Meth. **A419** (1998) 16

[Sei04] *The HERMES recoil detector: a combined silicon strip and scintillating fibre detector for tracking and particle identification*
B. Seitz, Nucl. Instr. Meth. **A535** (2004) 538

[SFT+06] *Technical SciFi Documents*
HERMES Recoil Detector SFT group
http://www-hermes.desy.de/groups/rcoilgrp/recoil/techdoc_sft.php

[Shi+98] *A High Precision Laser Alignment Monitoring System for HERMES Tracking Detectors*
T.-A. Shibata, *et al.*, Nucl. Instr. Meth. **A411** (1998) 75

[Sok+63] *On Polarization and Spin Effects in the Theory of Synchrotron Radiation*
A.A. Sokolov, I.M. Ternov, Dokl. Akad, Nauk SSSR **153** (1963) 1052

[Sok+64] *On polarization and spin effects in synchrotron radiation theory*
A.A. Sokolov, I.M. Ternov, Sov. Phys. Doklady 8 (1964) 1203

[Som03] *Identifikation von Pionen und Protonen mit einem Detektor aus szintillierenden Fasern*
W. Sommer, Diploma Thesis, HERMES 03-046 (2003)

[Som15] *Sitzungsber. Munchen*
A. Sommerfeld, Akad. d. Wiss., **425** (1915) 459

[Sta06] *Superconducting Magnetic Systems for High Energy Polarized Physics*
M. Statera, Dissertation, HERMES 06-069 (2006)

[Ste+03] *Polarized Gas Targets*
E. Steffens, W. Haeberli, Rep. Prog. Phys. **66** (2003) 1887

[Ste+05] *Alignment of the SciFi Detector at the DESY22 electron testbeam*
H. Stenzel, note, HERMES 05-063 (2005)

[Ter+61] *On possibility of polarization of an electron beam due to relativistic radiation in a magnetic field*
I.M. Ternov, Y.M. Loskutov and L.I. Korovina, Zhur. Eksp. Teor. Fis., **41** (1961) 1294

[Thi96] *The Gas System for the HERMES Transition Radiation Detector*
D.M. Thiessen, M. Sc. Thesis, HERMES 96-028 (1996)

[Van+99] *Deeply virtual electroproduction of photons and mesons on the nucleon : leading order amplitudes and power corrections*
M. Vanderhaeghen, P.A.M. Guichon, M. Guidal, arXiv:hep-ph/9905372v1 (1999)

[Vil08] *Detection of Low Momentum Protons with the New HERMES Recoil Detector*
I. Vilardi, Dissertation, HERMES 08-003 (2008)

[Wan+95] *DAD - Distributed Adamo Database system at HERMES*
W. Wander, *et al.*, note, HERMES 95-040 (1995)

[Wen01] *Particle Identification for HERMES Run I*
J. Wendland, note, HERMES 01-067 (2001)

[Wen99] *Improved Particle Identification at HERMES and Polarised Valence Quark Distributions in the Proton*
J. Wendland, M. Sc. Thesis, HERMES 99-016 (1999)

[Wii+79] *PETRA Resultate u.a. ein 3-Jet Event und Hinweise auf Gluon Brems. (vorlaeufig)*
B. Wiik, conference Neutrino 79 Bergen, 18.-22.6.1979

[Xil] *XC4000XLA/XV Field Programmable Gate Arrays*
Xilinx, Inc.

[Yas07] *SSD+SFT alignment first results*
S. Yaschenko, HERMES Technical Recoil meeting, 26.03.2007

[Ye07] *Transverse Target-Spin Asymmetry Associated with Deeply Virtual Compton Scattering on the Proton and A Resulting Model-Dependent Constraint on the Total Angular Momentum of Quarks in the Nucleon*
Z. Ye, Dissertation, HERMES 07-002 (2007)

List of Figures

137

List of Tables

Acknowledgements

At the end of the day it is time to remember.....

and by Iouri and Valdimir for the implementation of the recoil trigger part. Furthermore I want to thank Prof. Toshi-Aki Shibata to support me for the FGIP to stay in Japan. It was a very educational time to extend the horizon and to share time with his students. I have many in the debt to an outnumbered amount of people at HERMES who had incredible amount of patience and support to me in such a great international collaborations. Sorry it is not intentional but I am afraid I will not remember all of them anymore. Nevertheless many, many thanks to those like Alexander, Andy, Avetik, Beni, Elke, Jim, Larry, Ralf, Yorck and to the dedicated recoil group members too.

I want to thank all the people for the time during offsite activities. Special thanks I want to give Andrzej, Bohdan and the others for all the relaxed time of cooking and discussions.

During the run time of the experiment I had a very fine lodging time during my stay at Carsten's home. I want to express my thanks to him, Gisa, their family and their friends. It was always a very entertaining and relaxing occasion to spend my time at their activities.

A lot of thanks belongs to my family as well. My parents, especially for my mother, I fell great respect to make it possible to me to do all these studies and works. I have a rough idea about the difficulties to parent alone two kids in a foreign country out of nothing, chapeau. As well many thanks to my sister and her family for the permanent motivation and help.

Finally I want to thank all those out there to keep this space ship earth running.........

P.S.
At the very end I want to thank Prof. Dr. Claus-Dieter Kohl to be the second referee and another examiner and furthermore to PD. Dr. Stefan Leupold to be the additional examiner of my disputation.